HELSINGIN YLIOPISTO
HELSINGFORS UNIVERSITET
UNIVERSITY OF HELSINKI

Master`s thesis
Department of Geoscience sand Geography
Solid Earth geophysics

TESTING OF REFLECTION SEISMIC, GPR AND MAGNETIC METHODS FOR MINERAL EXPLORATION AND MINE PLANNING AT THE SIILINJÄRVI PHOSPHATE MINE SITE IN FINLAND

Viveka Laakso

12/2019

Supervisors:

Emilia Koivisto (University of Helsinki)
Pietari Skyttä (University of Turku)

UNIVERSITY OF HELSINKI
FACULTY OF SCIENCE
DEPARMENT OF GEOSCIENCES AND GEOGRAPHY

PL 64 (Gustaf Hällströmin katu 2)
00014 Helsingin yliopisto

HELSINGIN YLIOPISTO
HELSINGFORS UNIVERSITET
UNIVERSITY OF HELSINKI

Tiedekunta/Osasto Fakultet/Sektion – Faculty Faculty of Science	Koulutusohjelma/Utbildningsprogram– Degree programme Master's programme in geology and Geophysics	
Tekijä/Författare – Author Viveka Elina Laakso		
Työn nimi / Arbetets titel – Title Testing of Reflection Seismic, GPR and Magnetic Methods for Mineral Exploration and Mine Planning at the Siilinjärvi Phosphate Mine Site in Finland		
Opintosuunta /Studieinriktning – Study track Solid Earth Geophysics		
Työn laji/Arbetets art – Level Master's thesis	Aika/Datum – Month and year 12/2019	Sivumäärä/ Sidoantal – Number of pages 95

Tiivistelmä/Referat – Abstract

Siilinjärvi mine in Finland is the only mine within the European Union producing phosphate rock, a critical raw material for the European Union. With the current mining plans, the production is estimated to continue until 2035. The extent of the ore deposit and new locations for open pits are currently being investigated to ensure continuation of the mining operations also after 2035. The Siilinjärvi carbonatite-glimmerite deposit has been intruded by multiple waste-rock diabase dykes crosscutting the deposit and by a tonalite-diorite intrusion, creating a complex geological setting. To study the depth and lateral extent of the deposit, the diabase dykes, tonalite-diorite, major zones of weakness and the geophysical anomalies related to these features, active-source 2D reflection seismic, Ground Penetrating Radar (GPR) and magnetic surveys were conducted at the Siilinjärvi mine site in fall 2018 as part of the H2020 Smart Exploration project. Understanding the locations of the waste rocks and fracture and shear zones is crucial for mine planning and optimising the production prognoses. The interest of this study is in particular on imaging the sub-horizontal diabase dykes, whose locations and continuation are harder to predict. The focus area of this study is in the southern end of the Särkijärvi pit and the area just south of the pit, where the well-known geology of the pit can be used to constrain the interpretation.

Processing of the reflection seismic data focused especially on the static corrections and the methods used to improve the signal-to-noise ratio. This was done so that the processed data could serve as a reference for new processing methods, focused on these aspects, developed within the Smart Exploration project and planned to be tested with the Siilinjärvi data. The static corrections were constrained by the limited number of first-break picks clear enough for picking from the data. In addition to the bandpass filtering, suppressing the S-wave arrivals was found to be crucial for increasing the signal-to-noise ratio, particularly in the near subsurface which is the main interest area of this study. The GPR and magnetic data were processed with standard processing workflows.

The lateral and depth extent of the Siilinjärvi carbonatite-glimmerite deposit, the large-scale sub-horizontal waste-rock dykes and the major zones of weakness are imaged with the active-source reflection seismic data. The ore deposit is associated with a complex reflectivity pattern due to the intruded diabase dykes and tonalite-diorite, and the fracture and shear zones. The interpreted diabase dykes correlate with a large-scale sub-horizontal waste-rock dyke model created from the production drilling data as part of the Smart Exploration project, supporting the continuation of the sub-horizontal diabase dykes south of the pit. With GPR data, the smaller-scale sub-horizontal dykes within the shallow subsurface (<30 m) are imaged. The GPR data correlates with a detailed waste-rock dyke model created as part of the Smart Exploration project from the southern end of the Särkijärvi pit based on geological mapping, GigaPan images and a 3D photogrammetry model. The reflection seismic, GPR and magnetic data have very different scales and these different data are suitable for different purposes in mineral exploration and mine planning at Siilinjärvi. The carbonatite-glimmerite ore is associated with elevated magnetic total field values and at a larger scale the deposit could possibly be followed with magnetic surveys. With reflection seismic method, the large geological structures can be imaged at depth, and the data could be used for detailed planning of a new open pit. The higher resolution GPR measurements could then be implemented in the operating phase of the mine in a more routine manner to aid creation of reliable production prognoses.

Avainsanat – Nyckelord – Keywords
Reflection seismic, GPR, Magnetic, Mineral exploration, Mine planning, Siilinjärvi phosphate mine, Carbonatite complex

Säilytyspaikka – Förvaringställe – Where deposited
HELDA- Digital repository of the university of Helsinki

Muita tietoja – Övriga uppgifter – Additional information
39 figures and 8 tables

1. TABLE OF CONTENTS

1. INTRODUCTION

The Siilinjärvi open pit mine, eastern Finland, operated by Yara International ASA, is the only mine in the European Union extracting phosphate rock, listed as one of the 27 critical raw materials for the European Union (European Commission 2017a). Globally, 95% of phosphate rock produced is used in agriculture (European Commission 2017b). The Siilinjärvi phosphate mine is located in the Siilinjärvi municipality, Eastern Finland, near Kuopio city. Open pit mining for phosphate rock began in 1979 by Kemira Oy and has been continued by Yara science 2007. At the moment the mine operates two pits, the main Särkijärvi pit and the Saarinen satellite pit reaching 250 m and 60 m depths, respectively. The mine produces approximately 11 Mt of ore per year and is expected to continue production until 2035 (O'Brien et al. 2015). Production in the Saarinen pit will end in 2021, but the Särkijärvi pit will be extended 2 km further north after starting production in a new Jaakonlampi pit in 2021–2022 north of the Särkijärvi pit. In the end the Särkijärvi and Jaakonlampi pits will connect to form one large pit. The extent of the ore deposit and new locations for open pits are currently being investigated to ensure continuation of the mining operations also after 2035.

The Siilinjärvi deposit is an Archean ultramafic carbonatite-glimmerite complex, cut by multiple diabase dykes (Puustinen 1971, O'Brien et al. 2015). Phosphate is produced by extracting apatite from carbonatite-glimmerite ore. From the point of view of mine planning and optimising the production prognosis of the Siilinjärvi mine, it is crucial to know the distribution of waste-rock diabase dykes and any major fracture and shear zones that may affect the stability of the open pit mine and quality of the ore feed to the mill. Locations and continuation of the sub-horizontal waste-rock dykes are difficult to predict and follow compared to vertical dykes which can usually be followed from the surface.

To study the depth and lateral extent of the Siilinjärvi deposit, the diabase dykes and major fracture and shear zones, geophysical measurements were conducted at the Siilinjärvi mine site in fall 2018 as a part of the Smart Exploration H2020 project (Malehmir et al. 2019). Three active-source 2D reflection seismic lines SM1, SM2 and SM3, mine-tunnel active-source data and passive seismic 3D data were acquired during

the field period of the Smart Exploration project (Figure 1). In addition, Ground Penetrating Radar (GPR) and magnetic total field data were collected by the University of Helsinki along the seismic acquisition lines SM1 and SM2, and in the southern part of the Särkijärvi pit (Figure 1). This work focuses on the 2D reflection seismic line SM1, locating right beside the southern tip of the Särkijärvi pit, and on the GPR and magnetic data acquired along SM1 and in the southern parts of the Särkijärvi pit. The aim is to determine how these geophysical methods can be utilized in mineral exploration and mine planning by studying the geophysical anomalies associated with the carbonatite-glimmerite ore and its contacts with the surrounding rocks, and in particular with the diabase dykes. The interest of this study is in the near subsurface (first 1 km) accessible to mining.

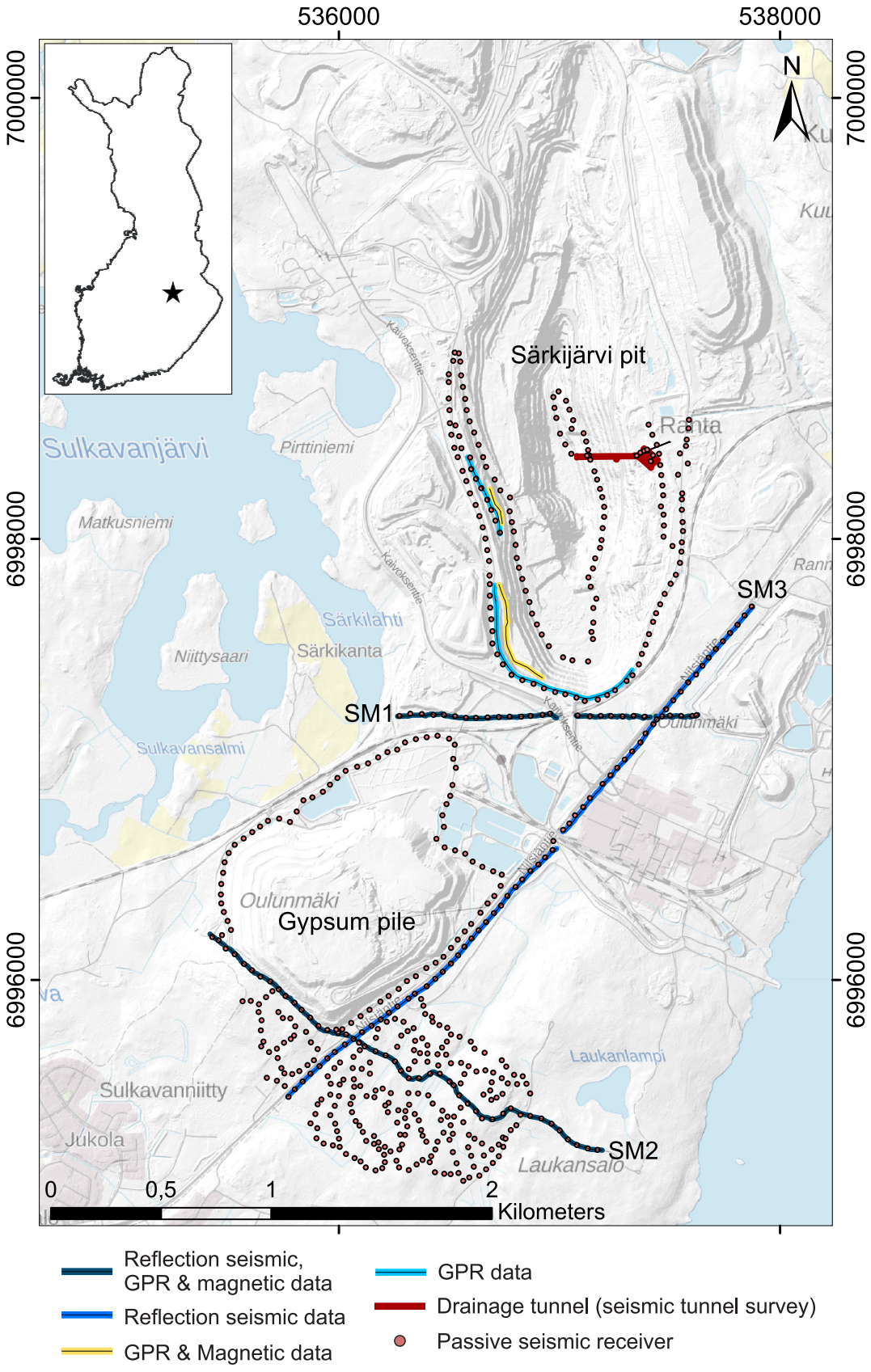

Figure 1. Location of the Siilinjärvi mine site and the measurement lines/locations for reflection seismic, passive seismic, in-tunnel seismic, GPR and magnetic data acquired in fall 2018 by the Smart Exploration project and the University of Helsinki. This study focuses on the reflection seismic, GPR and magnetic data acquired along SM1 and on the GPR and magnetic data collected in the Särkijärvi pit. Coordinates are in the EUREF-FIN ETRS-TM35FIN system. Elevation data: Elevation model 2008-2019, 2 m x 2 m © National Land Survey of Finland.

The reflection seismic methods are based on measuring subsurface reflections of seismic waves arising from elastic property contracts, essentially from changes in the seismic velocities and densities. The reflection seismic methods have the ability to produce high-resolution crustal-scale images. This is pivotal for mine planning applications which require high resolution, as well as for deep mineral exploration applications because of below about 1 km depth other geophysical methods, in particular the electromagnetic methods typically used in mineral exploration, lose their definition of the details. Consequently, over the past few decades, the reflection seismic methods have been increasingly utilized in hard-rock environments for mineral exploration and mine planning purposes. By now, there are numerous examples on applying the seismic reflection method for these applications also in hard-rock environments (e.g., Salisbury and Snyder 2007, Heinonen et al. 2012, Kukkonen et al. 2011, Kukkonen et al. 2012, Malehmir et al. 2012, Koivisto et al. 2015, Heinonen et al. 2019). For example, Koivisto et al. (2015) used seismic reflection data from the Kevitsa Ni-Cu-PGE mining and exploration site to build a 3D model of the key lithological contacts and the near-mine structures, some of which were later confirmed to be crucial for open pit planning (Lindqvist et al. 2017, Malehmir et al. 2018). However, despite the shown potential of the method it is not routinely applied by exploration or mining companies. Reasons for this are for example the relatively high cost of reflection seismic surveys when compared to other geophysical surveys, although the cost is notably lower when compared to the cost of drilling, and lack of expertise on the seismic methods in exploration and mining companies.

The GPR method is based on measuring reflections of electromagnetic waves due to changes in the dielectric properties of the subsurface. Civil infrastructure industry has had a major influence on the development and use of GPR applications (Francke 2012). Applicability of GPR is not only limited to civil infrastructure but is also applied in various environmental and bedrock applications. GPR measurements are relatively easy and inexpensive to implement and the cost of equipment is fairly moderate. In hard-rock environments, GPR measurements have typically been used for near-surface fracture and dyke detection (Davis and Annan 1989, Francke 2012). GPR measurements have also been successfully applied in various geological settings for mineral exploration and mining applications, including for example use of surface-based GPR in kimberlite, bauxite, iron ore and limestone environments (Francke 2012). However, the GPR is still

not widely used within the exploration and mining industry as there are still only a few examples on the use of GPR for mining and exploration applications. The depth extent of the GPR is not substantial, as even with the lowest frequencies (~25–30 MHz) maximum of 40–50 m depth can be achieved. However, the resolution is superior compared to for example seismic methods.

Magnetic methods are commonly and widely used for subsurface studies as they can be done with a low cost. For usability of the magnetic methods, the explored features must be magnetic, i.e., have a high magnetic susceptibility, to produce anomalies. Furthermore, magnetic methods are potential field methods meaning that the source depth of a magnetic anomaly is not readily constrained, challenging the interpretation. However, for example, in Finland, the whole country has been covered with low-altitude aeromagnetic data applicable for regional-scale mineral exploration by the Geological Survey of Finland (Airo 2005). More detailed observations can be made for example with ground magnetic surveys. Magnetic measurements have also been used on carbonatite exploration. For example, Andersson and Malehmir (2018) used ground and airborne magnetic surveys and gravity data to study the internal structural setting of the ring-shaped Alnö alkaline and carbonatite complex in Sweden. The magnetic measurements revealed the Alnö complex and its magnetic ring structure.

1.1. Smart Exploration

Smart Exploration is a project funded by the European Union's Horizon 2020 research and innovation programme (Smart Exploration 2019). Smart Exploration focuses primarily on the development of cost-effective and environmentally friendly measurement systems and methods for geophysical exploration, with an emphasis on seismic, electromagnetic and potential-field measurements. The Smart Exploration project involves 27 partners from nine European countries including, research institutions, companies and stakeholders (Malehmir et al. 2019). University of Helsinki is one of the partners. The project has 6 test sites located in Sweden, Portugal, Greece, Kosovo and Finland, where the Siilinjärvi mining area is the test site of the project. As already mentioned above, the geophysical data examined in this thesis are a part of the data set acquired by the Smart Exploration project at the Siilinjärvi mine site in fall 2018. During the field period, three reflection seismic 2D lines, in-tunnel seismic data, passive

seismic 3D data, GPR and magnetic data were acquired (Figure 1). Goals of the Smart Exploration Siilinjärvi survey were to determine the depth and lateral extent of the ore body south of the Särkijärvi pit and to test the methods for determining the distribution of the waste-rock diabase dykes and imaging of major structures essential for mine planning (e.g., fault and shear zones). Planning of a new open pit south of the Särkijärvi pit is complicated by the infrastructure, e.g., the gypsum pile, factory area and road network, related to the current mining activities. One central goal of the seismic measurements was to gain information on the continuation of the rock units beneath the gypsum pile. So far, the Siilinjärvi passive data have been used in surface wave analysis by Da Col et al. (2019) and the in-tunnel seismic data for shear zone characterization by Donczew et al. (2019) (Figure 1). One aspect of the Smart Exploration project is to develop new methods for reflection seismic processing, including those for the static corrections (Papadopoulou et al. 2019) and for suppression of noise (Balestrini et al. 2019). The methods developed by Papadopoulou et al. (2019) and Balestrini et al. (2019) are planned to be tested with the Siilinjärvi active-source reflection seismic data. The processing workflow of seismic reflection data presented in this study offers a reference workflow for the tests. In this work, the active-source 2D reflection seismic data are discussed along with the GPR and magnetic data sets collected at the Siilinjärvi mine site.

In addition to the already collected data, Unmanned Aircraft Vehicle (UAV) based magnetic data will be acquired at the Siilinjärvi mine site by the Smart Exploration project in 2020. A geophysical prototype UAV system is currently being developed within the Smart Exploration project (Malehmir et al. 2019). Use of UAV-based magnetic surveys in mineral exploration has shown prominent results and in the future, UAV-based measurements could replace, in growing numbers, ground and airplane-based magnetic surveys (Malehmir et al. 2017a, Parshin et al. 2018, Jackisch et al. 2019). The magnetic data acquired within the scope of this thesis will provide information on the magnetic properties of the Siilinjärvi deposit, which can be utilized in the interpretation of the future UAV measurements.

1.1.Aims of the study

The main aim of this study is to test the applicability of the reflection seismic, GPR and magnetic methods for mineral exploration and mine planning purposes in the complex

geological environment of the Siilinjärvi carbonatite complex. Delineating the depth and lateral extent of the carbonatite-glimmerite deposit would aid in focusing the drillings needed for resource evaluation. Furthermore, the carbonatite-glimmerite ore of the Siilinjärvi deposit is intersected by multiple waste-rock diabase dykes. The sub-horizontal diabase dykes, in particular, are expected to produce geophysical anomalies against the contact rocks. In addition to the diabase dykes, major zones of weakness, including fracture and shear zones, should be detected with geophysical methods. Detailed information on the distribution of the diabase dykes and fracture and shear zones at depth is essential for the construction of a reliable geological model that can be successfully used for mine planning.

The objective of this thesis is to present data acquisition and processing of the reflection seismic, GPR and magnetic data acquired at the Siilinjärvi mine site in 2018 (Figure 1), and initially interpret the processed data. With the reflection seismic data, geological features related to the Siilinjärvi deposit can be imaged with good depth extent and resolution, providing information on the lateral and depth continuation of the deposit south of the Särkijärvi pit. In addition, large-scale sub-horizontal waste-rock dykes and major weakness zones are detected with the seismic data. However, low-frequency GPR data provides a better understanding of the finer-scale structures, e.g., the smaller sub-horizontal waste-rock dykes, in the shallow subsurface. The easily implementable GPR measurements have the potential to be used routinely during the mining operations, to constantly support the production. With the high-resolution magnetic total field data, the lateral extent of the carbonatite-glimmerite ore body could possibly be followed, and a better understating of the magnetic properties related to the deposit can be constructed.

With a combined interpretation of geophysical and geological data, the complex shape of the Siilinjärvi ore body can be outlined. Available geological models, borehole data and physical property data are utilized in the interpretation of the reflection seismic, GPR and magnetic data. The GPR data acquired from the southern face of the Särkijärvi pit are interpreted together with detailed GigaPan images and a 3D photogrammetry model acquired by the Digital Leap Project of the University of Helsinki (Geotieteiden digiloikka 2019), and in particular together with a detailed waste-rock dyke network 3D model done within the Smart Exploration project by a PhD student Tuomas Kauti from the University of Turku (Kauti et al. manuscript in preparation). The 3D model is based

on the exposed parts of the Särkijärvi pit and is independent of the geophysical data. The exposed pit walls give an opportunity to directly correlate the known geology to the geophysical signals. Furthermore, the seismic line bypasses the southern wall of the Särkijärvi pit, providing a key to the interpretation of the upper parts of the seismic section (Figure 1).

As already mentioned, one aspect of the Smart Exploration project concerns methodological developments affiliated to seismic processing including reflection seismic processing (Malehmir et al. 2019). Hence, the reflection seismic processing flow applied in this study can work as a reference for testing new improved solutions. The interest in reflection seismic processing is especially on the static corrections and solutions used to increase the signal-to-noise ratio (Papadopoulou et al. 2019 and Balestrini et al. 2019).

The work done in this thesis is closely related to Blathnaid McKevitt's MSc thesis work, done at the University of Helsinki, focusing on the southern continuation of the Siilinjärvi ore body (McKevitt, B., MSc thesis in preparation). McKevitt's work will focus on the two other active-source reflection seismic 2D lines SM2 and SM3 (Figure 1), acquired by the Smart Exploration project, located further south from the Särkijärvi pit.

1.2. Geological background

The Siilinjärvi deposit is an elongated sub-vertical ultramafic carbonatite-glimmerite body, intruded to the surrounding gneiss and granite (Figures 2 and 3). The ore deposit is approximately 15-16 km long and 1-1.5 km wide (Puustinen 1971, O'Brien et al. 2015). The main carbonatite-glimmerite ore runs the whole length of the complex, is up to 900 m wide and covers up to 50% of the deposit volume (O'Brien et al. 2015). So far, the deepest borehole cut on the mineralization has reached a depth of approximately 700 m. The Archean Siilinjärvi carbonatite complex is one of the oldest carbonatite complexes on Earth, dated to ~2.6 Ga (Bayanova 2006, Zozulya et al. 2007, Rukhlov and Bell, 2010, Tichomirowa et al. 2013). The carbonatite complex has been deformed by several events and metamorphosis has taken place particularly during the Svecofennain orogeny ~1.8 Ga (O'Brien et al. 2015).

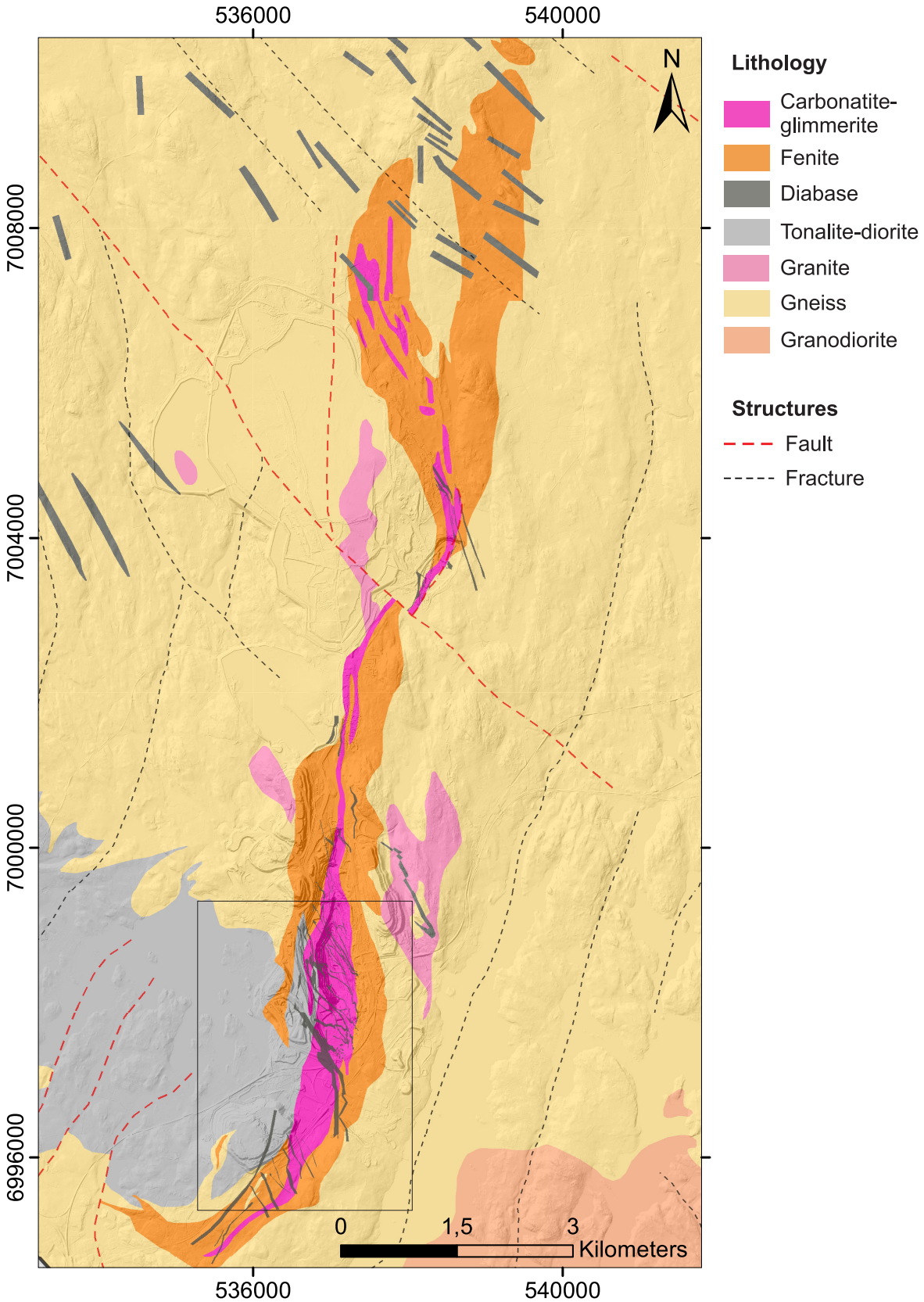

Figure 2. Geology of the Siilinjärvi carbonatite-glimmerite deposit. The area shown in Figure 3 is outlined with the black box. Coordinates are in the EUREF-FIN ETRS-TM35FIN system. Lithology data: Geological map of Finland, pre-quaternary 1:100 000, modified data © Geological Survey of Finland 2014. Structure data: Bedrock of Finland 1:200 000 © Geological Survey of Finland 2016. Base map: Elevation model 2008-2019, 2 m x 2 m © National Land Survey of Finland.

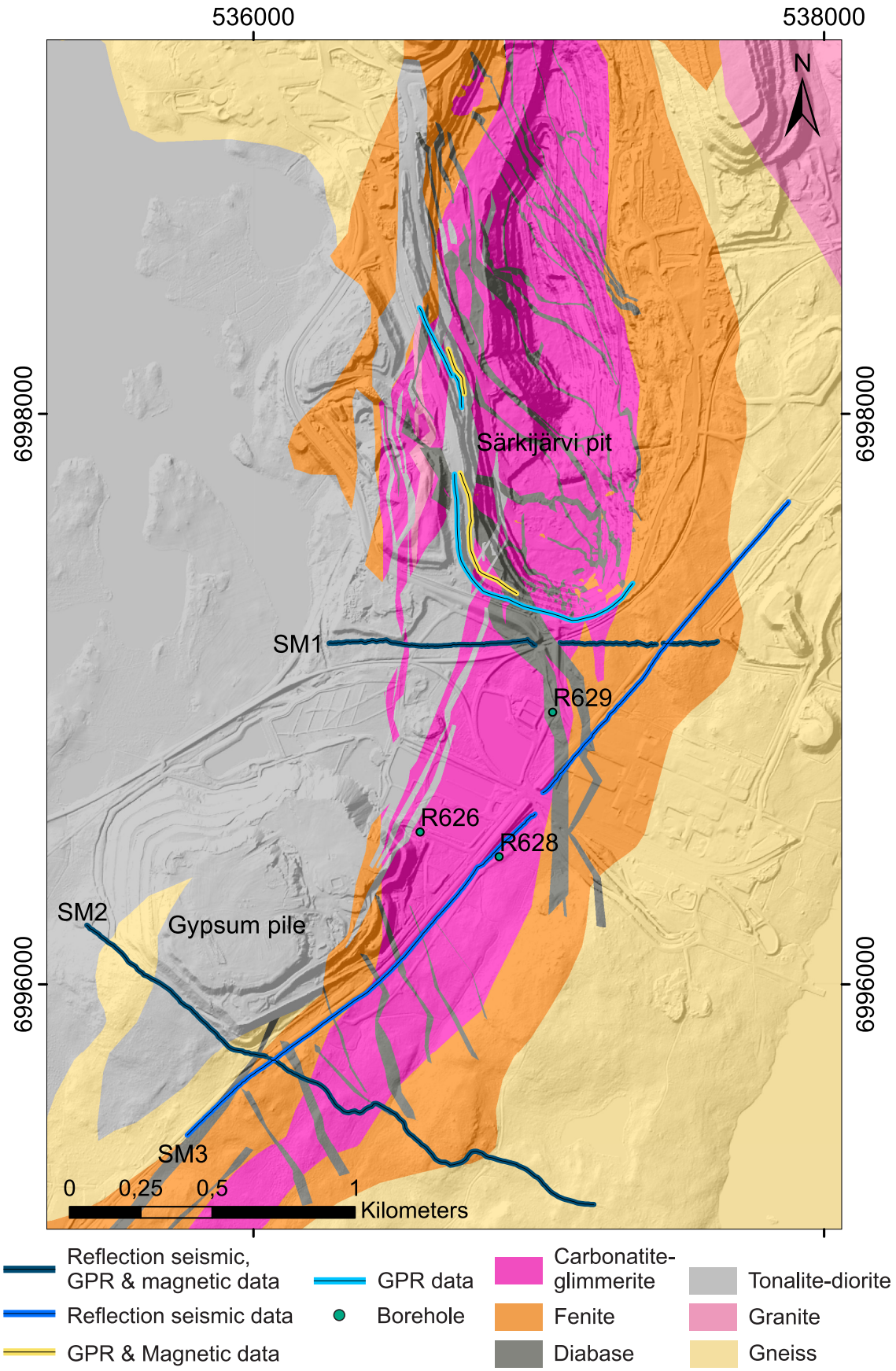

Figure 3. Geology in the Särkijärvi pit and south of the pit and the survey lines acquired during the Smart Exploration field campaign in fall 2018 (Figure 1). The boreholes shown are discussed in section 1.3.1. Geology from Yara. Coordinates are in the EUREF-FIN ETRS-TM35FIN system. Base map: Elevation model 2008-2019, 2 m x 2 m © National Land Survey of Finland.

The carbonatites and glimmerites control the apatite content of the ore, which seems to be slightly higher in the glimmerites (Al Ani 2013, O'Brien et al. 2015). Nearly pure glimmerites are usually located near the edges of the ore while the carbonatite content is generally greater in the central parts of the ore (O'Brien et al. 2015). Carbonate minerals found in Siilinjärvi are mainly white, grey or reddish calcites (Puustinen 1971). Amphibole and phlogopite, an iron-rich mica, are common minerals in the Siilinjärvi glimmerites (Puustinen 1971). Magnetite is also present in the carbonatites-glimmerites but in minor quantities (Puustinen 1971, Al Ani 2013). The carbonatites and glimmerites are usually dominated by vertical to sub-vertical lamination where carbonates occur as thin veins. On average the ore contains 65% micas, 5% amphibole, 15% calcite, 4% dolomite, and 10% apatite (O'Brien et al. 2015). The glimmerite-carbonatite ore is surrounded by a fenite margin, result of metasomatism in the surrounding gneiss and granite (Figure 3).

The carbonatite complex has been intruded by younger mafic diabase dykes and a tonalite-diorite body (Figures 2 and 3). The tonalite-diorite intrusion cuts the carbonatite-glimmerite complex within the southwestern part of the Särkijärvi pit. The diabase dykes appear to be mostly orientated in northwest-southeast or north-northwest-south-southeast directions crosscutting the Siilinjärvi carbonatite complex. The study done by Mattson et al. (2019) suggests that the mafic dykes belong to at least three different generations based on their field relations, petrography and geochemistry. In the southwest of the Särkijärvi pit the diabase dykes, tonalite-diorite and fenite together with the carbonatite-glimmerite ore are intersecting with each other creating a complicated structural setting. In the eastern part of the pit, the contacts between the carbonatite-glimmerite ore and fenite are sharp and well preserved. Despite all the alteration events, the majority of the rocks have preserved their primary textures and compositions.

1.3. Previous geophysical work done in the Siilinjärvi mine site

Earlier geophysical studies have been carried out in the Siilinjärvi mine site for geological and environmental reasons. These studies include petrophysical measurements, and GPR and seismic surveys (Luoma et al. 2014, Malehmir et al. 2017b).

1.3.1. Physical property measurements

A study comprising petrophysical and seismic landstreamer measurements was completed in the Siilinjärvi mine site in 2014 by Malehmir et al. (2017b) (see section 1.3.2 for more). Physical properties were studied with laboratory measurements and downhole logging. The laboratory measurements included density, P-wave velocity and porosity measurements of 65 drill core samples, selected from the study area. The P-wave velocities measured in the laboratory vary approximately between 4800–6500 ms^{-1} (Figure 4). The carbonatite-glimmerites and the diabase dykes have the highest P-wave velocities of ~6500 ms^{-1}, but also the largest velocity ranges. Considering average velocities, diorites have the highest average velocity of 5900 ms^{-1} and diabase dykes the lowest average velocity of 5400 ms^{-1}. The large variability seen in the P-wave velocities could be an indication of a high fracturing on the rocks, making the velocities less representative of the rock types. Density variation between different rock units is more distinct (Figure 4). The diabase dykes have the highest densities varying between 2750–3050 kgm^{-3} and fenites the lowest densities varying approximately between 2580–2680 kgm^{-3}. Diorites and the carbonatite-glimmerites show intermediate densities with densities varying between 2650–2900 kgm^{-3} for the diorites and between 2800–2950 kgm^{-3} for the carbonatite-glimmerites. All the measured samples have porosities below 1.2 %. Overall the fenites have the highest porosities and the carbonatite-glimmerites the lowest.

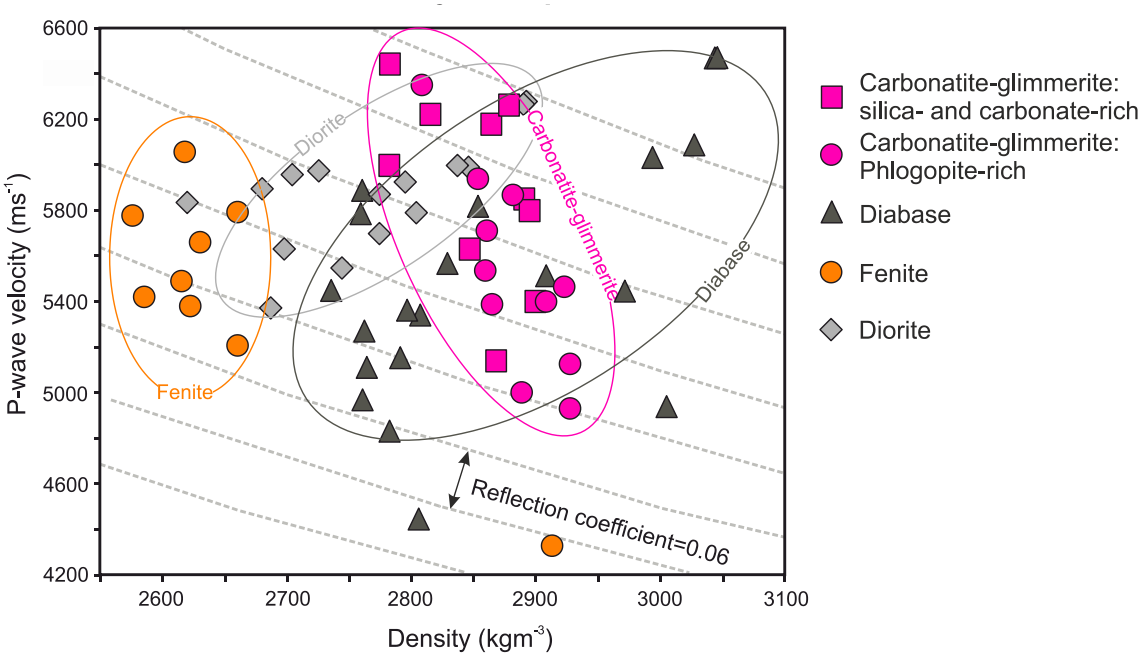

Figure 4. P-wave velocity and density laboratory measurements of drill core samples from the Siilinjärvi deposit. Reflection coefficient of 0.06, considered to be a minimum value for a visible reflection (Salisbury et al. 1996), separates the lines of constant acoustic impedance (see section 2.1.2 for more details). Modified after Malehmir et al. (2017b).

The downhole logging measurements were done in three approximately 300 m long boreholes, drilled south of the main pit (Figure 3) (Malehmir et al. 2017b). Malehmir et al. (2017b) used the Robertson Geologging system for the downhole logging, and measured triple full-waveform sonic, magnetic susceptibility, formation resistivity, temperature, fluid conductivity and natural gamma data. In addition, density measurements, Rock-Quality Designation (RQD) index and geological logging were done for the drill cores. Overall, the diabase dykes showed the highest densities and the diorite and fenite the lowest densities (Figure 5). The in-situ seismic P-wave velocities varied approximately between 2500–7000 ms^{-1} with slightly higher values on average for the diabase dykes and diorite (Figure 5). Reduced P-wave velocities were usually associated with lower rock quality, i.e., lower RQD index (Figure 5). The areas of lower rock quality can be associated with zones of weakness which based on the reduced P-wave velocities should be substantial sources of reflections. The measured magnetic susceptibilities varied between approximately 0.13–0.21 SI (Figure 5). Though overall little variance is seen in the magnetic susceptibility values, the results imply that the carbonatite-glimmerite ore has slightly elevated values. The susceptibility values for the tonalite-diorite and diabase are fairly stable.

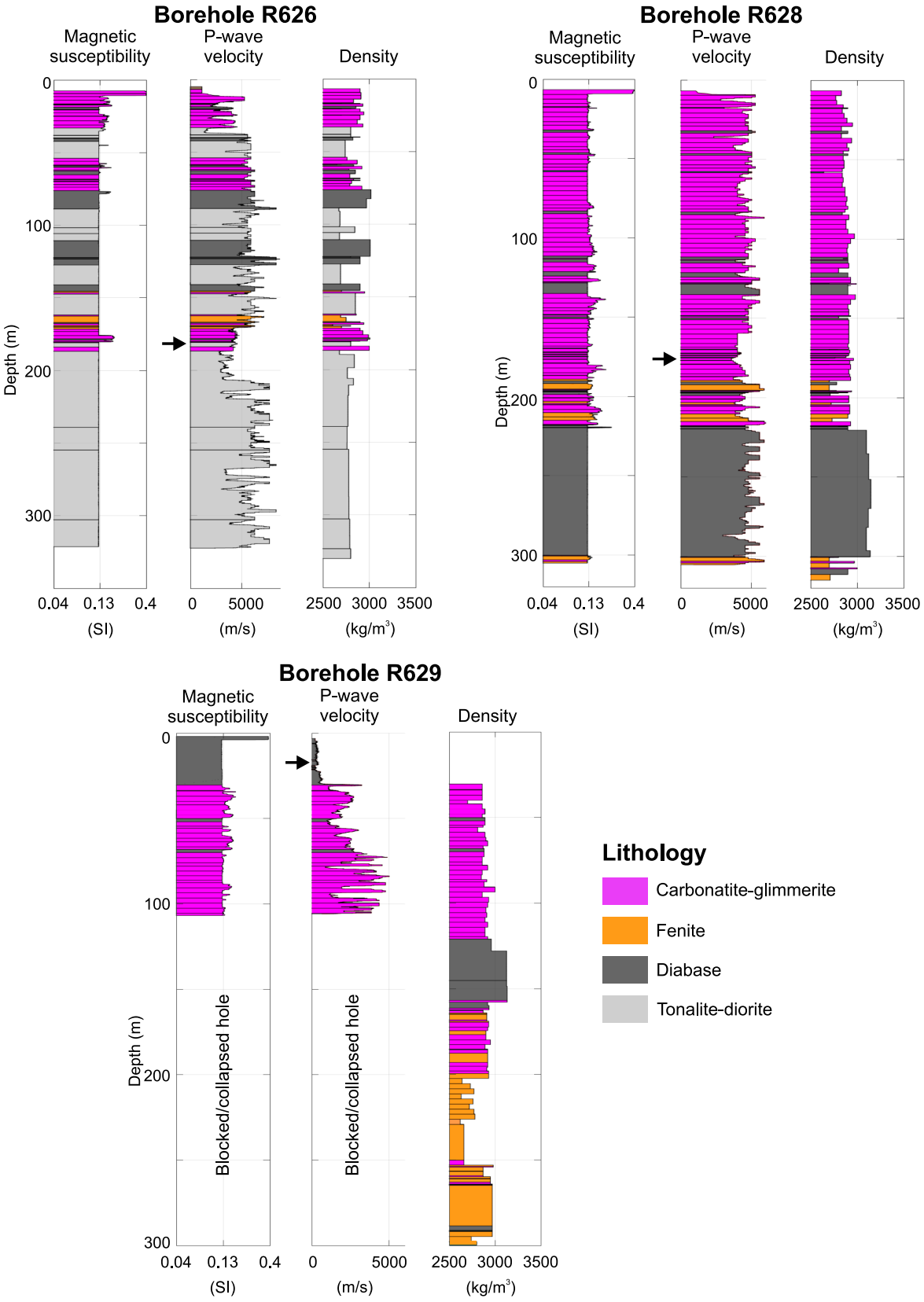

Figure 5. Magnetic susceptibility, seismic P-wave velocity, density and core logging results by Malehmir et al. (2017b), from boreholes R626, R268 and R629 (Figure 3). In borehole R629 downhole logging was done only until ~100m due to a collapse/blockade. The black arrows show areas of reduced RQD. The first magnetic susceptibility values in all three boreholes, looking from the ground surface, are very high compared to the rest and seem to be caused by artefacts. Modified after Malehmir et al. (2017b).

1.3.2. Seismic measurements

Malehmir et al. 2017b completed a seismic landstreamer survey in the Siilinjärvi mine site alongside with the petrophysical measurements discussed in the previous section 1.3.1. The seismic survey consisted of four seismic lines: two located inside the southern part of the Särkijärvi pit and two south of the pit. The data were acquired using a combination of landstreamer and wireless receivers. The Micro-Electro-Mechanical System (MEMS)-based broadband (0–800 Hz) seismic accelerometer landstreamer system has been developed for and mainly used in urban applications (Brodic et al. 2015). In the study by Malehmir et al. (2017b) the landstreamer data were collected with 2–4 m source and receiver spacing, while the wireless records were collected using a 10 m receiver spacing for 10 Hz geophones. A 520 kg drop hammer mounted to a Bobcat was used as a source. The combination of landstreamer and wireless data enabled imaging down to 400–500 m depth but did not provide a good image of the shallow subsurface. A similar study using a landstreamer and a drop hammer over an iron-oxide deposit in the Bergslagen mineral district in Sweden shows that greater depths can be achieved with the cost-effective landstreamer and drop hammer combination. In Bergslagen the whole iron-oxide deposit, known to continue to about 850 m depth, was imaged with the method (Malehmir et al. 2017c).

Malehmir et al. (2017b) applied two processing methods for the seismic data: reflection seismic data processing and traveltime tomography. The reflection seismic data processing followed a convectional processing flow excluding migration of the data. The first arrivals were of good quality which is why traveltime tomography was also implemented. Challenges to the reflection imaging were created by the low signal-to-noise ratio of the data and steeply dipping reflections. The seismic velocity model produced by the traveltime tomography revealed multiple 40–50 m thick low-velocity zones. The low-velocity zones were interpreted to be associated with zones of weakness, i.e., fracture and shear zones. Most of the reflections observed in the reflection imaging results are dipping to the southwest with an angle of 70° or more.

1.3.3. Ground Penetrating Radar (GPR)

In 2014 Luoma et al. (2014) conducted a GPR study in the Siilinjärvi mine area to determine bedrock surface topography and fracturing, and characteristics of the Quaternary overburden deposits in the area. The survey was successful in most areas, except for some areas near the gypsum and calcine waste piles where high electrical conductivity resulted in poor depth penetration of the GPR signal. The data were acquired with Malå - Ramac ProEx Rough Terrain system using 25 and 100 MHz frequency antennas. All of the survey lines were located outside the Särkijärvi and Saarinen pits. The overburden-bedrock contacts produced strong reflections indicating a sharp contact between the two. Luoma et al. (2014) concluded that the thickness of the quaternary deposits varies from 1.05 to 17.7 m, with an average of 2.3 m. Approximately 60% of the area is covered by fine-grained till from a basal melt out and 11% is exposed bedrock. The bedrock is highly fractured in most areas. Fine-grained sediments, such as clay, silt and peat, cover approximately 8% of the area.

In addition to the overburden-bedrock contacts, some of the GPR lines reveal bedrock reflections. The bedrock reflections have not been discussed by Luoma et al. (2014), however, based on them, we concluded that GPR measurements could provide good additional information on the shallow bedrock structures alongside the new seismic reflection data planned within the Smart Exploration project and included GPR measurement to our field campaign.

1.3.4. Magnetic measurements

Geological survey of Finland has covered the area, as well as the whole Finland, with low-altitude aerogeophysical magnetic flight survey (Airo 2005). Figure 6 shows the aeromagnetic survey results for the Siilinjärvi mine area. The aeromagnetic data shows elevated magnetic anomalies coinciding with the known carbonatite-glimmerite deposit (compare Figures 3 and 6), continuing from the Särkijärvi pit to the south of the pit. However, the anomalies don't seem to be very systematic. One of the anomalies is located at the southern end of the Särkijärvi pit and within the focus of this study. The highest magnetic total field anomaly in the area is an artefact created by a pile of burnt iron oxide beside the Särkijärvi pit (Figure 6).

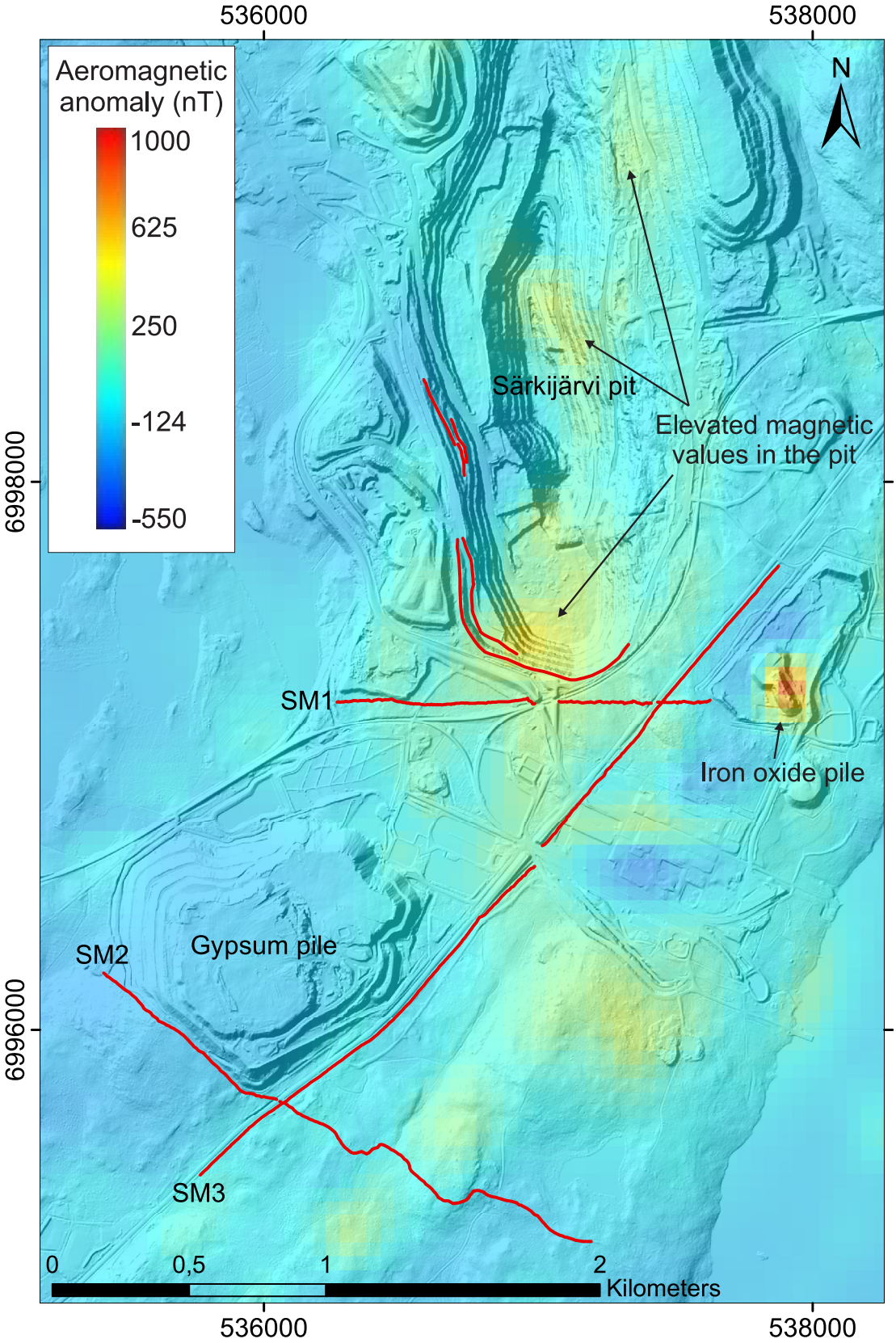

Figure 6. Low-altitude aeromagnetic anomaly map of the study area. Locations of the 2D survey lines presented in Figure 3 are shown with the red lines. Coordinates are in the EUREF-FIN ETRS-TM35FIN system. Aeromagnetic anomaly map of Finland © Geological survey of Finland 2007. Base map: Elevation model 2008-2019, 2 m x 2 m, © National Land Survey of Finland.

2. FUNDAMENTALS OF THE SURVEY METHODS

2.1. 2D reflection seismic

2.1.1. Propagation of seismic waves

Seismic methods are based on the propagation of seismic waves through the subsurface defined by its elastic properties. The background theory presented below focuses on theory essential for understanding the reflection seismic method and processing of reflection seismic data. The theory behind the seismic waves is described with more in depth for example by Sheriff (1995) and Ylimaz (2001).

Seismic waves are waves of energy traveling through a medium. The elastic strain energy of a seismic wave leads to oscillation of rock particles in the medium. Seismic waves are generated by events, like an earthquake or artificial explosions, releasing acoustic energy. Body and surface waves are the main types of seismic waves. Surface waves travel along interfaces between mediums with contrasting elastic properties like the ground surface. Body waves travel through an elastic medium and can be either compressional, i.e., P-waves, or shearing, i.e., S-waves. Compressional and dilatational strain of P-waves creates particle oscillation parallel with the direction of wave propagation. Particle motion in S-waves is perpendicular to the propagation direction and is caused by pure shear strain. With theoretical inspection of stresses and strains, propagation velocities for P- and S-waves can be derived. The velocities are defined by the elastic moduli, i.e., Lame's constants λ and μ and density ρ of a medium. The equations for P-wave V_P and S-wave V_S velocities are:

$$V_P = \sqrt{\frac{\lambda + 2\mu}{\rho}} \tag{2.1}$$

$$V_S = \sqrt{\frac{\mu}{\rho}} \tag{2.2}$$

Conventional seismic reflection surveys typically utilize P-waves. Surface waves are considered noise.

Seismic waves propagate creating a spherical wavefront around the source. The propagation of seismic waves follows the Huygens' principle which states that each point on a wavefront acts as a new point source for waves. The principle is used to understand the successive positions of propagating wavefronts. A spherical wave traveling through a medium continually spreads over a larger area causing a decrease in the energy density. This is referred as spherical divergence. The energy E of a spherical wave decreases exponentially with distance r from the source, meaning that the amplitude A decreases linearly with the propagation distance:

$$E \approx \frac{1}{r^2}, \qquad A \approx \frac{1}{r} \tag{2.3}$$

In addition to spherical divergence, elastic energy associated with the wave motion is gradually absorbed by the medium changing to heat due to internal friction of the medium. Eventually, these lead to the disappearance of the wave motion. Measuring absorption is difficult, but in rocks, the energy loss due to absorption appears to be exponential (Sheriff 1995, p. 59). Thus, the effect of absorption on the amplitude can be expressed as:

$$A = A_0 e^{-\eta x} \tag{2.4}$$

Where A is the amplitude at distance x from location of amplitude A_0 and η is the absorption coefficient. Energy losses due to absorption are greater for higher frequencies.

2.1.2. Seismic waves on an interface

When a seismic wave arrives at an interface between two mediums with different elastic properties, or more generally, encounters an abrupt change in the elastic properties, the wave is reflected and refracted (Figure 7). The energy of the wave is divided between the reflected and refracted waves. Boundary conditions on the interface must be fulfilled: the normal and tangential components of stress and displacement must be continuous (Sheriff 1995, p.47). When both of the mediums are solids, an incident P-wave generates reflected and refracted P- and S-waves. The angles of the refracted and reflected waves can be expressed with the general form of Snell's law:

$$\frac{\sin\theta_1}{V_{P1}} = \frac{\sin\delta_1}{V_{S1}} = \frac{\sin\theta_2}{V_{P2}} = \frac{\sin\delta_2}{V_{S2}} = p \tag{2.5}$$

Where θ_1 is the incident and reflection angle of the P-wave and θ_2 is the refraction angle of the P-wave, δ_1 and δ_2 are the reflection and refraction angles of the S-waves, respectively, V_{P1}, V_{S1}, V_{P2} and V_{S2} are the P- and S-wave velocities of the two mediums and p is the slowness of the ray. When the angle of incidence is critical, θ_2=90º the refracted waves travel along the interface. When the angle of incidence is greater than the critical angle, all energy of the incident wave is reflected.

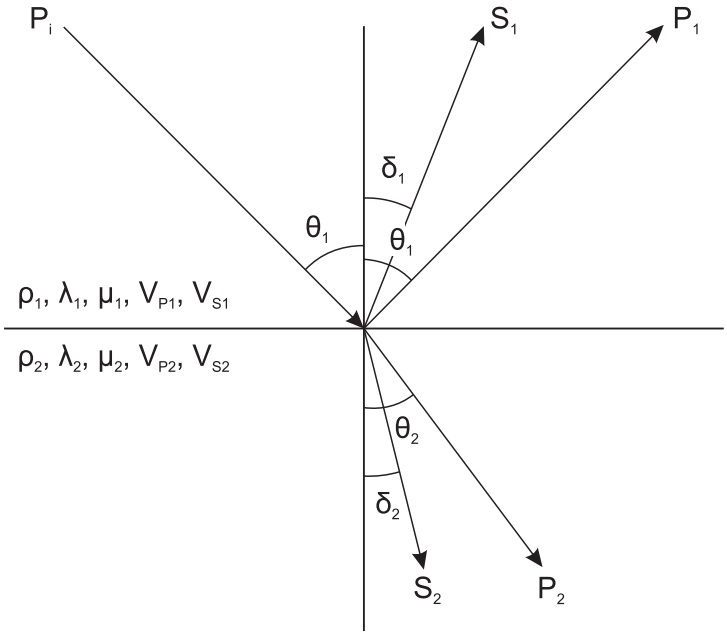

Figure 7. Reflection and refraction of a seismic P-wave at an interface between two mediums where ρ_1 and ρ_2 are densities, λ_1, λ_2, μ_1 and μ_2 are Lame's constants, V_{P1} and V_{P2} are P-wave velocities and V_{S1} and V_{S2} are S-wave velocities of the two mediums. θ_1 is the angle of the incident P_i and reflected P_1 P-waves. θ_2 is the angle of the refracted P-wave P_2. δ_1 and δ_2 are the angles of the reflected S_1 and refracted S_2 S-waves, respectively.

Amplitudes of the reflected and refracted waves are determined by the Zeoppritz' equations describing the partitioning of seismic wave energy at an interface (Sheriff 1995, p.73). The equations relate amplitudes of the incident P-wave and reflected and refracted P- and S-waves to the angle of incidence. When the angle of incidence of a P-wave is small (<15º) there are essentially no tangential stresses or displacements and thus no reflected or refracted S-waves. P-waves with small angles of incidence are typically applied in reflection seismic measurements. In such a case, the situation can be approximated as a normal incidence and the energy of the incident P-wave is divided between the reflected and refracted P-waves. The Zoeppritz' equations reduce to a simple form for a P-wave at normal incidence. Reflection and refraction coefficients determine

the relationships between the amplitude of an incidence wave and the amplitudes of the refracted and reflected waves, respectively. Reflection and refraction coefficients R and T can be derived from the reduced Zoeppritz' equations for a P-wave with a normal incidence:

$$R = \frac{A_1}{A_i} = \frac{I_2 - I_1}{I_2 + I_1} = \frac{V_{P2}\rho_2 - V_{P1}\rho_1}{V_{P2}\rho_2 + V_{P1}\rho_1} \tag{2.6}$$

$$T = \frac{A_2}{A_i} = \frac{2I_2}{I_2 + I_1} = \frac{2V_{P1}\rho_1}{V_{P2}\rho_2 + V_{P1}\rho_1} \tag{2.7}$$

Where I_1 and I_2 are acoustic impedances, ρ_1 and ρ_2 densities and V_{P1} and V_{P2} P-wave velocities of the two mediums. The reflection coefficient defines whether a visible reflection is created by the interface or not. Reflection coefficient value can range from +1 to -1, where the sign indicates the polarity of the reflected wave. If the reflection coefficient is zero or close to zero, the contrast between the elastic properties of the mediums is tenuous. Values further from zero represent greater differences between the properties. In a hard-rock reflection seismic survey the reflection coefficient should be at least 0.06 for a distinct reflection (Salisbury et al. 1996).

When a seismic wave encounters a feature with a radius approximately equal or smaller than the wavelength, energy of the wave is diffracted. Many geological features may have dimensions smaller than seismic wavelengths.

The required minimum spatial separation between two separately distinguishable reflections is defined as the seismic resolution. The vertical resolution of a reflection seismic survey depends on the velocity V and the dominant frequency f_d of the seismic waves. The vertical resolution defines a minimum thickness h_{min} for a layer which can be determined from the data:

$$h_{min} = \frac{V}{4f_d} \tag{2.8}$$

Layers thinner than h_{min} can be detected but the thickness cannot be determined. Detection limit is usually considered to be 1/8 or 1/16 of the dominant wavelength, depending on the source. Horizontal resolution defines a minimum separation d_F, the Fresnel zone, for two horizontal features that can be determined as separate from the data:

$$d_F = \sqrt{\frac{2zV}{f_d}} \tag{2.9}$$

The horizontal resolution is depended on the depth z. Reflecting points that fall within the Fresnel zone are indistinguishable and produce diffraction hyperbolas.

2.1.3. Reflection seismic method

The reflection seismic method is based on measuring seismic waves reflected from interfaces with an acoustic impedance contrast. In a reflection seismic survey, seismic waves are generated using a controlled source like an explosion or a seismic vibrator. The receivers consist of a detection (geophone) and recording (seismogram) components and measure the two-way traveltimes and amplitudes of the reflected traces. Two-way traveltime is the time required for a seismic wave to travel from a source to a reflective surface and back to a receiver on the surface. Each source is recorded by multiple receivers along a survey line. As the source location moves along the survey line, a reflective subsurface point is recorded multiple times with different source-receiver pairs and is known as the Common Depth Point (CDP). When a reflective interface is horizontal. The CDP is equivalent to the Common Mid Point (CMP), a point on the surface of the ground located in the middle of the sources and receivers. (Figure 8). However, when the interface has a dip, the actual reflection points are spread along with the interface covering a larger area. Nevertheless, essentially the CMP point is assumed to correspond with the CDP point. Traces with the same CMP are stacked together to create a CMP stack, a cross-section of the reflective interfaces within the subsurface. CMP stacking is essential for improving the signal-to-noise ratio of the data (Sheriff 1975, p.316). The stacking is done after correcting the recordings part of the same CMP gather to represent zero-offset recordings, i.e., as if there is no separation between the sources and receivers. When a source and a receiver are on the same point on the surface, the reflected waves have a vertical traveltime t_0. However, the two-way traveltime t is greater for source-receiver pairs with larger offsets than for those with a small offset. The additional traveltime Δt required due to a non-zero offset is called the normal moveout (NMO):

$$\Delta t = t - t_0 \tag{2.10}$$

In addition to the offset x, the NMO Δt is depended on the seismic velocity V and the zero-offset traveltime t_0:

$$\Delta t \approx \frac{x^2}{2V^2 t_0} \tag{2.11}$$

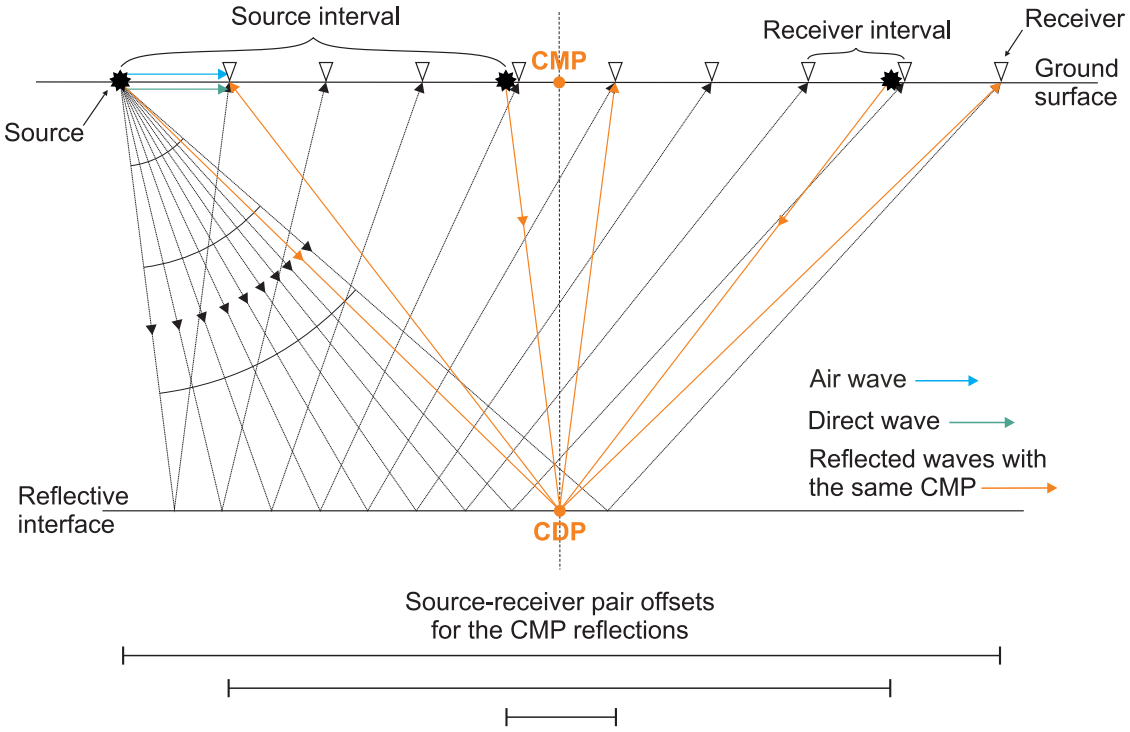

Figure 8. A reflection seismic survey graph showing three source locations, revivers and some of the ray paths from the sources to the receivers. The reflected waves with the same CMP/CDP point are presented with orange. The air and direct waves from the source on the left to the nearest receiver are presented. The air wave travels from the source to the receiver thorough air. The direct wave travels from the source to the receiver along the ground surface. Lastly, the offsets for different source-receiver pairs for the CMP reflections are visually presented.

2.2. GPR

2.2.1. Propagation of electromagnetic waves

Ground penetrating radar uses high-frequency electromagnetic waves to probe the subsurface features. Electromagnetic waves are formed by changing electric and magnetic fields and the relationship is explained with Maxwell's Equations. Electromagnetic waves carry electromagnetic radiant energy as they propagate through

space. This theory section focuses only on the aspects most essential for this study. The theory of the GPR method is explained with more detail for example by Telford et al. (1990) and Reynolds (2011).

As GPR measurements use high-frequency electromagnetic waves, low-loss conditions can be assumed. In low-loss conditions the conductivity $\sigma << \varepsilon\,\omega$, where ε is the dielectric permittivity, which can be defined as a product of vacuum permittivity ε_0 and relative dielectric permittivity ε_r for practical purposes, and ω is the angular frequency. Dielectric permittivity is a complex frequency-dependent material property, which measures the amount of energy stored, i.e., capacitance of a medium, during a polarisation process caused by an altering electric field. The relative dielectric permittivity controls the propagation velocity v of electromagnetic waves. For low-loss conditions and a non-magnetic media, the approximated electromagnetic wave velocity is:

$$v = \frac{c}{\sqrt{\varepsilon_r}} \tag{2.12}$$

Where c is the speed of light. In a non-magnetic media the magnetic permeability, which can be defined as a product of vacuum permeability μ_0 and relative permeability μ_r for practical purposes, equals the vacuum permeability and the relative permeability is assumed to be one $\mu_r=1$.

Analogous to seismic waves, electromagnetic waves propagate creating a spherical wavefront, or in the case of GPR more like a cone, around the source and lose energy while propagating through a non-vacuum medium (see section 2.1.1). Amplitudes of the electromagnetic waves decrease because of the geometrical spreading and due to attenuation caused by the absorption in different materials. This is expressed with attenuation constant α. High attenuation constant leads to stronger attenuation of electromagnetic waves. Attenuation constant of electromagnetic waves in low-loss conditions is:

$$\alpha = \frac{1}{2}\sigma\sqrt{\frac{\mu}{\varepsilon}} \tag{2.13}$$

Where σ is the electrical conductivity, ε is the dielectric permittivity and μ is the magnetic permeability. GPR is inadequate in materials of high electrical conductivity, such as clay, causing strong attenuation of electromagnetic waves. When conductivity is high,

diffusion regime dominates over the propagation regime, essential for GPR, and leads to fast attenuation of the signal.

Skin depth δ is defined as the depth at which the amplitude of the electromagnetic wave has been attenuated to e^{-1} of its initial surface value:

$$\delta = \frac{2}{\sigma}\sqrt{\frac{\varepsilon}{\mu}} \tag{2.14}$$

Practically, the penetration depth of the electromagnetic waves can be estimated to be approximately five times the skin depth. Low-frequency measurements have a greater depth penetration than high-frequency measurements due to the frequency dependence of attenuation (Davis and Annan 1989).

Other factors such as diffractions, distortions, dip displacements and out-of-line reflections affect the GPR traces. These result from the 3D cone-shaped radiation and receiving patterns of the radar antennas (Neal 2004). Due to the 3D cone shape, reflections recorded may not be directly beneath the surveyed point.

2.2.2. Electromagnetic waves on an interface

Electromagnetic waves are reflected and refracted due to changes in the relative permittivity ε_r of subsurface mediums. Similar to the reflection seismic method (see section 2.1.2), the intensity of a reflection at an interface between two mediums is defined by reflection coefficient R. The coefficient depends on the relative permittivities of the mediums. In GPR measurements, the electromagnetic waves are approximated to hit the interface between two mediums vertically, i.e., at a normal incidence angle, and thus be transmitted and reflected vertically, as if the transmitter and receiver would be in the same position on the surface and their offset would be zero. For low-loss conditions, non-magnetic media and a vertical incidence on an interface, the reflection coefficient R is:

$$R = \frac{A_r}{A_i} = \frac{\sqrt{\varepsilon_{r2}} - \sqrt{\varepsilon_{r1}}}{\sqrt{\varepsilon_{r1}} + \sqrt{\varepsilon_{r2}}} \tag{2.15}$$

where A_r is the amplitude of the reflected wave, A_i is the amplitude of the incident wave, ε_{r1} the relative permittivity of medium one and ε_{r2} the relative permittivity of medium two.

The definitions for resolution of a reflection seismic survey can be directly applied to a GPR survey (see section 2.1.2). Vertical resolution ΔV of an antenna depends on the electromagnetic velocity v of the propagation medium and the center frequency of the antenna f_c:

$$\Delta V = \frac{v}{4f_c} \tag{2.16}$$

The center frequency defines the frequency bandwidth of the antenna, centred at the center frequency. For example, a 30 MHz antenna has a 30 MHz bandwidth, centred approximately at 30 MHz. Horizontal resolution ΔH depends also on the depth z, in addition to the electromagnetic wave velocity v and the center frequency f_c:

$$\Delta H = \sqrt{\frac{2zv}{f_c}} \tag{2.17}$$

Reflecting points smaller than the horizontal resolution create diffraction hyperbolas. These include objects that act as isolated point reflectors.

2.2.3. GPR method

The GPR operating principle is in many ways analogous with a reflection seismic survey, except for that instead of seismic waves electromagnetic waves are used and typically the profiles are acquired with a common-offset system, meaning that the offset between the transmitter and receiver is fixed. A radar transmitter transmits pulses of electromagnetic energy into the subsurface which is then reflected from various interfaces within the subsurface, with a relative dielectric permittivity contrast, and recorded on the surface by a radar receiver (Figure 9). As in a reflection seismic survey, the receiver measures the two-way traveltimes (ns) and amplitudes of the received electromagnetic waves. In common-offset data, cross-sections corresponding to the reflection seismic CMP stack are produced immediately after receiving the reflected waves. This is done by

transmitting multiple pulses of electromagnetic energy into the ground at each survey point.

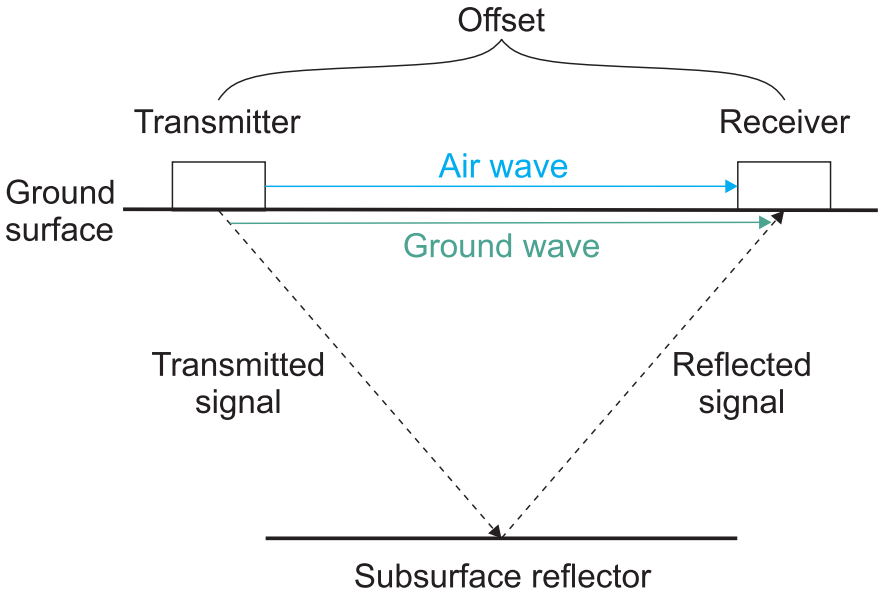

Figure 9. Ray paths of electromagnetic air wave, ground wave and reflected wave from the transmitter to the receiver in a common-offset GPR survey. The air wave travels from the transmitter to the receiver through air. The ground wave travels from the transmitter to the receivier along the ground surface. Modified after (Neal 2004).

A GPR survey design must satisfy sampling principles considering the temporal and spatial sampling intervals. In practice, for a given center frequency f_c the temporal sampling interval Δt should meet the following condition to satisfy the Nyquist sampling criteria:

$$\Delta t \leq \frac{1}{3f_c} \tag{2.18}$$

The Nyquist sampling criteria states the conditions for correctly reconstructing waveform data. The Nyquist criterion for spatial sampling interval Δx is:

$$\Delta x \leq \frac{v}{3f_c} \tag{2.19}$$

Where v is the electromagnetic wave velocity. These sampling criterions apply for all waveform data and can be respectively applied into a reflection seismic survey.

2.3. Magnetic

2.3.1. Basis of magnetism

Magnetic methods are based on measuring the Earth's magnetic field. A magnetic dipole, formed by two magnetic poles with opposite polarity, creates a magnetic field. This is based on the force between magnetic poles. Magnetic fields are also produced by moving electric charges. The Earth's magnetic field is created by the convection of electric currents in the Earth's outer core and can be essentially approximated as a magnetic dipole in the center of the Earth, tilted by about 11° with respect to the Earth's rotation axis. Earth's magnetic field B (T) is composed of Earth's magnetic main field B_E and induced M_i- and remanent M_r magnetization in Earth materials:

$$B = B_E + M_i + M_r \tag{2.20}$$

The magnetic field is strongest at the poles, varying around 60000–70000 nT, and weakest at the equator ~30000 nT (Telford et al. 1990 p.68, Reynolds 2011 p.92, Hinze et al. 2013 p.224). Changes in the flow patterns of the Earth's outer core cause slow secular variation to the magnetic field. Solar activity, rotation of the Earth and electromagnetic sources from human activity cause daily variations to the magnetic field. The crust (and partly upper mantle) creates magnetic anomalies to the Earth's field due to induced and remanent magnetization. The physics and theory behind magnetism are described with more detail by Telford et al. (1990) and Reynolds (2011).

2.3.2. Induced and remanent magnetization

An applied external magnetic field creates an induced magnetic field to a material with magnetic susceptibility. Magnetic susceptibility is a measure of how susceptible material is to become magnetized. The induced magnetization M_i is proportional to the applied magnetic field strength H and susceptibility κ of the magnetizing body:

$$M_i = \kappa \mathrm{H} \tag{2.21}$$

The dependence between the magnetic field B and the magnetic field strength H is defined by the magnetic permeability of vacuum μ_0 ($4\pi \cdot 10^{-7}$ NA^{-2}):

$$B = \mu_0 H \tag{2.22}$$

The highest induced magnetizations are formed within minerals of high susceptibilities. Minerals can be either dia-, para-, ferro- or ferrimagnetic depending on their magnetic properties. Dia- and paramagnetic materials have low magnetic susceptibilities. Ferro- and ferrimagnetic materials, like the mineral magnetite, have the highest susceptibilities and may also have a remanent magnetization. Remanent magnetization is created by permanently magnetized particles in a medium and exists regardless of an applied external field.

2.3.3. Magnetic anomalies

Changes in the magnetic susceptibility create magnetic anomalies. Areas with little variation are magnetically quiet and refer to a low magnetic susceptibility. Features with moderate to high magnetic susceptibility create magnetic anomalies. Due to the dipolar nature of the Earth's main magnetic field, the induced magnetic anomalies may be either positive, negative or have both a positive and negative peak. The induced magnetic field is dependent on the direction of the Earth's magnetic field which, due to the dipolar nature, varies with latitude, meaning that anomalies caused by an identical source for example at the equator and at the northern hemisphere are different. The possible existence of remanent magnetization has an effect on the measured magnetic anomaly complicating the interpretation. In the case of remanent magnetization, the intensity and direction of the remanent magnetism should be determined to comprehend the effect. In addition, the shape and size of a magnetic anomaly depend on the shape, size, orientation, and depth of the magnetizing body. Interpretation of the magnetic anomalies created by differently sized, shaped and oriented sources has been presented and discussed in multiple papers and text books like Telford et al. (1990) and Reynolds (2011).

3. DATA AQUISITION

The data acquisition at the Siilinjärvi mine site was completed over a two-week field period. A team of ~20 people from different partners of the Smart Exploration project took part in the data acquisition of the active-source 2D reflection seismic lines, mine-tunnel active-source data and the passive seismic 3D data. The team members were from Yara, University of Helsinki, Uppsala University, Geopartner, Politecnico di Torino, Delft University of Technology and the Institute of Geophysics of the Polish Academy of Sciences. GPR and magnetic total field data were collected by the University of Helsinki.

As described in the introduction, this work focuses on the active-source 2D reflection seismic line SM1 and on the GPR and magnetic total field data acquired along SM1 and in the southern part of the Särkijärvi pit (Figure 1). In the Särkijärvi pit, the data acquisition lines run over the mined bedrock. South of the pit along SM1, the terrain alters from a clayey soil to gravel and bedrock. The terrain was especially clayey in the middle parts of the line. All safety regulations considering the active mine site were taken into account while planning the survey and followed during the collection of the data.

3.1. Active-source reflection seismic data

The acquisition line SM1 of the reflection seismic data is located south of the Särkijärvi pit, cutting through known geological units like the carbonatite-glimmerite ore, the fenite associated with the Siilinjärvi carbonatite deposit, the tonalite-diorite intrusion, and diabase dykes (Figure 10). The east-west oriented survey line is perpendicular to the north-south running ore body. The total length of SM1 is approximately 1.36 km. Elevation along the line varies between 99-125 m above the sea level. The survey line crosses two roads, a forest road and a railway causing defects to the data coverage (Figure 10).

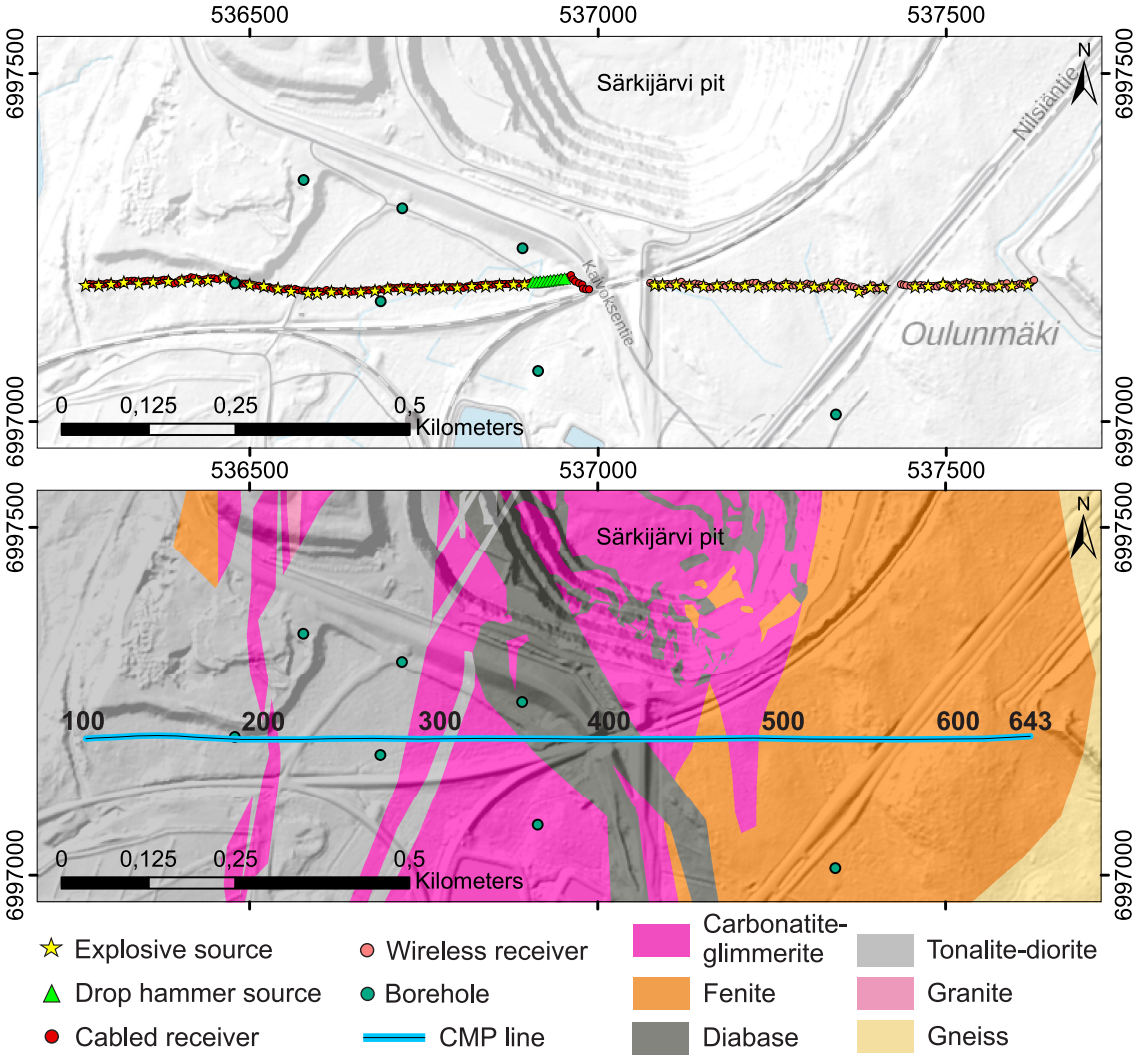

Figure 10. The reflection seismic survey line SM1. Above: the cabled and wireless receivers and the explosives and drop hammer sources for SM1. Below: The CMP line created for processing (see section 4.1.1) with geology. In total, there are 543 CMP points (100–643) every 2.5 m along the CMP line. Coordinates are in the EUREF-FIN ETRS-TM35FIN system. Geology from Yara. Basemap: © National Land Survey of Finland.

The data were acquired using 147 cabled receivers with the Sercel Lite™ system of the Uppsala University on the western side of the line and 115 wireless receivers with the UNITE cable-free seismic acquisition system from Sercel (2019) on the eastern side, after the railway (Figure 11). One 10 Hz geophone was used at each receiver location. The acquisition systems used are all owned by the Uppsala University. The receivers were installed every five meters along the survey line. Because of the railway and the road beside it, approximately 50 m gap was left between the end of the cabled and the beginning of the wireless receivers. The receiver and source locations were marked into the terrain with wooden pegs which were used to survey the locations with a high-precision GPS, and to acquire GPR and magnetic data.

Figure 11. Left: The wireless UNITE acquisition systems connected to a geophone placed to a hole dug in the ground and covered with the ground material. Right: Setting up the Uppsala University Sercel Lite™ cabled receiver system along SM1.

Explosions were used as the main source of seismic energy along the line and a bobcat-mounted drop hammer in places unsuitable for explosions. In total there were 69 source locations with 20 m spacing, with 59 were explosive sources and 10 drop hammer sources. The 520 kg drop hammer, owned by the Uppsala University, was used close to the railway where explosives could not be used due to a necessary safety distance. The explosives were detonated in approximately 2–3 meters deep holes drilled in advance. Orica's blasting device and Uni Tronic TM 600 detonators were used for the blasting (Orica Limited 2019). The Bobcat-mounted hammer was dropped 4–5 times during a 30 s long recording period used for the source, enabling stacking of 4–5 events. Each source is identified with a FFID and shot point identifiers recorded to the observer's log. All the parameters related to the data acquisition of the reflection seismic data have been listed in Table 1.

Table 1. Survey parameters for the reflection seismic line SM1 measured in Siilinjärvi in fall 2018 (Figure 10). The vertical and horizontal resolutions have been calculated with Equations 2.8 and 2.9 using a velocity of 5000 ms^{-1} and a dominant frequency of 60 Hz.

Survey parameters	
Type of survey	Active-source 2D reflection seismic
Profile	SM1
Total survey length of SM1	1.36 km
Spared type	Fixed spread
offset range	Maximum offset of 1362 m
Acquisition system	Sercel Lite 428, GPS time stamping
Nominal CMP fold	68
Recording information	
Number of active channels	262, 147 cabled, 115 wireless
Sampling interval	1 ms
Recording length	6 s (30 s for the Bobcat pattern and 6 s for the explosives)
Source information	
Source spacing	20 m
Energy sources	Explosives & 520 kg Bobcat-mounted drop hammer
Charge weight	125 or 250 g
Shot hole depth	~2–3 m
Bobcat source pattern	4–5 records per source point
Receiver information	
Receiver spacing	5 m
Geophone type	10 Hz
Station configuration	1 geophone per station
Cabled receiver type	Uppsala University Sercel Lite™ system
Wireless receiver type	Sercel UNITE
Theoretical survey resolution	
Vertical resolution*	20 m
Horizontal resolution*	180 m at 200 m depth, 290 m at 500 m depth & 410 m at 1 km depth

* See caption for more information on the calculation.

With equations 2.8 and 2.9, a theoretical resolution for the survey can be calculated. Using a seismic velocity of 5000 ms^{-1} and a dominant frequency of 60 Hz (based on the data analysis, see for more in section 4.1) the theoretical vertical resolution is about 20 m. Using the same values, the horizontals resolution is 180 m at 200 m depth, 290 m at 500 m depth and 410 m at one-kilometer depth (Table 1).

3.2. GPR data

GPR data were acquired from the southern part of the Särkijärvi pit and along survey line SM1 (Figure 12). The GPR data along SM1 have few gaps due to the railway and roads crossing the survey line. In the Särkijärvi pit, the GPR data were collected from mining level 66 and around the southern face of the pit. Two entries to level 66 were utilized to access different parts of the level.

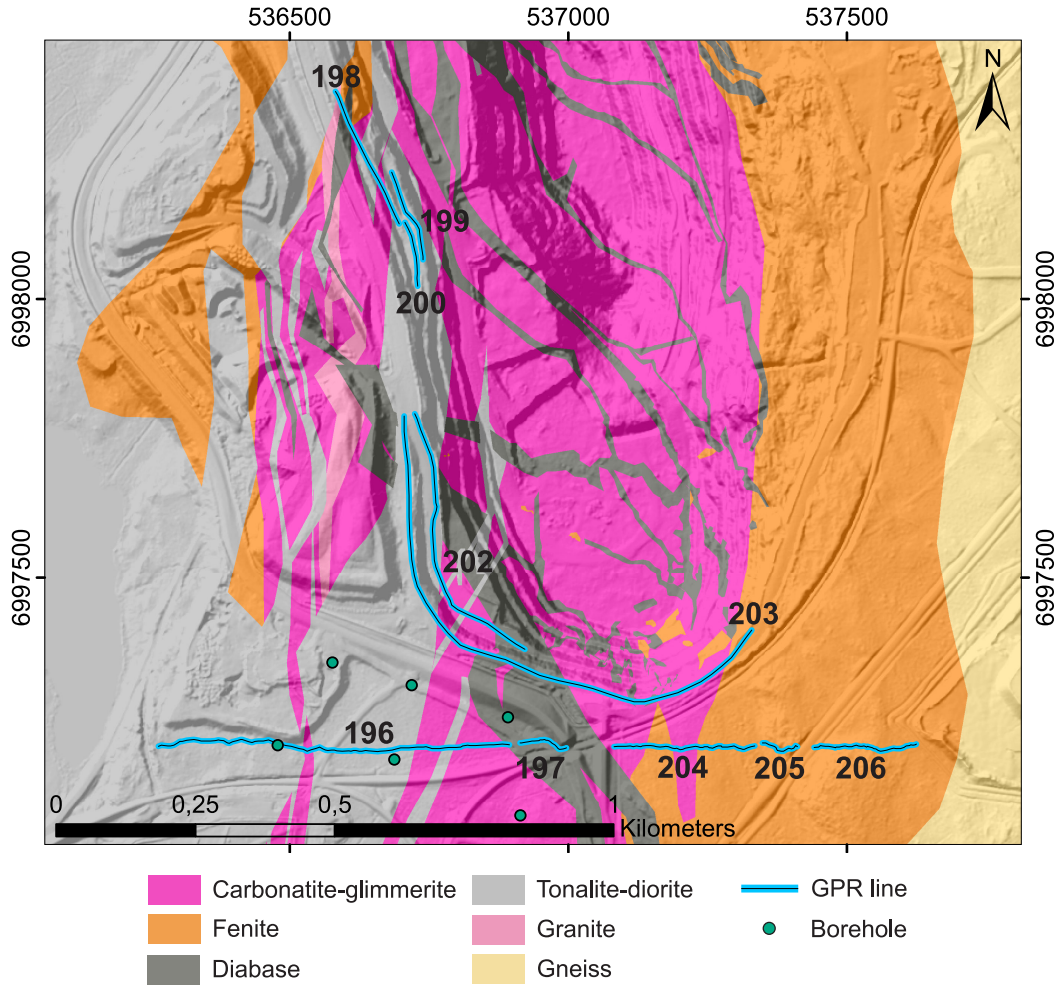

Figure 12. Survey lines for the GPR data collected at the Siilinjärvi mine site in fall 2018. Lines 196, 197, 204, 205 and 206 were acquired south of the Särkijärvi pit, along SM1. Lines 198, 199, 200, 202 and 203 were acquired in the pit. Coordinates are in the EUREF-FIN ETRS-TM35FIN system. Geology from Yara. Basemap: © National Land Survey of Finland.

When imaging bedrock structures is the aim of the study, as was the case in Siilinjärvi, the deepest possible depth penetration is usually vital for the GPR applications, requiring low-frequency antennas with center frequencies varying between 20–50 MHz (Francke 2012). With low-frequency antennas resolution to fine details is compromised over the depth penetration. The GPR data were acquired with MALÅ ProEx system using MALÅ rough-terrain 30 MHz unshielded fixed geometry antenna, and with MALÅ rough-terrain 50 MHz unshielded fixed-geometry antenna along some of the lines (MALA GPR Australia 2009-2017). This study focuses on the 30 MHz data due to the otherwise similar results of the 30 and 50 MHz antennas, except for the deeper depth extent of the 30 MHz data. The whole data acquisition system consists of a MALÅ Professional Explorer control unit, MALÅ XV monitor, measuring wheel/hip chain, GPS and the antennas which include a transmitter and a receiver. The equipment is owned by the University of Helsinki. An unshielded antenna can receive signals from reflectors above the ground surface, such as metallic objects or power lines. Therefore, possible causes of above ground reflectors were noted while acquiring the data. The GPS used with the GPR system is not a high-accuracy GPS and is located on the surveyor's backpack while the actual surface expression of the measurement points is several meters behind, in the middle of the transmitter and the receiver (Figure 13). In the 30 MHz antenna the distance between the backpack and the measurement point (in the middle of the transmitter and the receiver) is approximately 8.67 m.

Figure 13. Operating the GPR data acquisition system at the Särkijärvi pit level 66. The distances between the transmitter and receiver (~6.15 m) and the surveyor and the measurement point (~8.67 m) are presented with the white lines. The GPR GPS is located on the surveyor's backpack.

The GPR profiles along SM1 were collected by following the seismic receiver and source locations marked with wooden pegs. High-precession GPS points were separately surveyed for the pit lines and the lines were acquired in accordance with these. The survey positions were attached to the GPR profiles by adding a marker every time the surveyor reached one. The GPR measurement point is several meters behind the marker and the GPR GPS position. This was corrected for in the data editing stage (see section 4.2 for more).

The GPR data were acquired with a 0.83 m sampling interval, using a measuring wheel to measure the distance. This meets the Nyquist sampling criteria for the spatial sampling

interval (Equation 2.19) when the electromagnetic wave velocity is considered to vary approximately between 0.1–0.13 nsm^{-1}. At each measurement point, the radar transmitted 16 radar signals to the subsurface which were then stacked together. The time window for the recording was set to 1311 ns, meaning that only those signals with two-way traveltime less than 1311 ns were recorded. The survey parameters related to the GPR data acquisition can be seen in Table 2.

Table 2. Survey parameters of the GPR measurements carried out in Siilinjärvi in fall 2018. The vertical and horizontal resolutions have been calculated with Equations 2.16 and 2.17. To calculate the resolutions for the 30 MHz antenna (30 MHz center frequency), electromagnetic wave velocities of 0.08–0.13 nsm^{-1}, presented in Table 4 were used.

Survey Parameters	
Type of survey	2D Ground penetrating radar common offset profiles
Profiles	Lines 198, 199, 200, 202 & 203 in Särkijärvi pit & lines 196, 197, 204, 205 & 206 along SM1
Total length of survey lines	~3.4 km
Equipment	
GPR Unit	MALÅ Professional Explorer control unit
Data logging	MALÅ XV monitor for ProEx
Antenna	MALÅ rough-terrain 30 MHz unshielded fixed geometry antennas
Acquisition parameters	
Antenna separation	6.15 m
Mode of data collection	Measuring wheel
Sampling interval	3.3 ns
Time window (recording time)	1311 ns
Stacks	16
Trace spacing	0.83 m
Theoretical survey resolution	
Vertical resolution*	0.6–1.1 m
Horizontal resolution*	4.8–6.6 m at 5 m depth & 8.4–11.4 m at 15 m depth

* See caption for more information on the calculation.

The theoretical vertical and horizontal resolutions for the 30 MHz antenna were calculated with Equations 2.16 and 2.17. The vertical resolution within the related rock types varies between 0.6–1.1 m. The horizontal resolution varies between 4.8–6.6 m at five-meter depth and 8.4–11.4 m at 15 m depth.

3.3. Magnetic data

High-resolution near-surface magnetic data were acquired at the southern part of the Särkijärvi pit and along the survey line SM1, using resonance magnetometers to measure the magnetic total field along the survey lines and the daily variation of the total field. In total four profiles were measured: MAG1a and MAG1b along SM1, and MAG2 and MAG3 in the pit (Figure 14). The proton free-precession magnetometer and alkali vapor magnetometer are the two main types of resonance magnetometers and were used to measure the daily variation and the total magnetic field along the survey lines, respectively. Proton precession magnetometers are based on measuring the free-precession frequency of polarized magnetic protons (hydrogen nuclei). In the presence of an external field, the magnetic spins of protons align with the polarizing field. When the polarizing field is removed the protons realign with Earth's magnetic field and start to precess. The precession frequency f_p (Larmor precession frequency) is proportional to the total magnetic field B:

$$B = 2\pi f_p/\gamma_p \tag{3.1}$$

Where γ_p is the gyromagnetic ratio of the proton and the factor $2\pi/\gamma_p$ equals to 23.487 ±0.002 $nTHz^{-1}$. The alkali vapor magnetometers utilize optical pumping to measure the magnetic total field (Bloom 1962). The total magnetic field can be determined from the precession frequency of flickering light produced by optical pumping of alkali vapor absorption cells.

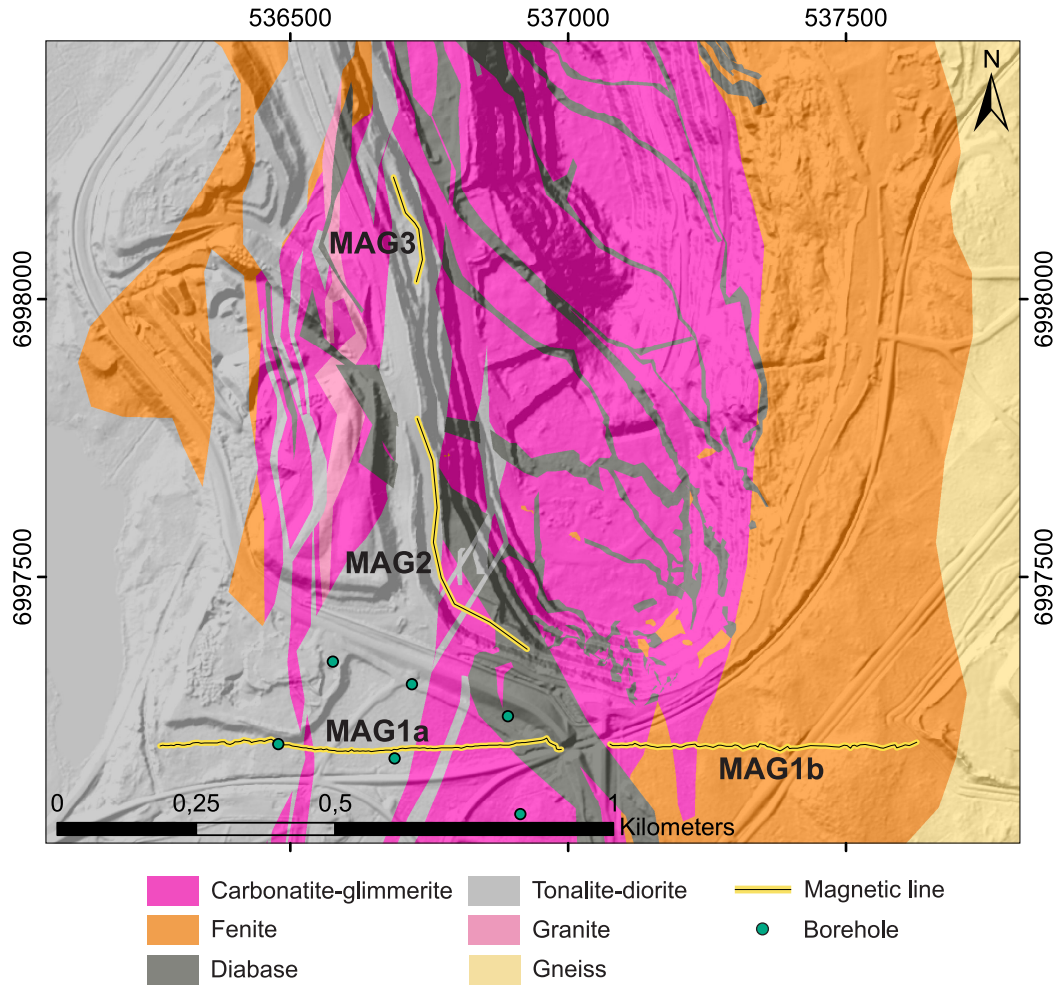

Figure 14. Survey lines for the magnetic total field data collected in the Siilinjärvi mine site in fall 2018. Survey lines MAG1a and MAG1b were acquired south of the pit along SM1 and survey lines MAG2 and MAG3 were acquired in the Särkijärvi pit. Coordinates are in the EUREF-FIN ETRS-TM35FIN system. Geology from Yara. Basemap: © National Land Survey of Finland.

The magnetic profiles measured in the pit ran along with two of the GPR profiles measured at level 66 (Figure 3). The magnetic measurements were made with G-858 MagMapper a self-oscillating cesium vapor magnetometer from Geometrics (2018a) (Figure 15). It uses non-radioactive Cs-133, operates between 18000-95000 nT and has an 0.01-0.05 nT resolution (Geometrics inc. 2001). Magnetic total field values were measured using a single sensor on the G-858 MagMapper. The measurements were done using a simple survey mode of the G-858 MagMapper enabling discrete station recordings. One-meter measurement spacing was used in the pit and 2.5 m spacing along MAG1. The measurements along MAG1, following the SM1, were acquired utilizing the seismic source and receiver pegs. Measurements were taken between and at each peg. As the magnetic profiles in the pit were relatively short, measurement points were marked to the ground. Daily fluctuation of the Earth's magnetic field was measured with a G-857

magnetometer from Geometrics (2018b). The G-857 is based on the high accuracy proton precession method. The device has a 0.1 nT resolution and operates between 20000-90000 nT (Geometrics inc., 2015). The base station was set to measure the magnetic total field every 10 seconds. Before setting the base station, the times of the G-857 and G-858 were synchronized. The G-857 was installed to measure the daily variation of the Earth's magnetic field to a tree as far as possible from any magnetic noise sources. Both of the magnetometers used are owned by the University of Helsinki. The survey parameters related to the magnetic total field measurements are presented in Table 3.

Figure 15. Acquiring the magnetic total field data along SM1 with the G-858 MagMapper magnetometer.

Table 3. Survey parameters of the magnetic total field measurements carried out in Siilinjärvi fall 2018.

Survey parameters	
Type of survey	Single sensor magnetic 2D profiles
Survey lines	MAG1(a & b), MAG2, MAG3
Total length of survey lines	~2.05 km
Survey equipment	G-858 MagMapper (survey lines) & G-857 magnetometer (base station)
Measurement spacing	2.5 m (MAG1) & 1 m (MAG2 & MAG3)
Base station measurement interval	10 s

4. DATA PROCESSING

4.1. Processing of reflection seismic data

Processing of reflection seismic data requires multiple time-consuming steps, each building on the success of the earlier steps. Figure 16 shows the processing workflow used for the Siilinjärvi reflection seismic data. Processing of data along SM1 focused on the first 2 kilometers, in particular on the uppermost 1 km, most interesting for the Siilinjärvi mine. The aim of the processing is to reveal and visualise the reflection events. The reflection seismic data were processed with GLOBE Claritas software (GLOBE Claritas 2019). The main features and theory behind the processing steps applied will be discussed in this section. Seismic data processing is discussed with more detail for example by Sheriff (1995) and Ylimaz (2001).

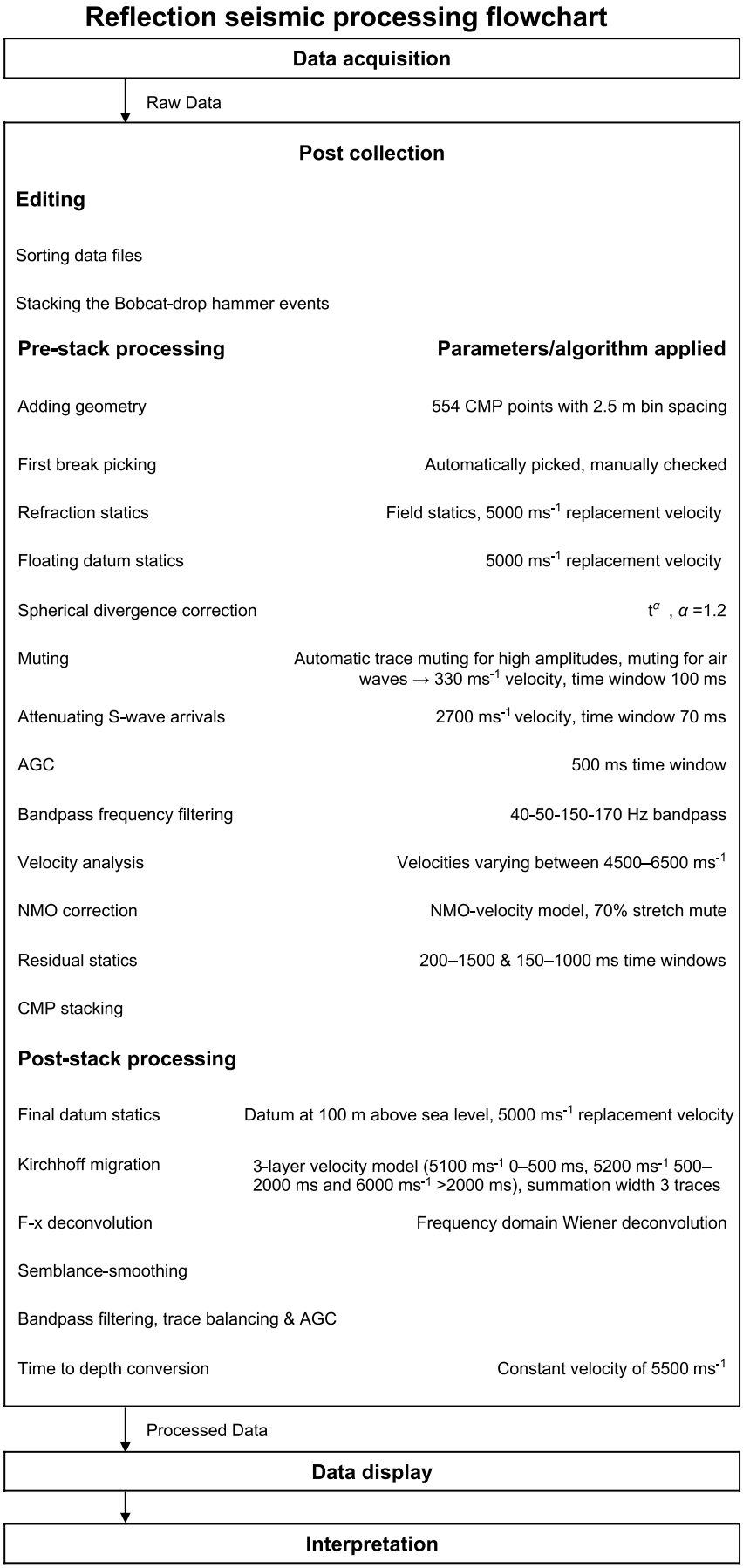

Figure 16. Processing workflow applied to the reflection seismic data.

The raw data contains several noisy low-frequency traces, with most having a dominant frequency of less than 30 Hz. First breaks (velocity approximately 5000 ms^{-1}), S-wave arrivals (velocity ~2600–2800 ms^{-1}) and air waves (velocity ~330 ms^{-1}) can be clearly distinguished from the raw explosive shot gathers (Figure 17). In the drop hammer shot gathers, the first breaks are very faint, no air waves are seen, and the S-waves are the most dominant arrivals (Figure 18). Reflectivity in the drop hammer shot gathers is much weaker as noise is more emphasized compared to the explosive shots.

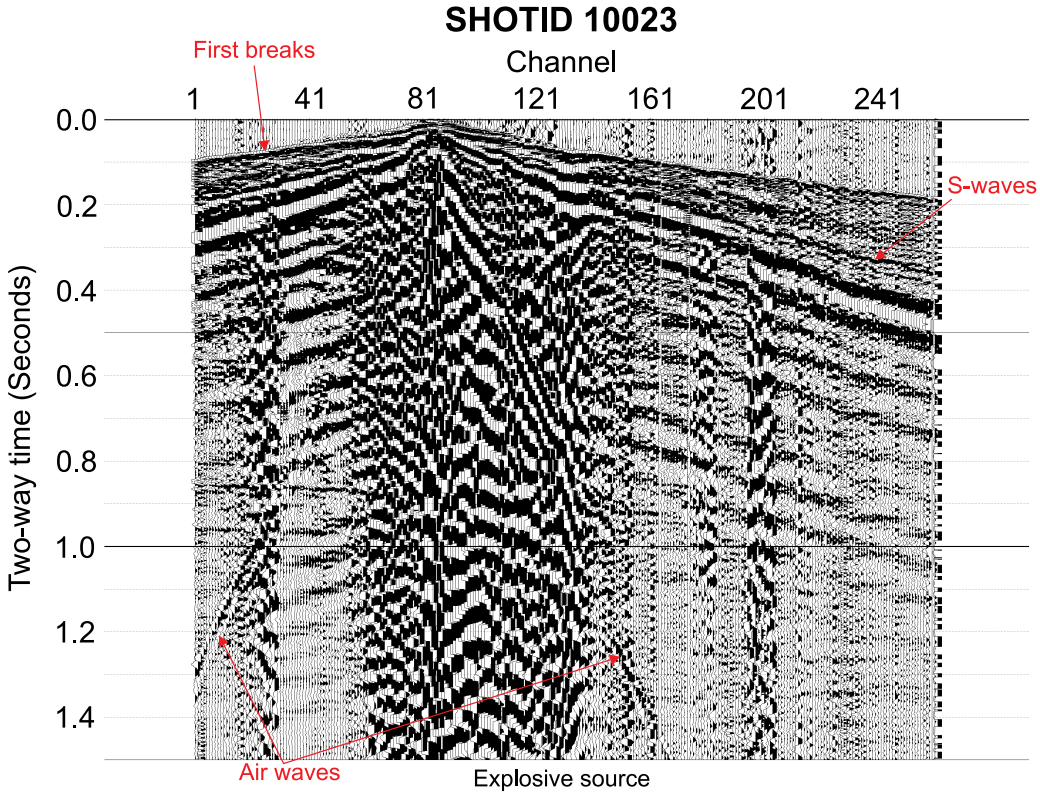

Figure 17. Shot gather from an explosive source. On SM1 it was not possible to test and compare the performance of explosive and drop hammer sources on the same source location, this was done on SM3 (Figure 1). Automatic Gain Control (AGC) has been applied before plotting.

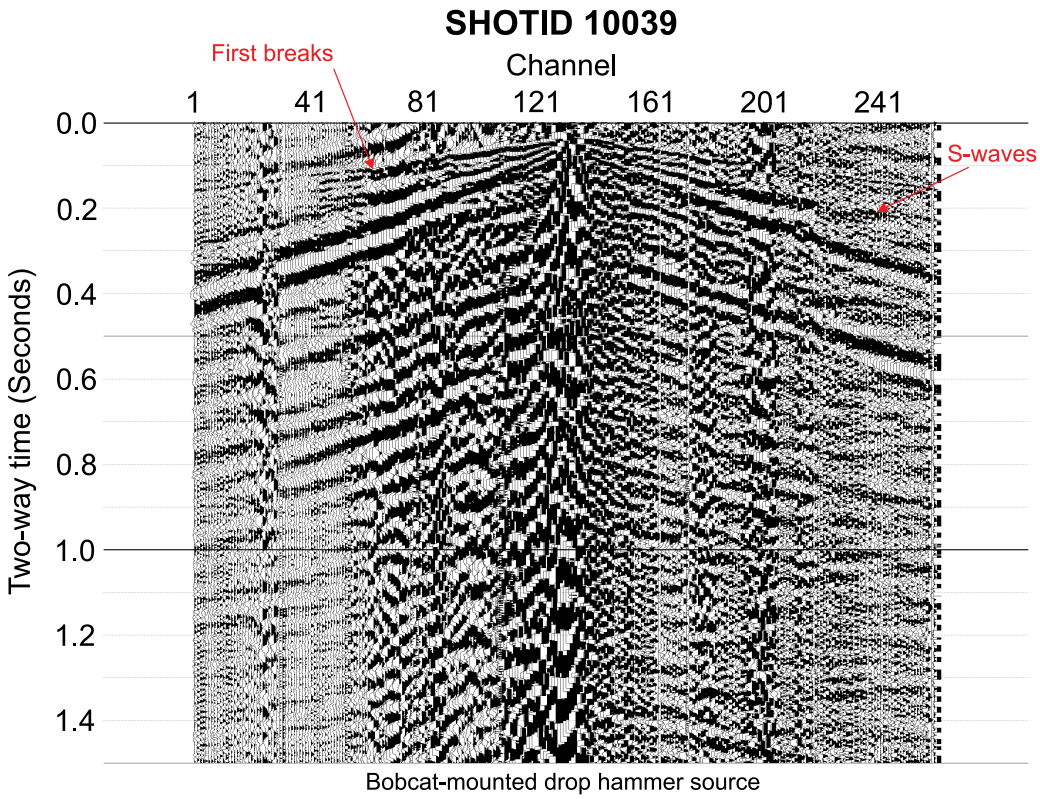

Figure 18. Shot gather from a drop hammer source. On SM1 it was not possible to test and compare the performance of explosive and drop hammer sources on the same source location, this was done on SM3 (Figure 1). AGC has been applied before plotting.

4.1.1. Geometry and static corrections

To set up geometry of the survey line, information on the receiver and source peg coordinates, receiver peg identification values, active channels, shot points and FFIDs are needed. The information was used to create a CMP geometry for the survey line. The geometry created has 544 CMPs with 2.5 m bin spacing, 4 m bin size along the line and 16 m bin size perpendicular to the line. All 17669 traces fell within the 16 m perpendicular bin size. The CMP geometry was then applied to the data.

Static corrections are applied to correct time delays caused by variable overburden thicknesses and velocities and the effects of elevation variations. Weathering and overburden materials create a low-velocity near-surface layer. This layer can consist of multiple layers with distinct seismic velocities. Aim of static corrections is to determine the delays caused by the low-velocity layer and to correct the data to a constant datum level such that the low-velocity layer and elevation changes do not affect the traveltimes of the reflection signals (Figure 19). The effect of the low-velocity layer is corrected with

refraction and residual static corrections. Refraction static corrections are applied after adding the geometry, while the residual static corrections are calculated and applied just before stacking the data (Figure 16). Correction to a datum is performed by first applying floating datum statics and then correcting the data to a constant datum with final datum statics after stacking the data.

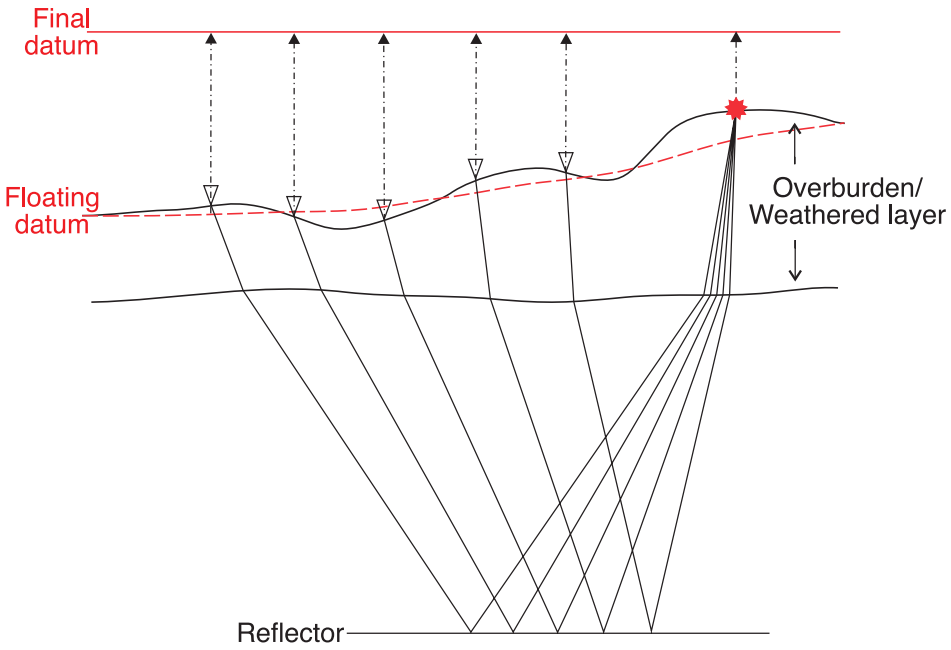

Figure 19. Effect of low-velocity overburden/weathered layer on the measured data. After static corrections, the data is moved to a floating datum and later after staking the data to the final datum. In the final datum, the reflections appear as if the sources and receivers had been on the same datum, i.e., the final datum.

With first-break pics and geometry information, a layered shallow subsurface velocity model can be created, based on which refraction statics can be calculated. First arrivals seen on a shot gather are usually refracted energy associated with the base of a weathering layer (Sheriff 1995, p. 228). The quality of the first breaks depends on the source and the near-surface conditions. Picking of first breaks close to the sources was difficult due to noise. Automatic first-break picking was used for initial picks, but all of the first breaks were checked and corrected manually. Multiple shallow subsurface velocity models were created to find a model with a good fit to the data. The models are based on the first-break picks and assumed P-wave velocities. The static time delays are calculated using a ray-tracing approach (Woodward 1991); with inversion, the difference between the calculated and the first arrival traveltimes is minimized as the layer velocities and boundaries vary iteratively. Field and residual refraction static corrections are extracted from a model with the ray-tracing approach. Field statics are sufficient in solving the long-wavelength static

anomalies, while the residual statics estimate short-wavelength variations. Both the field and the residual refraction static corrections were tested for the data but eventually only the field refraction static component was applied for the data.

Two of the shallow subsurface velocity models, a 3-layer and a 2-layer model, are presented in Figure 20. Both of the models have a good fit to the data (root-mean-square, i.e., rms, misfits of 2.66 ms and 1.84 ms, respectively) and exhibit similar trends, also present in the other models created. Both of the models have a low-velocity layer in the middle while on the sides, higher velocities reach closer to the surface. Refraction static solutions extracted from the models caused only a slight difference to the stacked data and in the end, the refraction statics extracted from the 3-layer model were used.

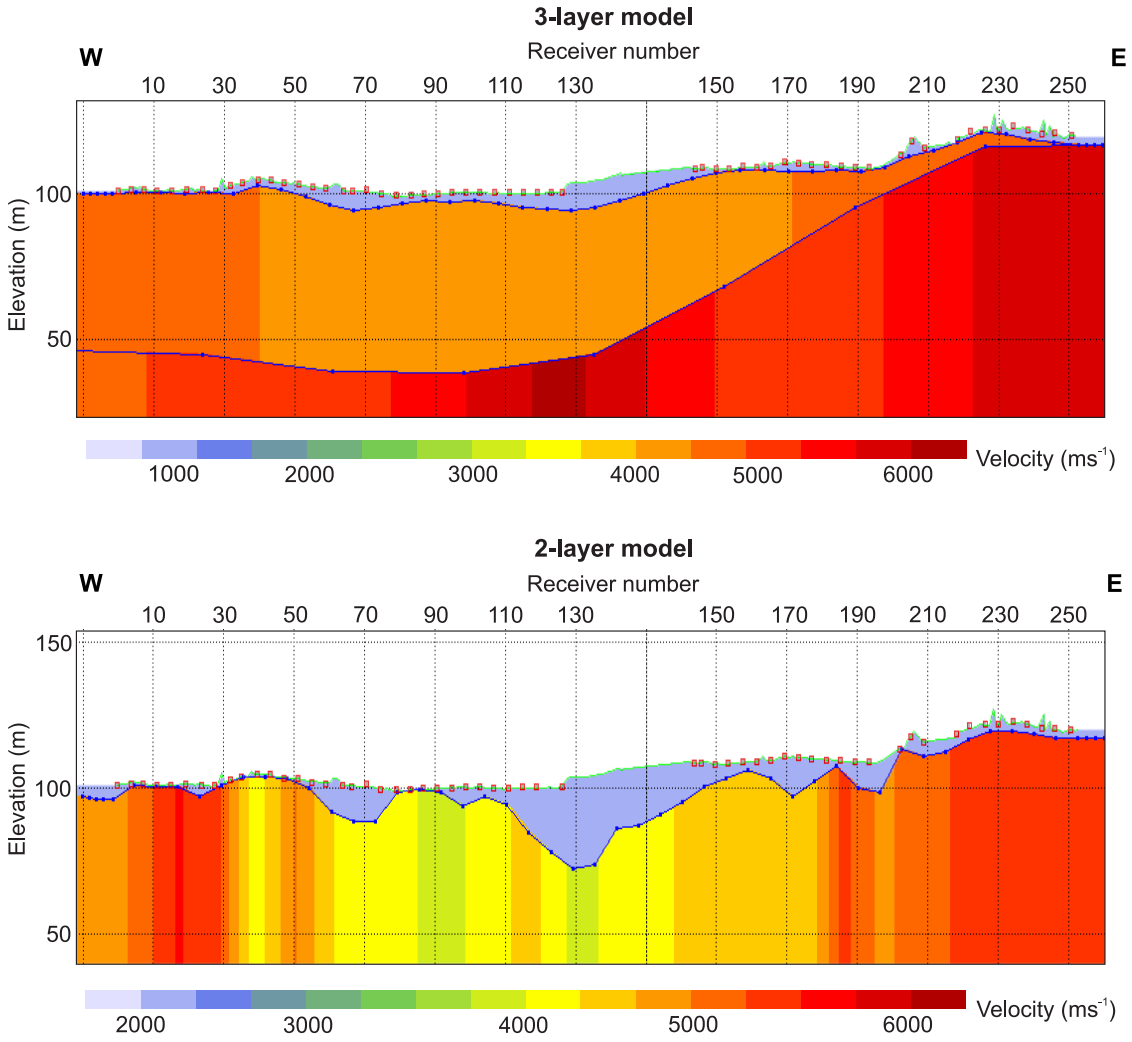

Figure 20. Two near-surface velocity model solutions for SM1 generated based on the first-break picks, geometry information and assumed P-wave velocities. Above is a 3-layer model (rms misfit 2.66 ms) and below a 2-layer model (rms misfit 1.84 ms). The blue dots are variation points of the models. The red squares are source points along the line (Figure 10). As seen from the source points, there were no sources nor receivers in the middle of the line due to the railway.

After refraction static corrections, the data were moved to a floating datum (Figure 19), to avoid large elevation static shifts before normal move-out (NMO) correction and stacking of the data (see section 4.1.4). Large shifts would cause distortion on the NMOs of reflection events. Replacement velocity of 5000 ms^{-1} was used for all the static corrections.

To improve the static corrections and the final stack, a set of surface-consistent residual statics corrections were calculated in a cycle with velocity analysis and NMO corrections (see section 4.1.4). With the residual statics, the velocity model for NMO correction can be improved and with the improved NMO correction, the residual statics can be improved and so on. The cycle is repeated multiple times to improve the velocity model and by that to improve the NMO correction and the residual statics. The residual statics are calculated by cross-correlating pre-stack traces with a pilot trace based on the CMP stack within a designed time window. The surface-consistent residual statics are based on stack power maximization (Ronen and Claerbout 1985). Multiple different time windows were tested for the residual static correction, in order to find a solution which works well with the shallow subsurface but doesn't distort deeper features. The cycle of improving the velocity model, NMO correction and residual statics was repeated 5 times. The final residual statics were calculated twice to improve the solution; first with a time window of 200–1500 ms and then with a time window of 150–1000 ms.

Lastly, after stacking the data, the final datum statics were applied to the data (Figure 19). The final datum was fixed to 100 m above the sea level with a replacement velocity of 5000 ms^{-1}.

4.1.2. Amplitude corrections

Amplitudes of seismic waves depend on multiple factors (Sheriff 1975). Some of the factors like source strength and coupling, scattering, geophone sensitivity and coupling, instrumentation, array directivity and superimposed noise, are independent of the subsurface. Factors like spherical divergence, raypath curvature, absorption, multiple reflections, reflection coefficients, curvature of the reflectors and incident angle depend on the subsurface. Amplitude corrections aim to compensate for the different factors affecting the amplitudes.

Spherical divergence, referring to the attenuation of wave amplitude due to geometrical spreading of the wavefront (see section 2.1.1), has a substantial effect on the observed amplitude spectrum at depth. To correct the spherical divergence along SM1, all traces were multiplied with an exponential scaling function of time:

$$g(t) = t^{\alpha} \tag{4.1}$$

Where t is time and α is the exponent chosen. With the right exponent, a balance between earlier and later times should be achieved (Figure 21). Values between 1.1–1.2 seemed to deliver the best results, and in the end exponent value of 1.2 was chosen for the data. For absorption, no specific correction was applied.

Air waves and noisy traces were removed from the data with muting. Muting sets values to zero within a designed mute interval. High-amplitude traces were muted by calculating rms (root-mean-square) amplitudes for each trace within a specified time window and muting the high-amplitude traces based on a defined rms limit. The air waves were muted using a specified velocity and a time zone around the velocity. Air waves travel with the velocity of sound ~330 ms^{-1}, which was used for the muting. The same function was used to attenuate S-wave arrivals, which were found to disguise the shallow subsurface reflectively. The disguising effect of the S-waves was emphasised especially after stacking the data. The S-waves were attenuated using a velocity of 2700 ms^{-1}. Figure 22 shows the effect of muting and attenuating the air and S-waves. The shot gather 10023 is used as an example to show how the processing steps affect the data.

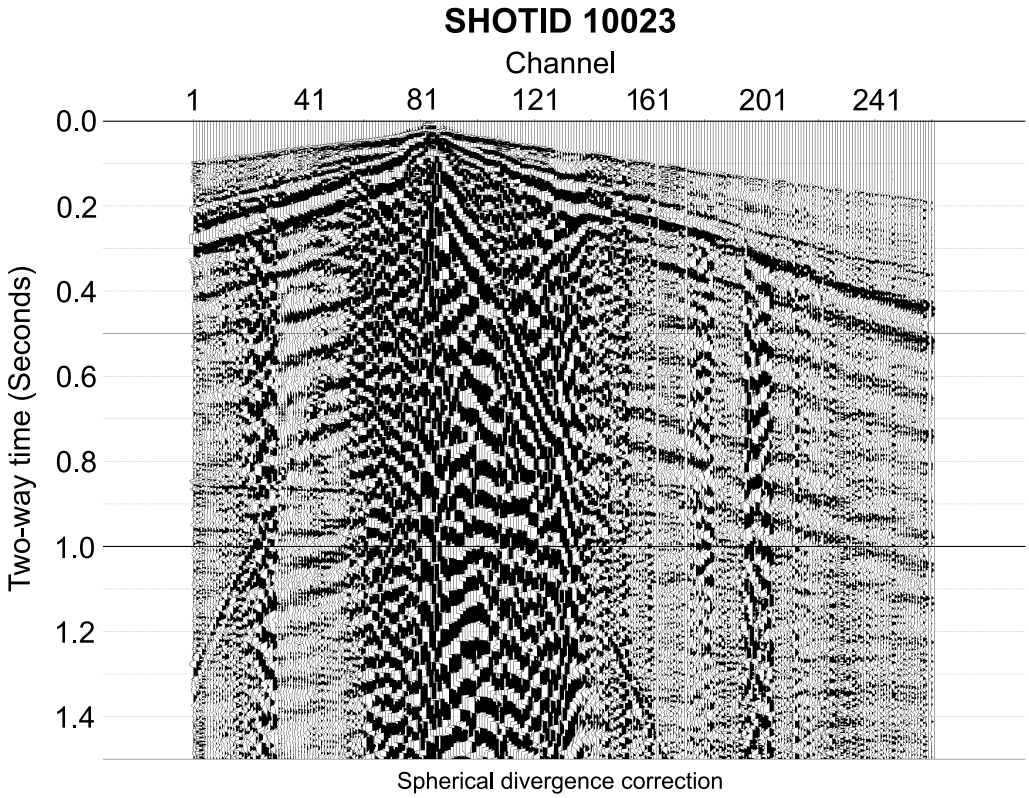

Figure 21. Static corrections and spherical divergence applied to the shot gather 10023. Manually picked noisy traces have been removed. AGC has been applied before plotting.

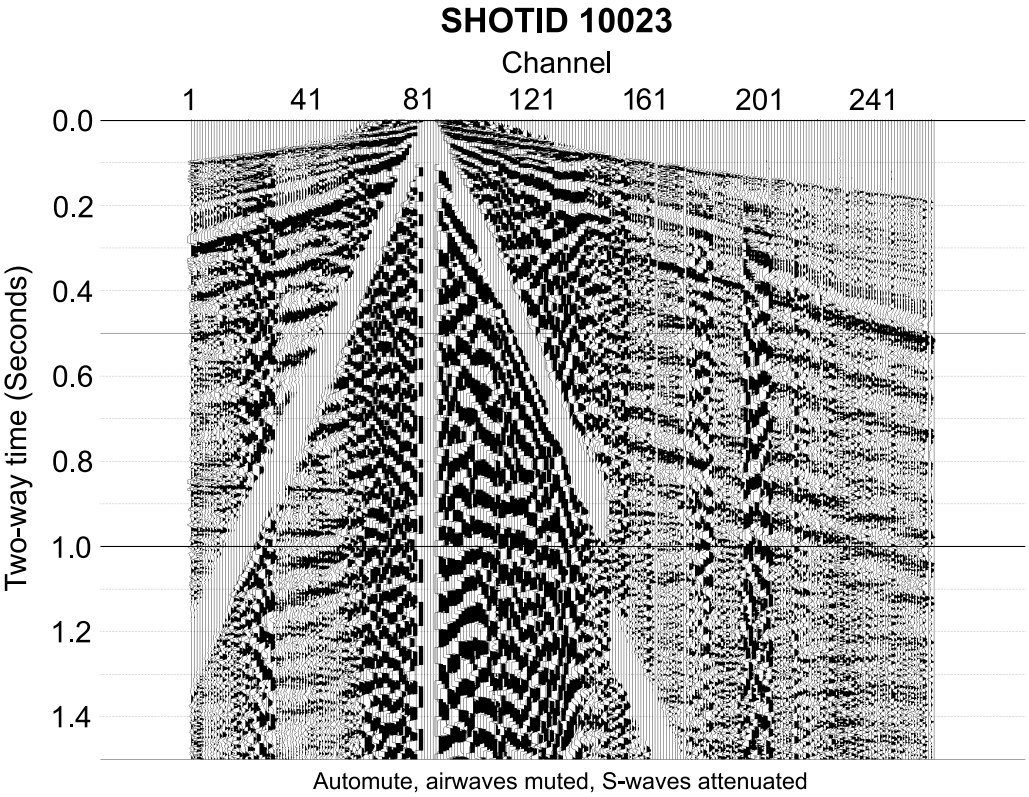

Figure 22. In addition to the corrections applied in Figure 21, automatic muting has been applied, air waves have been muted and S-waves attenuated. AGC has been applied before plotting.

Automatic gain control (AGC) was used to scale the input signal variations. The AGC function multiplies each sample of a trace with a scaling factor. The scaling factor is calculated within a given time window so that the average amplitude over the window length (500 ms in this case) is constant down the trace. The scaling factor is constant for each trace, scaling the traces both horizontally (spatially) and vertically (time). AGC improves the visualization of the reflective events but alters the frequency content (signal characteristics) of the data as it is a non-linear operator. Because of this, the data were also alternatively trace balanced, which only affects the traces spatially as opposed to the AGC. The balance function scales the amplitudes to vary around a certain amplitude leading to an evenly distributed energy within the section. The balancing function can be fixed to specific time windows or set equal for the whole traces. Whole-trace balancing was tested simultaneously with the AGC and both lead to similar results with slightly different contrasts. However, it was noted that for visualization and interpretation in the Gocad 3D modelling environment (see section 5.1.2), the AGC produces better-balanced images. Additionally, the whole-trace balancing was applied later in the processing flow after stacking the data for visualization purposes (Figure 16).

4.1.3. Frequency filtering

Frequency filtering is applied to enhance the reflected signals by filtering out noisy frequency spectrums unnecessary for the reflective signals, e.g., surface waves, and hence increasing the signal-to-noise ratio. A wide frequency bandpass, including the lower frequencies, is desirable, however, typically a compromise needs to be made between the unwanted and wanted factors. Different bandpass filters were tested for the SM1 data to find which frequencies are dominated by noise and which reveal the reflected signals. The different frequency bands tested show that most of the noise (caused by surface waves) is dominating the low frequencies below 40 Hz (Figure 23). The most optimal frequency spectrum for the reflective signals is between 30–80 Hz (Figure 23). The higher frequencies show signs of the reflections, but these are more smudged with the background (Figure 23). Despite the reflective signals seen at 30–40 Hz frequencies, the upper value for the bandpass filter was set to 50 Hz, as excluding the lower frequencies improved the signal-to-noise ratio on the final stack. The applied bandpass frequency filter had a lower value of 50 Hz, an upper value of 150 Hz, and taper values of 40 Hz

and 170 Hz for a smoother transition (Figure 24). Taper values are used to reduce signal ringing caused by the Fourier transform used for the filtering.

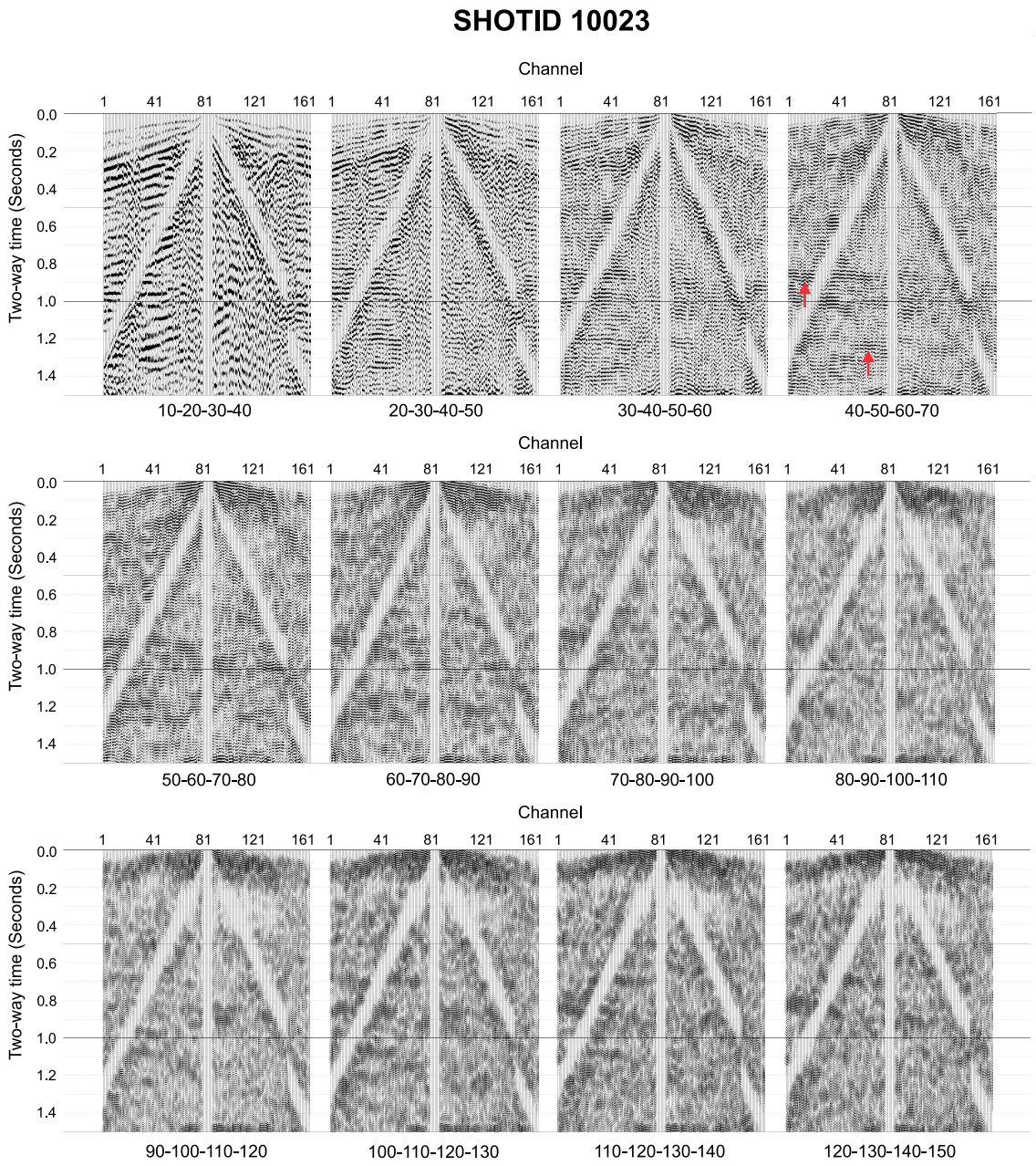

Figure 23. Comparison between different bandpass filters. Examples of reflective events are shown with the red arrows on the data filtered with a 40-50-60-70 Hz bandpass.

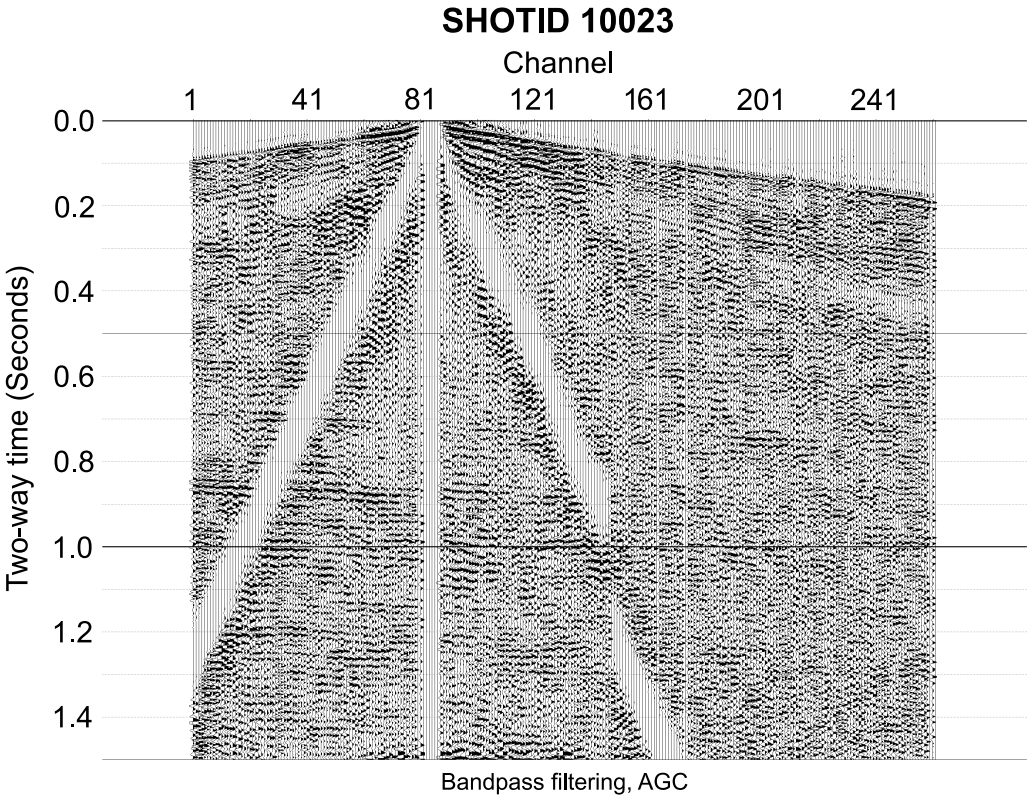

Figure 24. Shot gather after bandpass filtering and AGC. The bandpass filter used had a lower value of 50 Hz, an upper value of 150 Hz and taper values of 40 Hz and 170 Hz (40-50-150-170 Hz).

In addition to frequency filtering, the signal-to-noise ratio can be improved using deconvolution. Deconvolution aims to restore the shape of a waveform to a form prior to any filtering effects due to the subsurface and the acquisition system. Various algorithms were tested for deconvolution, with unsatisfactory results. In the end, a frequency-domain post-stack f-x deconvolution was applied to the data after stacking (Figure 16). The f-x deconvolution attenuates noise by performing a Wiener deconvolution for each frequency in the horizontal direction.

4.1.4. Stacking and velocity analysis

With CMP stacking, the reflective signals are strengthened, and noise weakened by summing up traces with the same CMP point (see section 2.1.3). Before CMP stacking, the traveltime delays caused by source and receiver offset should be removed with an NMO correction (see section 2.1.3). The function used for the NMO correction links the measured time with the zero-offset time, the offset distance and the rms velocity of the subsurface to calculate the NMO. Rms velocity is the square of an average velocity from

the ground surface to a reflective surface. To be able to correct for the NMOs, first several constant-velocity NMO corrections were tested with velocities ranging between 4000 ms^{-1} and 7000 ms^{-1} to create a simple NMO velocity model for initial stacking of the data. This velocity model was then used to create a detailed velocity model for the NMO corrections, by inspecting responses of individual reflections to different velocities (Figure 25). The velocity model for the NMO correction was improved multiple times in a cycle with the time-variant residual statics (see section 4.1.1). Figure 26 shows the NMO-corrected and CMP-stacked data.

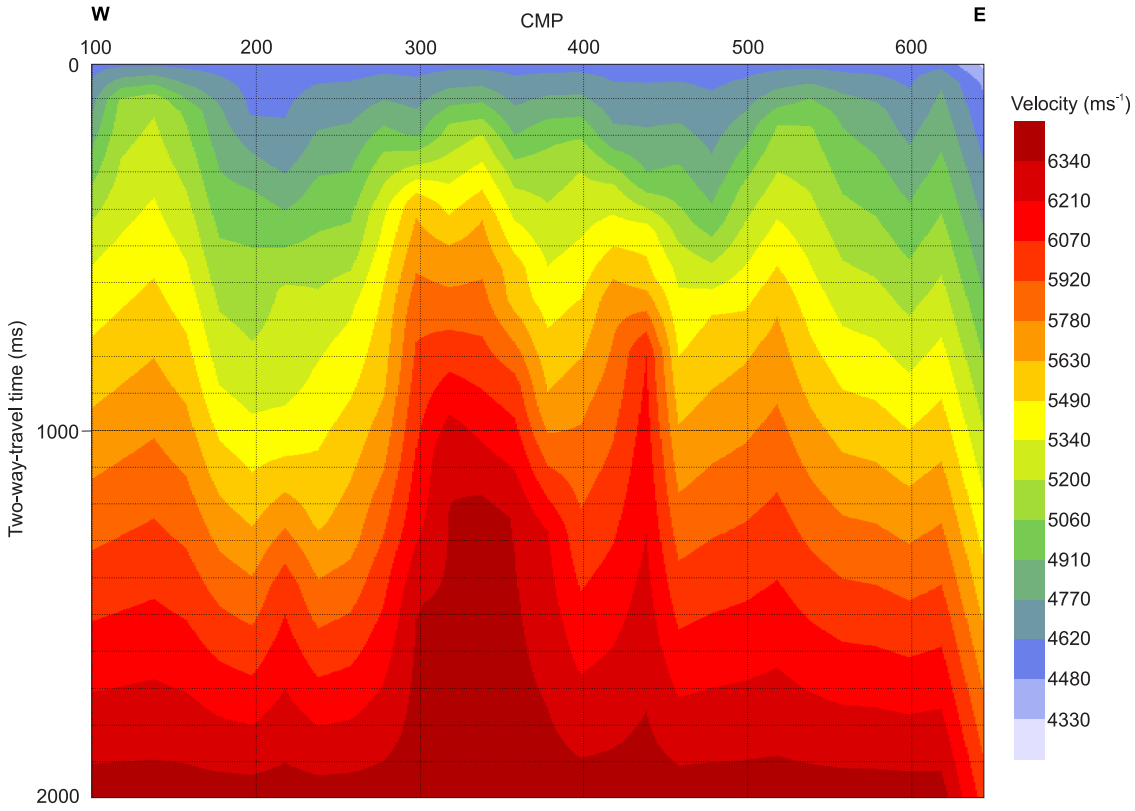

Figure 25. The final velocity model created and used for the NMO correction. The velocities are represented with respect to the two-way traveltime and the CMP number (Figure 10).

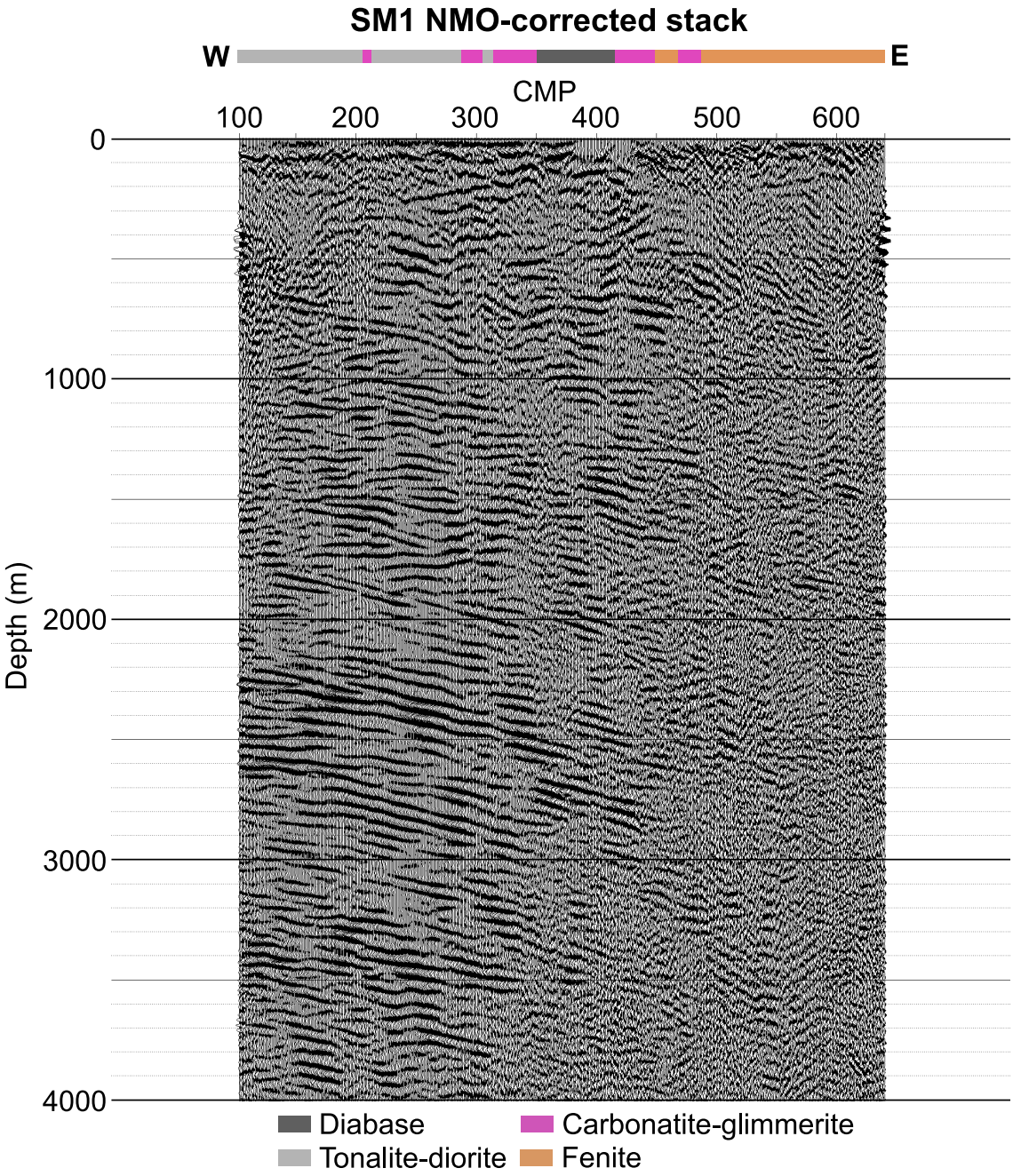

Figure 26. NMO-corrected and CMP-stacked data from SM1. The velocity model in Figure 25 was used for the NMO correction. Post-stacking processing steps like f-x deconvolution and additional filtering, balancing and AGC have been applied to the stack (Figure 16). The geology bar has been extracted from the known surface geology. See Figure 10 for the geology and CMP locations. The seismic section is shown with 1:2 horizontal exaggeration.

4.1.5. Migration and time-to-depth conversion

Migration of seismic data repositions dipping reflections to their true positions and collapses diffractions caused by pointwise reflectors, increasing the spatial resolution. Prior migration, the seismic events are positioned with respect to the observation points,

in stacked data this refers to the CMP points. In the stacked data, each event is located vertically below a CMP point, which differs from the true subsurface position of the reflector (Figure 27). Relationship between true and apparent dips of a reflection can be stated as:

$$tan\xi_a = sin\xi \tag{4.2}$$

where ξ_a is the apparent dip of the reflective interface and ξ is the true dip of the interface.

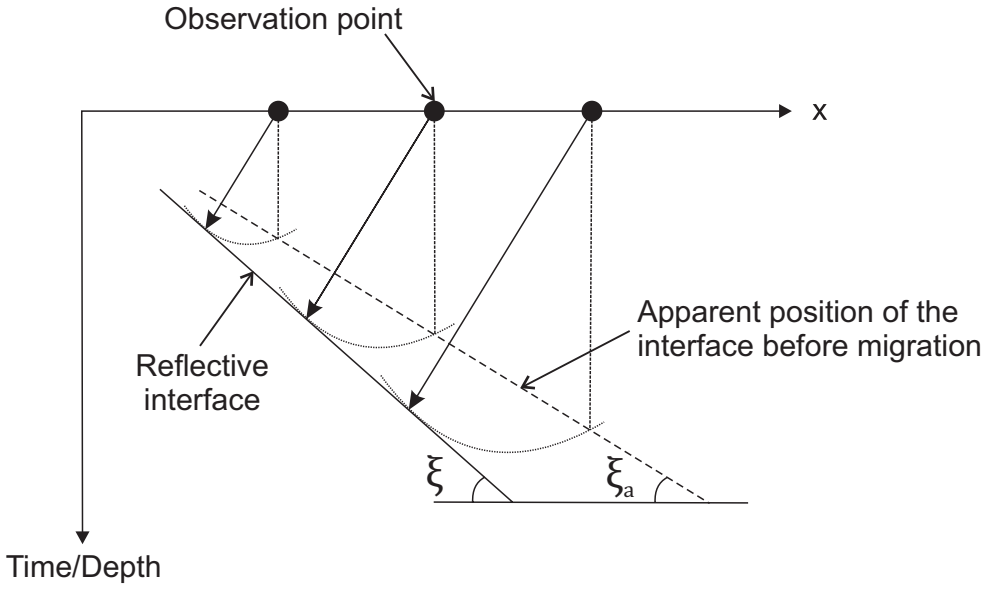

Figure 27. The principle of migration. Migration moves dipping reflections to their true subsurface positions. The graph shows the apparent and true positions of the reflective interface and their dipping angles ξ_a and ξ, respectively.

Migration is typically performed after stacking but a more intricate pre-stack migration can also be carried out. Pre-stack migration may give better results especially in areas with a complex velocity distribution. Generally, a migration algorithm assumes all of the data elements to be either primary reflections or diffractions. Because of this, noise in the data will also be migrated. Hence, it is essential to carefully process the data prior to migration when most of the noise can be removed. To perform the migration and create a good image of the subsurface, knowledge on the velocity distribution is needed. Migration can be performed with several different algorithms. For SM1, a post-stack migration was carried out using the Kirchhoff migration algorithm (Figure 28). Kirchhoff migration is based on integrating along diffraction curves with the Kirchhoff equation and position the integration results at the crests of the diffraction curves (Schneider 1978).

A simple 3-layer velocity model (5100 ms^{-1} for 0–500 ms, 5200 ms^{-1} for 500–2000 ms and 6000 ms^{-1} for >2000 ms) was used as a constraint for the migration algorithm.

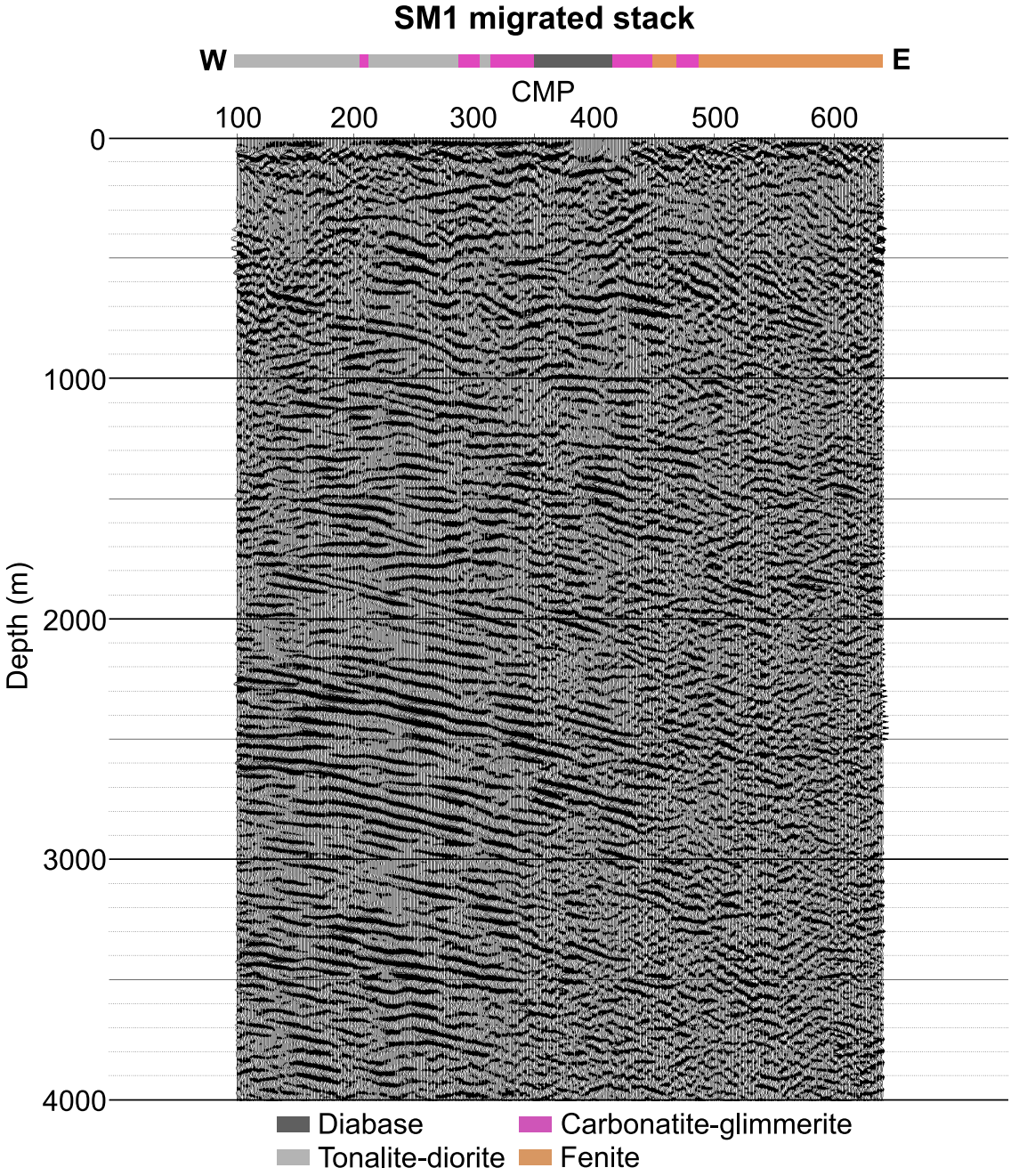

Figure 28. The migrated stack from SM1. The migration was done using Kirchhoff's migration algorithm. Post-stacking processing steps like f-x deconvolution and additional filtering, balancing and AGC have been applied to the stack (Figure 16). The geology bar has been extracted from the known surface geology. See Figure 10 for the geology and CMP locations. The seismic section is shown with 1:2 horizontal exaggeration.

After migration, additional filtering, balancing, AGC, f-x deconvolution and semblance-smoothing, a coherency filter, were applied to the stacked data to enhance the reflective features and the visual representation of the stack. The semblance-smoothing uses a

similar algorithm as described by Milkereit and Spencer (1989) to compute trace semblances by utilizing local coherency. To present the data in the depth domain, a time-to-depth conversion was performed for the processed stack. The conversion requires a defined velocity model as a constrain. A velocity model with a constant velocity of 5500 ms^{-1} was chosen for the conversion so that the stack would be comparable with the two other reflection seismic lines SM2 and SM3 converted to the depth domain with the same velocity (McKevitt, B., MSc thesis in preparation).

4.2. Processing of GPR data

Processing of GPR data is analogous but much simpler compared to the processing of reflection seismic data. Reflexw software, produced by Sandmeier geophysical research was used for GPR data processing (Sandmeier geophysical research 2018). The software has been developed for processing and interpretation of waveform data. The processing workflow applied to the GPR data is presented in Figure 29.

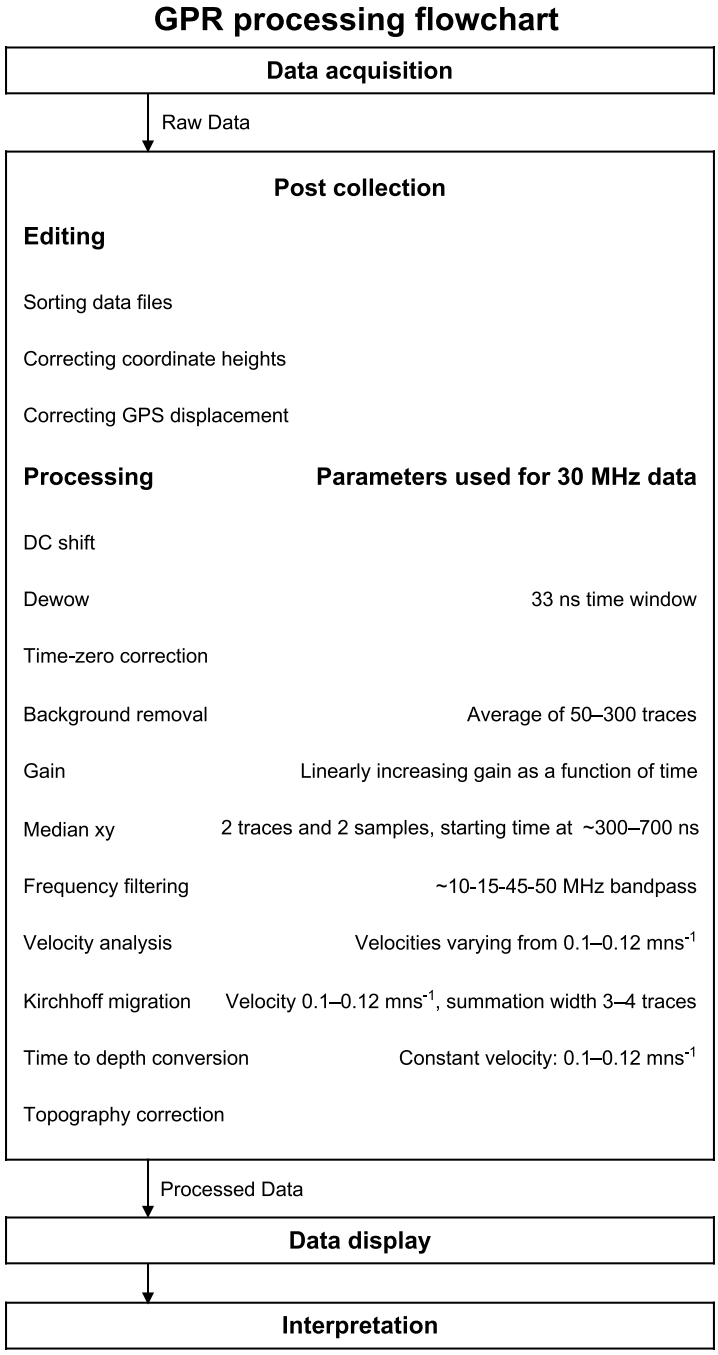

Figure 29. Processing workflow applied to the GPR data.

Before importing the raw GPR data to the processing software, the coordinates were replaced with the high-precision coordinates. In addition, the displacement between the surveyor and the measurement point was corrected by adding ten to each trace number (displacement divided by trace spacing, 8.67/0.83≈10.4) (see section 3.2). After the correction, the error margin between the coordinates and the actual subsurface positions is approximately 30–40 cm.

4.2.1. Time-zero correction

In the raw GPR data, air- and ground waves are the most dominating features, but subsurface reflectivity can be observed beneath these (Figure 30). Due to the transmitter and receiver offset (~6.15 m in the case of the 30 MHz antenna used in Siilinjärvi), the reflection signals have a time delay with respect to the case of vertical incidence, i.e., NMO (see section 2.1.3). Time-zero correction is used to move the GPR recordings to start from the onset of the first-break signal caused by the air wave (Figure 30). In the correction, GPR data is treated as if the transmitter and receiver would be in the same position and have zero offset, even though in reality the transmitter and receiver are usually, also in this case, separated by some distance (Figure 9). In zero-offset data, the air wave should have reached the receiver as soon as the signal was sent by the transmitter, and typically in time-zero correction, the time before the first arrivals is simply removed. To be precise, the time delays, caused by the antenna separation, should be subtracted from the traveltimes as a whole with an NMO correction. However, this is rarely done as the depth distortion of the primary reflections is fairly small, i.e., reflections below the air and ground waves, and other processing steps usually work adequately without the NMO correction (Neal 2004).

The time delays due to the antenna separation cause distortion to the reflector depths and they appear to be at a greater depth than their true position. The depth difference between the common- and zero-offset data increases with larger antenna separations and decreases with depth. In particular, at shallow depths (0-5 m from the ground surface) the traveltimes to the reflectors are longer for common-offset data compared to a zero-offset data, causing larger depth distortion. For example, a reflector at one-meter depth in zero-offset data would be at 3.2 m depth for 30 MHz common-offset data with 6.15 m antenna separation. At 5 m depth, the difference reduces to 90 cm and at 10 m depth to 45 cm. The possible distortion should be considered while interpreting shallow features from the data especially due to the long antenna separation of the 30 MHz antenna.

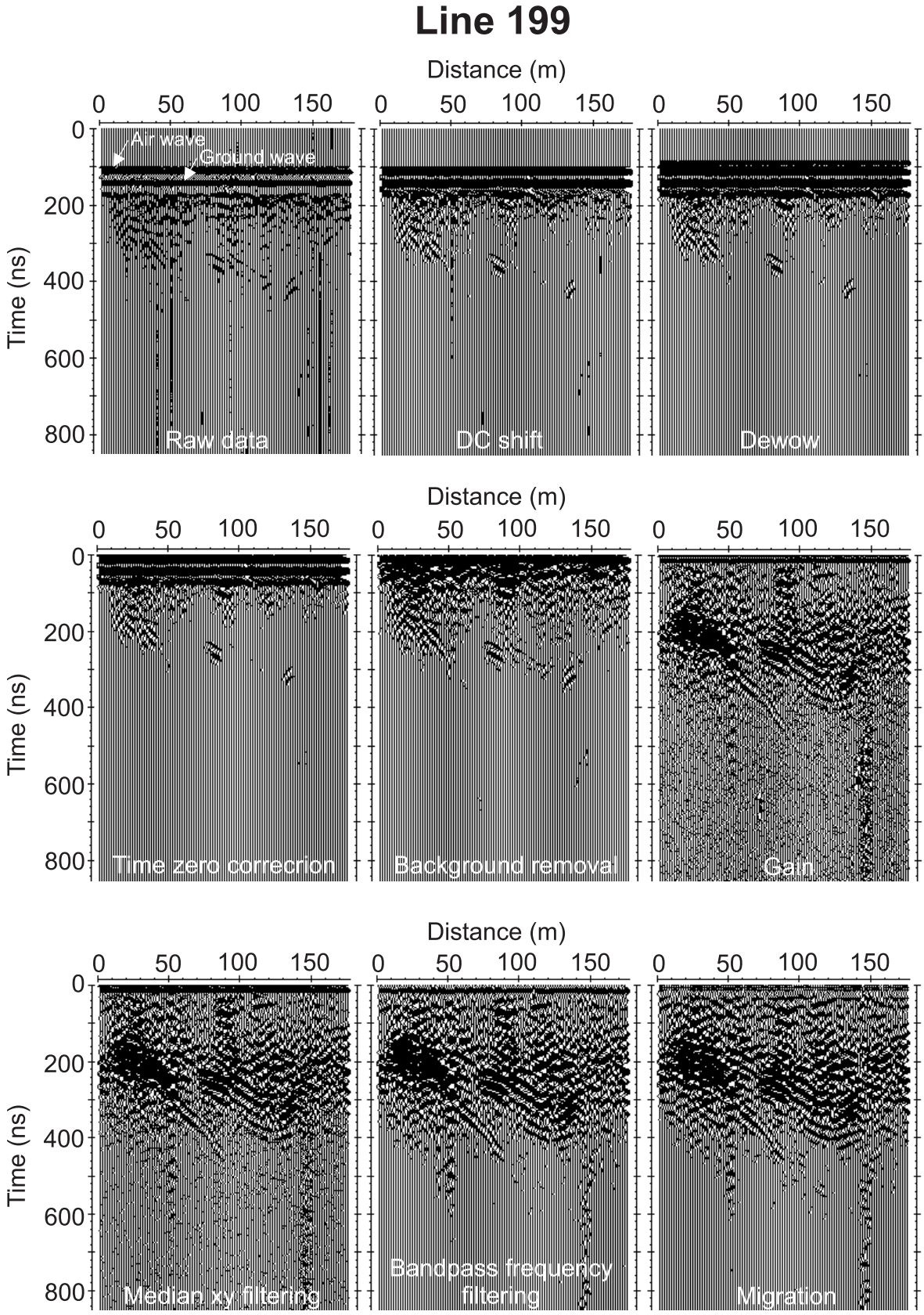

Figure 30. The processing steps applied for the GPR data shown for the profile 199 (Figure 12). The processing workflow is presented in Figure 29.

4.2.2. Amplitude corrections and filtering

Electronics of the GPR device cause a direct current (DC) shift resulting in a mean amplitude displacement from zero. With a DC shift correction, the data are shifted to alternate around the zero amplitude (Figure 30). This can be done by using the average amplitude before the first arrivals to shift the data. For the 30 MHz data the time used varied from 87–106 ns within the acquired lines. The GPR profile 199 (Figure 12) is used as an example to show how the processing steps affect the data (Figure 30).

Dewow (subtract-mean) is a high-pass filter used to filter out a slowly decaying low-frequency component 'dewow' caused by signal saturation of the receiving antenna (Figure 30). The signal saturation is caused by the large energy input of air waves, ground waves, near-surface reflections and the short time interval between the transmitted signals (Fisher et al. 1992). A time window, which should be approximately one principle period, needs to be set for the filter. For 30 MHz data, time window of 33 ns was used.

Background removal is used to suppress air and ground waves (Figure 30). This was done by subtracting an averaged trace. The averaged traces were calculated over 50–300 traces, and the affected time area was restricted by setting the starting time between 20–25 ns.

Gain is applied to correct the decaying of amplitude due geometrical spreading of the propagating wavefront and due attenuation of amplitudes, similar to the seismic data (see section 4.1.2). A manual gain function was designed to boost the amplitudes in later times. Simple linear gain functions were found to produce good results, boosting the signals at later times with minimal strengthening of noise (Figure 30).

The acquired GPR profiles contain varying amounts of partly pixelated, noisy traces. Median xy, a 2D filter was used to filter such noise (Figure 30). It suppresses both trace- and time-dependent noise by calculating a median for each time step over a selected xy area. The suppressing effect of the filter may decrease data resolution. To avoid losing resolution a later starting time was set for the filter (300–700 ns) and it was focused on small areas (2 traces and 2 time samples).

A bandpass frequency filter is applied to remove high- and low-frequency noise (Figure 30). The bandpass values should vary around the center frequency. For example, for the 30 MHz data, the bandpass values were approximately 15 and 45 MHz. The taper values were set approximately to 10 and 50 MHz to create a softer edge for the filter, as was done for the seismic data (see section 4.1.3). The optimal filter values were defined with the aid of frequency spectrums. For noisy data, the bandpass frequency filter was additionally applied later in the processing flow, for example after migration or after repeated median-xy filtering, to suppress the noise caused by these processing steps.

4.2.3. Velocity analysis and migration

Information on the subsurface velocities is vital for the successful correlation of GPR profiles and drilling data (Francke 2012). Knowledge of the electromagnetic wave velocity is also important for the migration (for the principle of migration see section 4.1.5). To gain a better understanding of the subsurface velocities, velocity analysis was done for the data. On common-offset GPR data, the subsurface velocities can be analysed by fitting curves to diffraction hyperbolas. The GPR profiles had only a few diffraction hyperbolas available for the velocity analysis from. However, the velocities analysed from the diffraction hyperbolas varied between 0.1-0.12 mns^{-1} and were used for the migration of the data. If diffraction hyperbolas were not present and velocity analysis could not be done, subsurface velocity of 0.1 mns^{-1} was assumed. Based on the electromagnetic wave velocities calculated from the relative dielectric permittivity values of different rock types in the Siilinjärvi deposit with Equation 2.12, the average velocities vary from 0.08 to 0.13 mns^{-1} (Table 4). Kirchhoff migration was found to be the most suitable migration algorithm for the GPR lines (Figure 30).

Table 4. Estimated relative dielectric permittivities and electromagnetic wave velocities of different rock types in the Siilinjärvi deposit. Values for relative dielectric permittivities from Davis & Annan (1989), Telford (1990) and Schön (2011a). The relative dielectric permittivity value of the Siilinjärvi carbonatite-glimmerite ore has been calculated for an average ore composition from Luoma et al. 2014 (65% micas, 5% amphibole, 15% calcite, 4% dolomite, and 10% apatite), with the relative permittivity values for the ore minerals from Olhoeft 1981 and Keller 1989 in Schön 2011a. The relative permittivity value of biotite was used for the mica. Because the diabase dykes have a basaltic composition (O'Brien et al. 2015), the relative dielectric permittivity value is considered to vary within the relative dielectric permittivity range of basalts 10–17 (Schön 2011), which is within the range of diabase (10.5–34.5) (Telford 1990). Value for fenite could not be estimated with the available references. The electromagnetic wave velocities have been calculated with equation 2.12 using the estimated relative dielectric permittivity values. The electromagnetic wave velocity for granite is from Davis & Annan (1989).

Rock type	**Relative dielectric permittivity ε_r**	**Electromagnetic wave velocity (mns^{-1})**
Carbonatite-glimmerite ore	6.4–9.2	0.1–0.12
Diabase	10.5–17	0.07–0.09
Fenite	-	-
Diorite	6	0.12
Gneiss	6–12	0.09–0.12
Granite	4–11	0.13

The final processing step applied for the data is the time-to-depth conversion. The conversion was done with the velocities used in the migration. Depth penetration of the GPR profiles varies between 600-800 ns which is approximately 30 m with a constant velocity of 0.1 mns$^{-1.}$ Elevation changes along the lines can be visualized with a topography correction. The correction uses elevation information attached with the coordinates to visualize the topography of a line. The processed GPR lines with a topography correction, and here with a time-to-depth correction using a constant velocity of 0.1 mns^{-1}, are presented in Figures 31, 32 and 33.

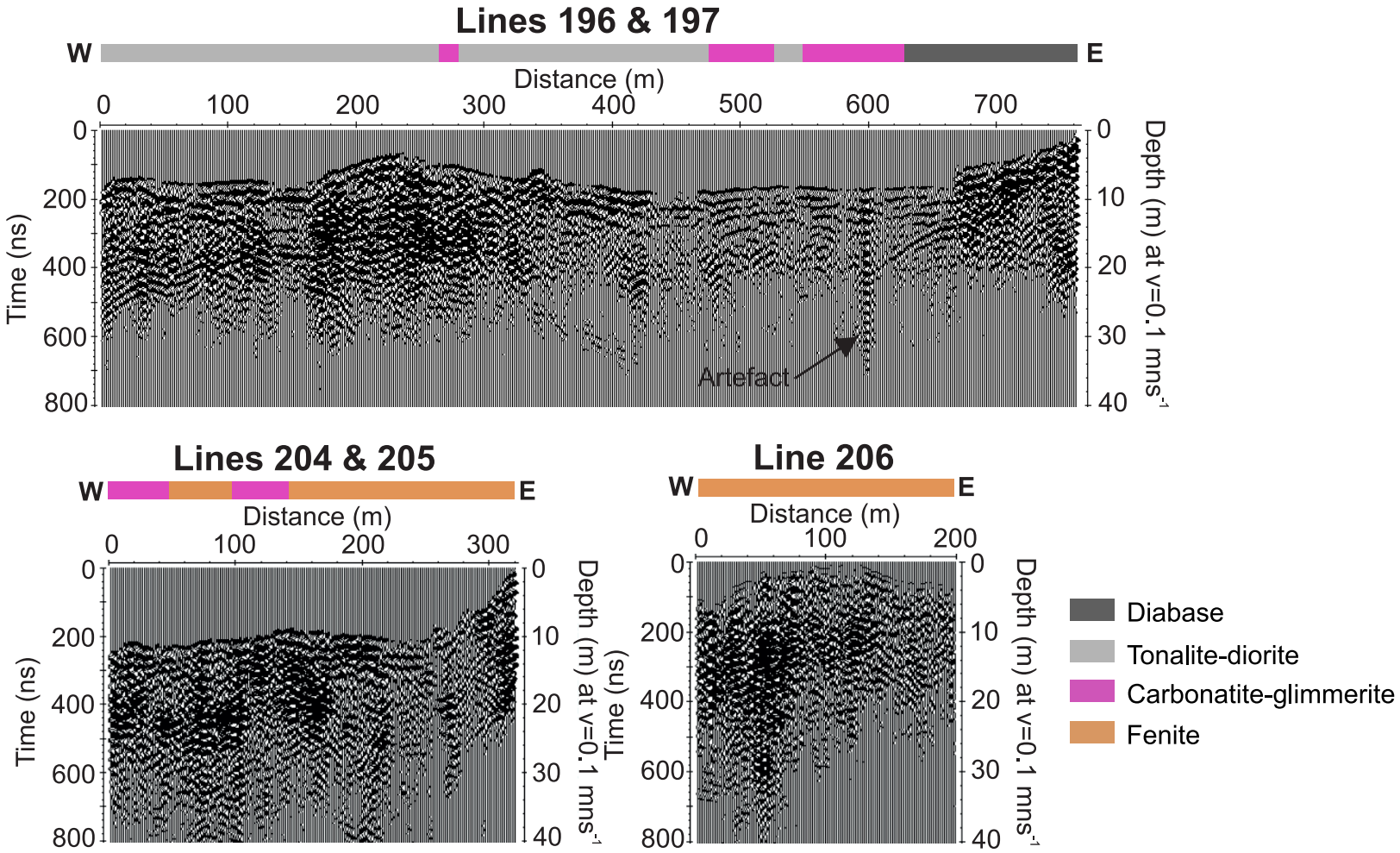

Figure 31. Processed GPR lines 196, 197, 204, 205 and 206 measured along SM1 (Figure 12). The geology bars have been extracted from the known surface geology (Figure 12).

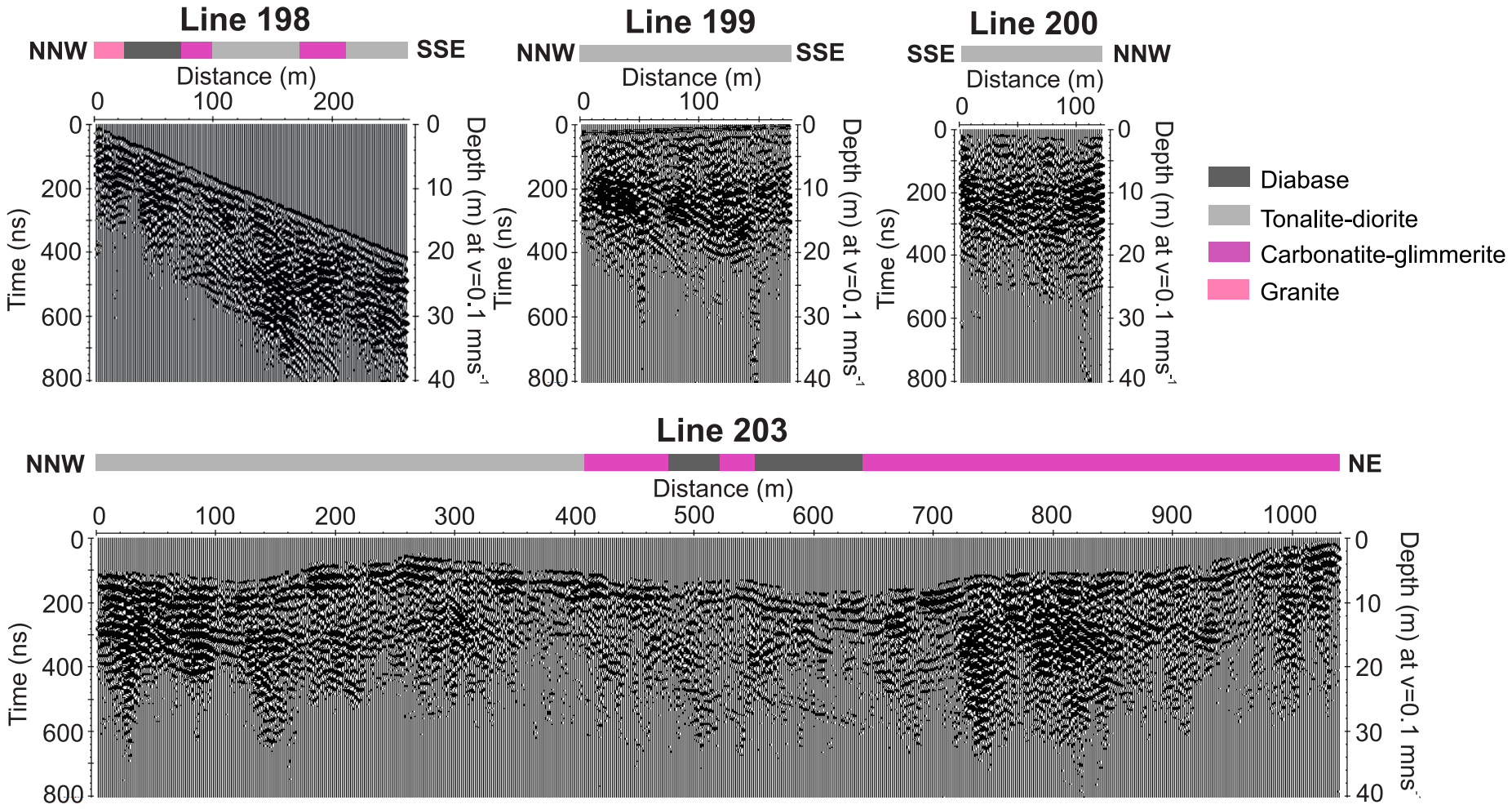

Figure 32. Processed GPR lines 198, 199, 204, 200 and 203 measured in the Särkijärvi pit (Figure 12). The geology bars have been extracted from the known surface geology (Figure 12).

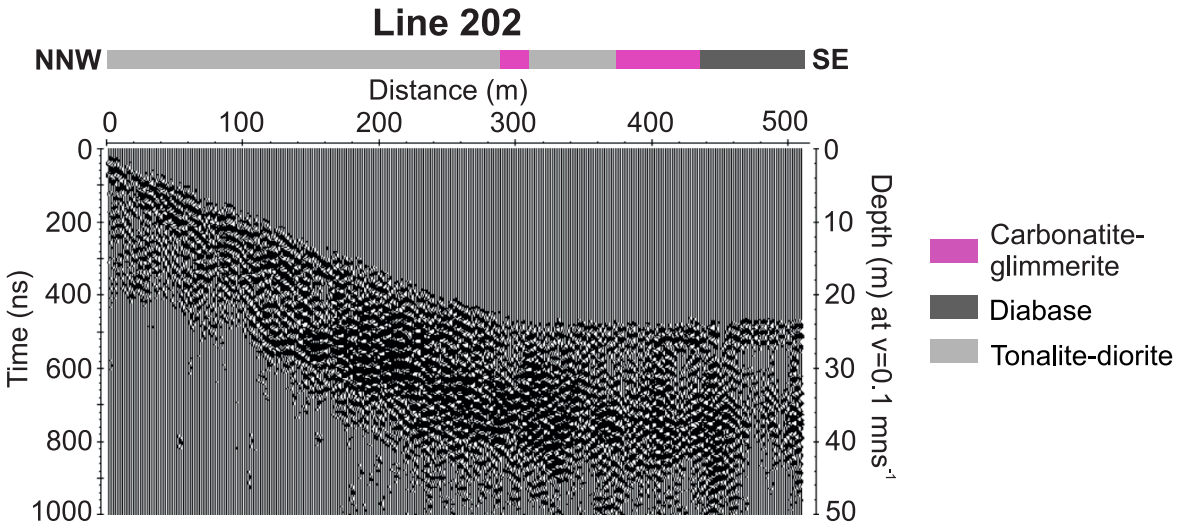

Figure 33. Processed GPR line 202 measured in the Särkijärvi pit (Figure 12). The geology bar has been extracted from the known surface geology (Figure 12).

4.3. Processing of magnetic data

The processing flow applied for the magnetic data is presented in Figure 34. A correction is needed to remove the effects of daily variation from the measurements made along the survey lines. Before the correction, data files from the magnetometers were sorted for each line. The daily variation was corrected with the magnetic total field measurements of the base stations. The magnetic total field is assumed to act linearly between each total field value measured. A correction for the daily variation is calculated by interpolating the deviations of the total field measurements with time. In this case the effect of the daily variation is tenuous as the scale of the correction is about 0–20 nT for all of the lines. The corrections and their effects are shown in Figure 35.

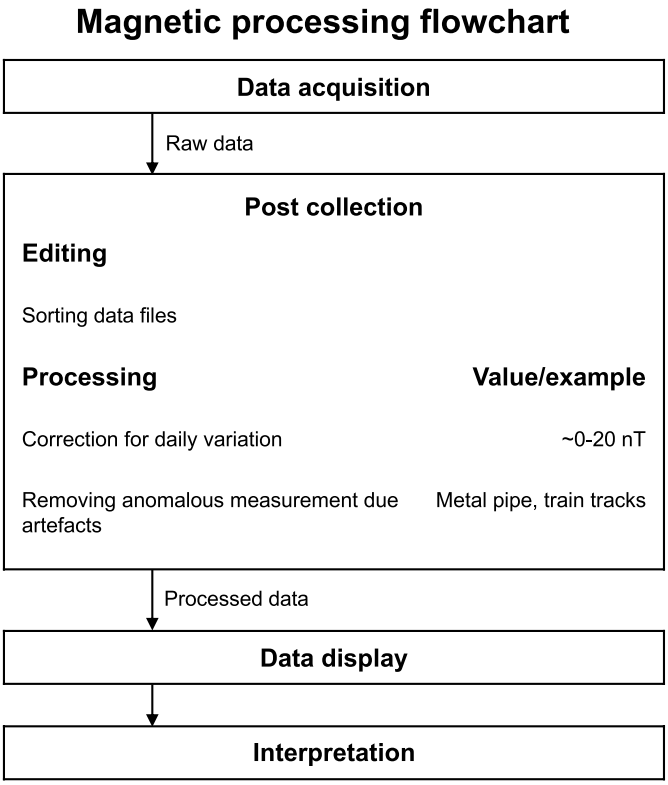

Figure 34. Processing workflow applied for the magnetic data.

Anomalous measurements caused by artefacts were removed from the measurements manually. For example, along SM1, a metal pipe in the ground created an anomalous spike (Figure 35). In addition, measurements along SM1 taken in the vicinity of train tracks were removed due to possible disturbance from the tracks. All the corrected magnetic total field measurements from lines MAG1a, MAG1b, MAG2 and MAG3 are presented in Figure 35. The magnetic total field values vary between 52500–55000 nT.

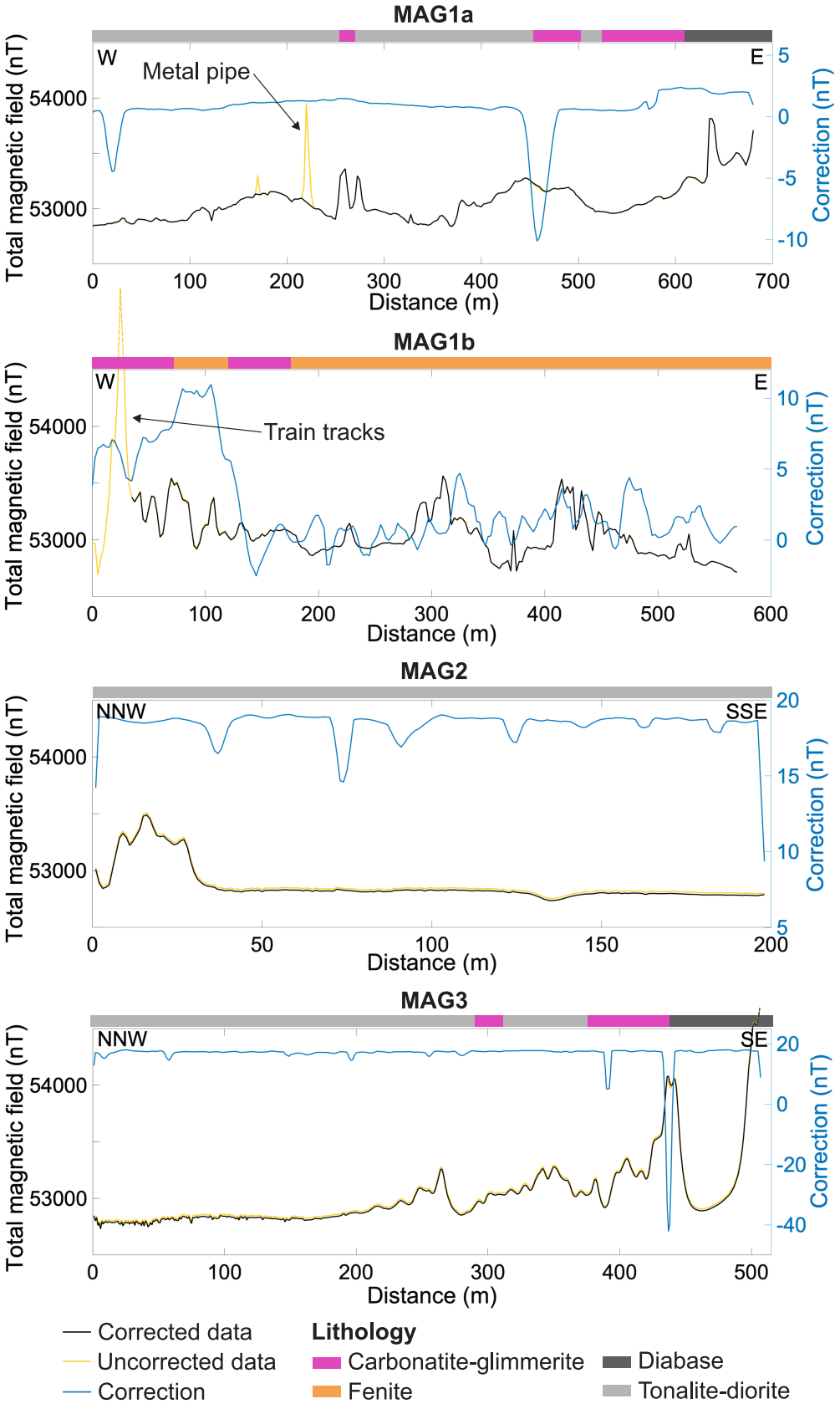

Figure 35. The corrected and uncorrected magnetic total field values and the correction applied for the magnetic lines MAG1a, MAG1b, MAG2 and MAG3 (Figure 14). The correction corrects for the effect of the daily variation. Anomalous spikes due to artefacts have been manually removed from the data. The geology bars have been extracted from the known surface geology (Figure 14).

5. RESULTS AND INTERPRETATION

5.1. Reflection seismic data

5.1.1. Physical properties essential for interpretation of reflection seismic data

Seismic reflections may arise from geological features like lithological contacts or shear zones where there is a contrast in the physical properties, specifically in the acoustic impedances. With the available density and seismic velocity information (Table 5, see section 1.3.1), the reflection coefficients between different contacts related to the Siilinjärvi deposits can be calculated (Equation 2.6, see section 2.1.2). With the reflection coefficient information, the reflectivity of different contacts can be estimated. Based on the calculated reflection coefficients, the carbonatite-glimmerite ore and diabase against other rock types produce distinct reflections (Table 6), for which the approximate minimum value is 0.06 (Salisbury et al. 1996) (see 2.1.2). However, given the right circumstances, the densities and seismic velocities might be equal or so close to each other that the lithological contact will not create a distinct reflection. Fracture and shear zones should reduce seismic velocities and densities and produce reflections if they are large enough. A connection between the reduced seismic P-wave velocities and lower rock quality was seen in the physical property measurements made in the Siilinjärvi mine site (Figure 5). In addition, the tomography results of the earlier seismic measurements by Malehmir et al. (2017b) indicate that the weakness zones are associated with reduced seismic velocities (see section 1.3.2).

Table 5. Estimated P-wave velocities and densities for different rock types in the Siilinjärvi deposit mainly from Malehmir et al. (2017b). Values for gneiss and granite from Schön (2011b and 2011c).

Rock type	P-wave velocity ms-1	Density kgm-3
Carbonatite-glimmerite ore	5000–6500	2800–2950
Diabase	4600–6500	2750–3050
Fenite	5200–6100	2575–2675
Diorite	5400–6300	2650–2900
Gneiss	3000–4900	2500–2800
Granite	4200–5800	2500–2600

Table 6. Seismic reflection coefficients for different rock contacts. The reflection coefficients are calculated with Equation 2.6 using density and P-wave velocity information presented in Table 5.

Interface	Reflection coefficient R (+1 to -1)	Average R
Ore & diabase	0 to ± 0.2	0.1
Ore & diorite	0 to ± 0.14	0.07
Ore & fenite	±0.02 to ± 0.17	0.1
Ore & gneiss	±0.01 to ±0.43	0.22
Ore & granite	±0.03 to ± 0.29	0.16
Diabase & diorite	0 to ± 0.18	0.09
Diabase & fenite	±0.01 to ± 0.19	0.1
Diabase & gneiss	0 to ± 0.45	0.23
Diabase & granite	±0.03 to ± 0.31	0.17

5.1.2. Results and interpretation of the reflection seismic line

Multiple reflective events can be seen in the final stacked reflection seismic profile SM1 (Figure 28). The depth extent of the data is much better than required considering the main goals of this project related to minable depths. With large-scale inspection of the data, the profile could be divided into three parts; the western side controlled by

continuous deeper reflections dipping to the east, the reflectivity-wise quieter area on the eastern side of the profile and the complex reflectivity of the near subsurface (approximately the first 1 km) (Figure 28). The continuous reflection package on the western side of the profile starts approximately at 700 m depth and continues at depth to the end of the herein investigated depth of 4 km. The most intense reflections of the package appear at 2–3 km depth.

Because the mineable depths at the near subsurface are the main interest of this study, the interpretation focused within the first kilometer of the profile. The reflectivity of the near subsurface is characterized by multiple mainly sub-horizontal reflections creating a complicated reflection package. Based on the surface geology, borehole data and the reflective response, the extent of the carbonatite-glimmerite deposit can be outlined (Figure 36). The eastern end of the profile displays a clearly contrasting reflective response, which is interpreted as the sub-vertical contact between the reflectivity-wise quiet fenite and the carbonatite-glimmerite ore characterized by the presence of multiple sub-horizontal reflections. On the western side, the ore is in contact with the tonalite-diorite intrusion. However, the borehole data show that the tonalite-diorite alternates with the carbonatite-glimmerite and seemingly some of the reflections within the carbonatite-glimmerite are likely caused by contact between the two units, which is possible considering the physical properties (Table 6). At depth, the carbonatite-glimmerite ore is interpreted to be constrained by the first of the many continuous east-dipping features, but it should be noted that at this point there is no clear understanding of what the east-dipping events are. The interpreted ore body continues up to ~900 m depth. However, the depth observed depends on the velocity used in the time-to-depth conversion, 5500 ms^{-1} in this case. If the velocity has been evaluated for example 200 ms^{-1} too high or low, the effect would be ±0.0364 m per one meter and for example, the interpreted 900 m depth would have ±33 m difference depending on the velocity. Most of the reflections within the carbonatite-glimmerite were interpreted as diabase dyke contacts, which based on the physical properties is likely (Table 6). The shapes of the reflections imply that some of the contacts may belong to the top and bottom surfaces of a thick diabase dyke (>20 m, see Table 1 for vertical resolution). The area occurring approximately between 200–400 m depth, within the carbonatite-glimmerite, is an area of reduced reflectivity. Whether the area is created by a large diabase dyke or a more homogenous segment of carbonatite-glimmerite ore cannot be confirmed with the borehole data available. The borehole

closest to the area, on the northern side of the profile, has a thick diabase section that could be related to the area but when looking at the situation from the south the area seems to be related to the carbonatite-glimmerite. Possible fault zones were outlined utilizing the borehole rock-quality designation (RQD) data and the large geological contacts.

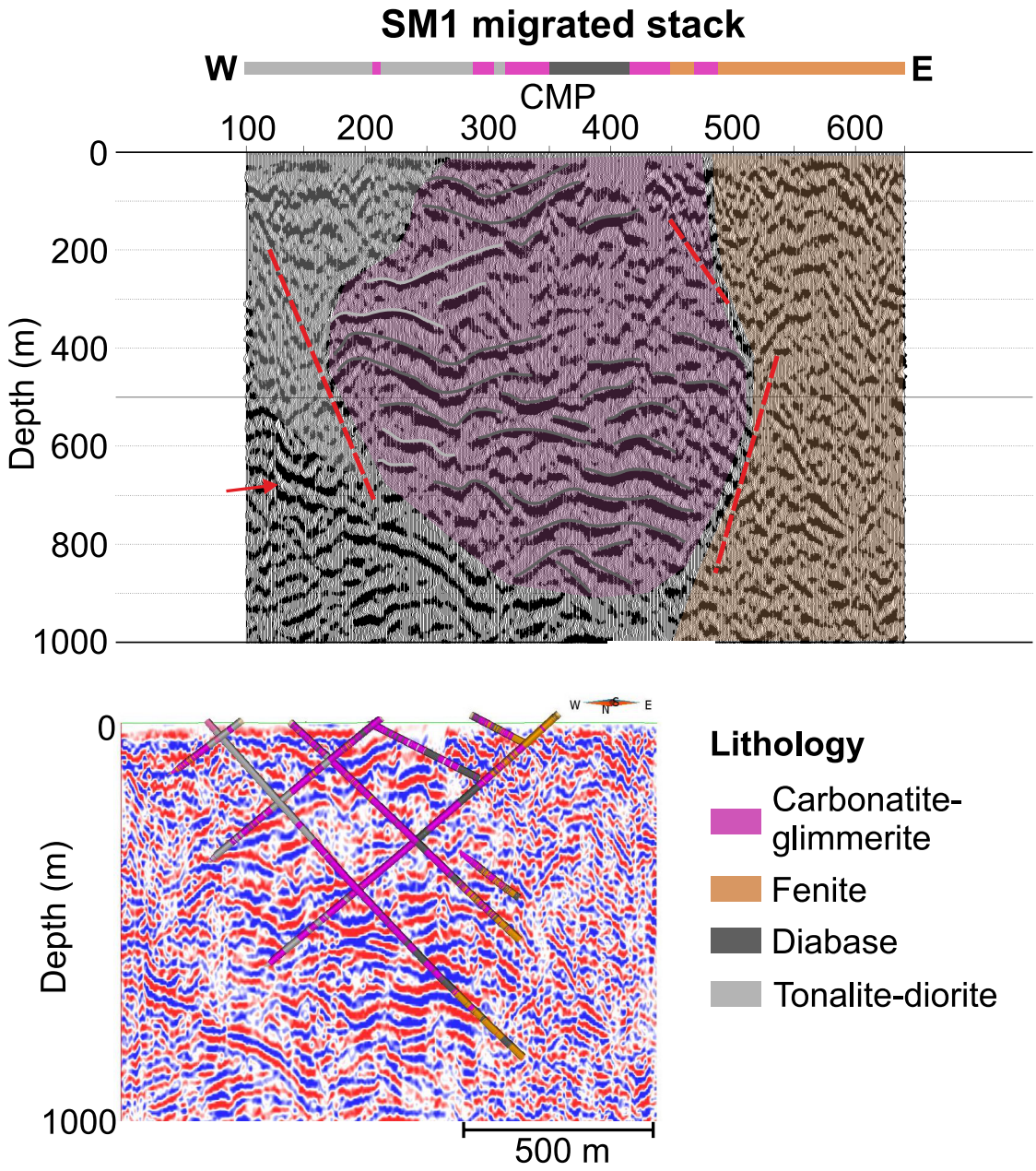

Figure 36. The geological interpretation of the reflection seismic line SM1. Above: the migrated reflection seismic stack with the interpreted features. The interpreted diabase dyke and tonalite-diorite contacts within the carbonatite-glimmerite ore have been outlined with dark (diabase) and light (tonalite-diorite) grey lines. The red dashed lines represent possible fault zones. The location of the first of the many east-dipping reflections is indicated with the red arrow (see the whole section shown in Figure 28). Below: The reflection seismic data with borehole lithology information. Only the boreholes closest to and on the southern side of the seismic line are included (Figure 10). The migrated sections have no vertical or horizontal exaggeration (1:1) and the view is towards the north. See Figure 10 for the CMP locations.

5.2. GPR data

5.2.1. Physical properties essential for interpretation of GPR data

Changes in water content, lithology and density are the main causes to create differences in the dielectric properties causing electrically reflective boundaries (Hänninen 1991). Calculating reflection coefficients for different rock contacts will give an understanding of whether reflections are theoretically possible or not, like in the case of reflection seismic data (see section 5.1.1). With Equation 2.15 (see section 2.2.2) and relative dielectric permittivity information (Table 4), the reflection coefficients for different rock contacts were calculated (Table 7). The calculations show that the carbonatite-glimmerite ore and the diabase dykes in contact with each other, diorite or gneiss should produce detectable reflections to the acquired radar profiles. Considering the protolith rock of fenite, the dielectric properties of fenite likely resemble the dielectric properties of gneiss, and fenite might be reflective when in contact with the carbonatite-glimmerite ore or diabase. Problems for reflectivity can occur if the relative permittivity values are equal or close to each other. For example, gneiss and the carbonatite-glimmerite ore might have equal relative permittivity values leading to a nonreflective interface (Table 4).

Table 7. Estimated reflection coefficients for electromagnetic waves at different rock contacts. The reflection coefficients are calculated with Equation 2.15 using relative dielectric permittivity information presented in Table 4.

Interface	Reflection coefficient R (+1 to -1)
Ore & diabase	±0.03 to ±0.24
Ore & diorite	±0.02 to ±0.11
Ore & gneiss	0 to ±0.16
Ore & granite	0 to ±0.21
Diabase & diorite	±0.14 to ±0.25
Diabase & gneiss	0 to ±0.25
Diabase & granite	0 to ±0.35

5.2.2. Interpretation of GPR results

All the GPR profiles reveal complex reflectivity within the subsurface. We focused the interpretation on lines 196, 197, 204, 205 and 206 along SM1 and on line 203 from the pit (Figure 12). In the pit, the contact to the bedrock is almost immediate and the reflectivity seen on the profiles is from bedrock features. However, it should be noted that the line 203 did run over a built road structure which, based on the GPR data and the GigaPan image, is fairly thick at some places. Along line 203 the overburden layer was interpreted to be ~1–2 m thick (Figure 37). Based on the Quaternary deposit thickness map presented in the study by Luoma et al. 2014 (see section 1.3.3) the overburden thickness along SM1 varies between 0–4.2 m. The boreholes closest to SM1 have overburden thicknesses varying from 0.8 to 8.6 m. The interpreted overburden thickness along SM1 varies between ~1–8 m (Figure 37). Again, like in seismic data, the depth observed depends on the velocity used for the time-depth conversion. For example, if the velocity would differ ±0.02 mns^{-1} from 0.1 mns^{-1}, the change in depth would be 0.2 m per one meter, meaning that a reflection at 10 m depth would be ±2 m from this depth. The overburden is thicker in the middle parts of the line and the areas of thicker overburden seem to be related to those parts of the line where the terrain was very clayey, for example between 450–600 m along line 196 (Figure 37).

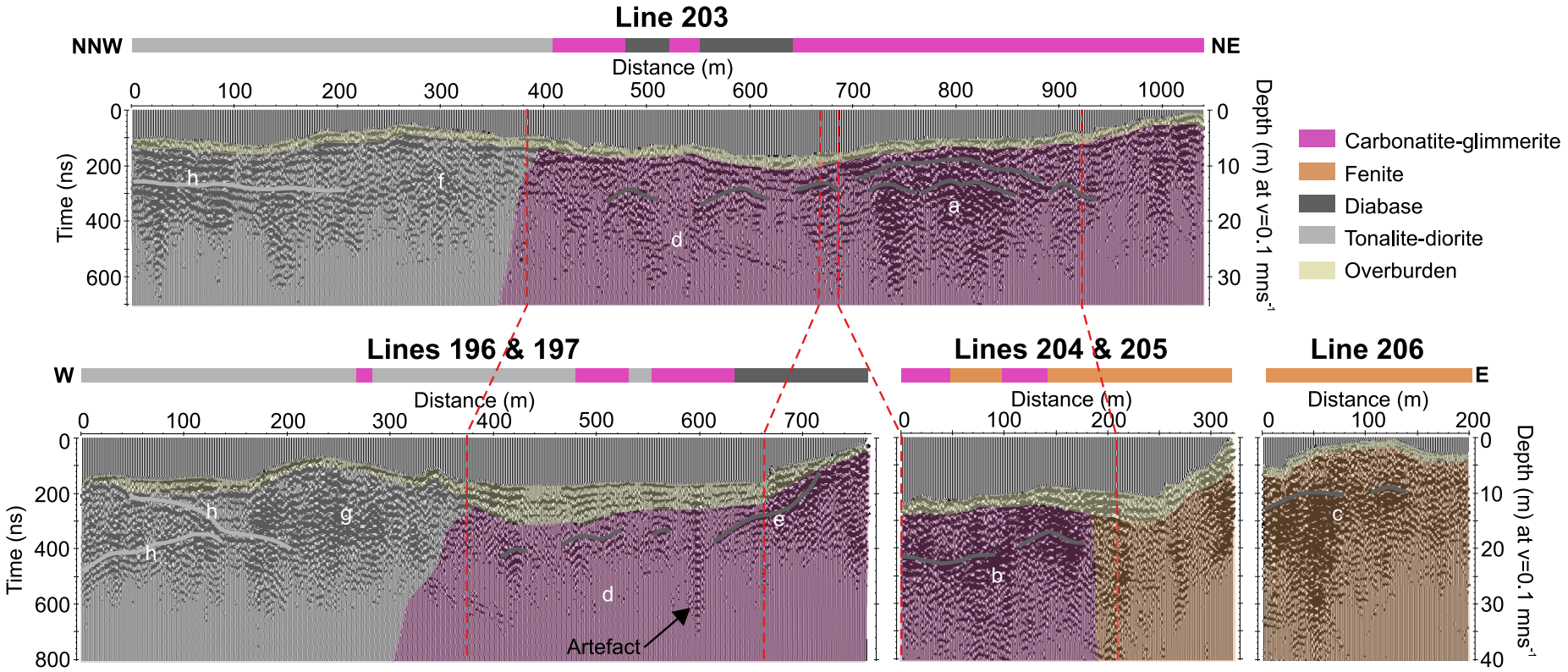

Figure 37. Interpreted GPR lines 196, 197, 204, 205 and 206 measured along SM1 and 203 measured around the southern face of the Särkijärvi pit (Figure 12). Possible diabase dyke contacts are shown with dark grey lines. The red dashed lines connect areas with similar reflectivity from the pit and south of the pit along SM1. Letters a–h show different areas or features discussed.

By correlating the profile 203 with the GigaPan and 3D photogrammetry models (Geotieteiden digiloikka 2019) created form the southern face of the Särkijärvi pit, a relation between the main carbonatite-glimmerite phase and an area of high reflectivity was observed (a, Figure 37). There are several sub-horizontal diabase dykes within the area and the reflectivity was interpreted to be caused by diabase dyke contacts. Similar reflectivity seen along lines 204 and 205, south of the pit along SM1, was also interpreted as sub-horizontal diabase dyke contacts (b, Figure 37). In addition, there is a high reflectivity area within fenite at the end of SM1 on line 206 (c, Figure 37). Based on the earlier observations, the reflectivity within the fenite could be caused by diabase dykes. To distinguish individual dykes, the vertical thickness should be approximately 1 m or more and horizontal separation (and continuation) 5–6.5 m at 5 m depth and up to 8–11 m at 15 m depth (Table 2). Towards west, the reflectivity within the carbonatite-glimmerite is more discontinuous and fragmented (d, Figure 37). This applies in the pit (line 203) and south of the pit (lines 196 and 197). The dipping reflection at the end of lines 196 and 197 (e, Figure 37), interpret as diabase dyke, seems to reach the surface in the same area as a diabase dyke interpreted in the reflection seismic data (Figure 36). The reflection in the GPR data could possibly be from a top contact of a thicker dyke.

Reflections are also seen within the tonalite-diorite (f and g, Figure 37). Based on the surface geology, some of the reflectivity could be related to carbonatite-glimmerites within the tonalite-diorite, which is possible considering the estimated reflection coefficients (Table 7). However, within the area (g, Figure 37), there are two boreholes in the close proximity of SM1 enabling correlation with the GPR data (Figure 12). Despite the boreholes being very close and even cross-cutting each other, the lithologies are different. The other has a granite unit which changes to tonalite-diorite at ~35 m depth and the other has a tonalite-diorite unit until 30 m depth. Based on these, the reflectivity seen within the tonalite-diorite could be caused by granite within the unit. There are also a few long continuous sub-horizontal reflections at the beginning of lines 203 and 196 (h, Figure 37). However, there is no data available to verify what kind of contacts have caused these long sub-horizontal reflections within the tonalite-diorite.

The scale of features seen in the GPR data is significantly finer compared to reflection seismic data. Hence, the approximated contacts between the carbonatite-glimmerite ore,

tonalite-diorite and fenite were estimated utilizing the known surface geology. Details of the interpretation were constrained by the limited number of borehole data available, especially along SM1, and the extent of the GigaPan and 3D photogrammetry models, as they did not cover the first ~300 m of line 203.

5.3. Magnetic data

5.3.1. Physical properties essential for interpretation of magnetic data

Magnetic anomalies are created by changes in the magnetic susceptibility and/or remanent magnetization. As mentioned earlier (see section 1.3.1), the magnetic susceptibility measurements made from three boreholes in the Siilinjärvi mine site imply that the carbonatite-glimmerite ore has slightly elevated values compared to the other rock types, although overall the variation was slight (Figure 5). Table 8 present magnetic susceptibility values for different rock types in the Siilinjärvi mine. Based on the values, the carbonatite-glimmerites are likely to produce magnetic anomalies within the geological setting. Susceptibilities for fenite are also slightly higher (Table 8), however, this observation is based on a very limited number of measurements (Figure 5). Because there is no data available for remanent magnetism, the possible effect of remanent magnetization to the magnetic total field will not be considered in this work.

Table 8. Magnetic susceptibility values for different rock types in the Siilinjärvi deposit. The table combines magnetic susceptibility values from Malehmir et al. (2017b) and Hunt (1995)*. Values from Malehmir et al. (2017b) are based on magnetic susceptibility measurements done in three boreholes from the Siilinjärvi mine site (see section 1.3.1).

Rock type	Magnetic volume susceptibility (SI)
Carbonatite-glimmerite ore	0.13–0.21
Diabase	0.13 (0.01–0.16*)
Fenite	0.13–0.15
Diorite	0.13 (0.0063–0.13*)
Gneiss	0–0.025*
Granite	0–0.05*

5.3.2. Interpretation of the Magnetic results

By comparing the surface geology with the magnetic total field profiles, general observations about the magnetic responses of different rock types can be withdrawn. The total field profiles and the surface geology are presented in Figure 35. Firstly, the tonalite-diorite is magnetically quiet, as the total magnetic field shows very little variation within the tonalite, especially along lines MAG2 and MAG3 (Figure 35). The magnetic susceptibilities measured from the tonalite-diorite show a similar constant pattern with essentially no variation (Figure 5). Secondly, the carbonatite-glimmerite ore seems to be related with elevated magnetic total field values. For example, along MAG3 a clear change in the magnetic response is seen when the carbonatite-glimmerite is reached (~250 m along MAG3, Figure 35) and the total field chances from constant (tonalite-diorite) to elevated, changing anomaly values (Figure 35). The carbonatite-glimmerite should produce a magnetic anomaly, especially when it is in contact with the tonalite-diorite based on the magnetic susceptibilities (Table 8). However, the magnetic total field values do vary also within the carbonatite-glimmerite (Figure 35) which is in line with the magnetic susceptibility measurement made in Siilinjärvi (Figure 5). This could indicate changes in the ore content (carbonatite/glimmerite rich), in particular on the magnetic content of the ore, or be caused for example by diabase dykes. Thirdly, the magnetic response created by fenite seems variable. This observation is based on the profile MAG1b where the surface geology is mostly fenite (Figure 35). The magnetic anomalies could be created by magnetic susceptibility variation within the fenite (Table 8) or by for example carbonatite-glimmerite or diabase cutting the fenite. However, there is no borehole data available from the area or close by the area to confirm the cause of the anomalies. In addition to the different responses, profiles MAG1a (eastern end) and MAG3 (south-eastern end) show an overall increasing trend towards the southern end of the Särkijärvi pit (Figure 14).

The processing of the reflection seismic, GPR and magnetic data were done within limited time spam. Within this time spam, only very basic interpretation was done for the magnetic data. To utilize the data further, forward or inversion modelling could be implemented on the data.

6. DISCUSSION

6.1. Data acquisition and processing considerations

The usability, i.e., the following processing and interpretation results, of geophysical data, depends on the quality of the data acquired. Careful planning of a survey is essential for successful results. The seismic survey carried out by the Smart Exploration project in Siilinjärvi was carefully planned beforehand which ensured that all of the data planned to be acquired were acquired. The GPR and magnetic surveys were not as carefully planned and the time available for these measurements was constrained by the time left from the seismic survey which was carried out throughout the whole field period. The incompleteness in the planning affected especially the magnetic survey. The magnetic measurements took longer than expected as the magnetometer used, unlike anticipated, did not include its own GPS and each measurement had to be taken individually with a discrete station recording. A GPS attached to the magnetometer would have enabled continuous measurements quickening the measurement process. Due to the longer time taken by the magnetic measurements, magnetic data could not be acquired along the southern edge of the Särkijärvi pit within the limited time available for data acquisition.

Processing of reflection seismic data is the most complex and demanding out of the geophysical data processed. The terrain along SM1 was not ideal for data acquisition, effecting the signal-to-noise ratio of the data and by that the processing of the data. In particular, within the soft clayey parts of the line, the coupling of the geophones with the bedrock was most likely defective. In hard-rock environments, good coupling of receivers and sources with the bedrock is pivotal for improving the signal-to-noise ratio of reflection seismic data (Salisbury and Snyder 2007). First-break picking was challenging as the first arrivals near the sources could not be easily identified and essentially no first breaks were visible on the drop hammer shot gathers. These greatly limited the number of the first-break picks on which the near-subsurface velocity model for refraction static corrections is based on. A way to speed up the first-break picking or even skip the process could significantly reduce the time used for processing. One aspect of the Smart Exploration project is to develop alternative methods for estimating static corrections (Malehmir et al. 2019). One approach is to derive the longer-wavelength static corrections from surface-wave analysis (Papadopoulou et al. 2019). Papadopoulou et al. (2019) have

tested the method with reflection seismic data from the Ludvika iron-oxide mining site in Sweden with promising initial results. The surface-wave approach will be tested also with the Siilinjärvi reflection seismic data and the refraction static corrections produced within this work will give a reference for the tested approaches. To test the effect of refraction statics to the final stacked data, refraction statics were calculated from multiple different near-surface velocity models created using the first-break pics. All the 2-layer and 3-layer models suggested a relative thin low-velocity layer with deeper notches in the middle of the line (Figure 20). The shapes of the low-velocity layers presented in the two models are following the same general shape, but because of the different overburden velocities used, the thickness of the layers differs (Figure 20). However, the computational statics corrections are very close to each other in both of the models. The shape of the low-velocity layers modelled resembles the overburden layer interpreted from GPR data along SM1 (Figures 20 and 37), noting that there is no GPR data right from the middle of the line due to a railroad. Considering the resemblance, the GPR data could be utilized as a constrain for the building of the near-surface velocity model for refraction static corrections. The refraction static corrections extracted from the different near-surface velocity models all improved the stacked section, but the difference between the models was slight. During the process, it was noted that residual statics calculated later on in the processing flow had a much greater impact on the final stack compared than the choice of the refraction statics.

Another crucial aspect in the processing of the reflection seismic data was the presence of S-wave arrivals, overpowering the near-subsurface reflectivity (especially the first 400 m), the main interest area of the study. Suppression of the S-wave arrivals was found to be important for revealing the genuine near-subsurface reflectivity. Several different filtering techniques were tested but attenuation of the S-wave arrivals was found to produce the best solution. After the suppression of the S-wave arrivals, reflections could be followed all the way from the surface of the produced stack.

Considering the signal-to-noise ratio of the reflection seismic data, bandpass frequency filtering was also an important step on the processing flow, as it significantly improved the signal-to-noise ratio of the data and primarily removed the surface waves. The importance of bandpass filtering in hard-rock environments has been discussed for example by Eaton et al. (2003) and Buske et al. (2015). Methodological developments to

increase the signal-to-noise ratio are also done within the Smart Exploration project. Balestrini et al. (2019) have developed and tested a new method to increase the signal-to-noise ratio by suppressing surface waves using seismic interferometry, and tested the approach with active-source reflection seismic data from the Ludvika mining area in Sweden. Whether this method or some other will be tested with the Siilinjärvi data, the processing workflow built in this study can be used as a reference.

6.2. Interpretation

6.2.1. Reflection seismic

With reflection seismic data, large-scale geological features could be observed. Based on the reflective response of the subsurface, the carbonatite-glimmerite deposit was outlined (Figure 36). The contact between the carbonatite-glimmerite and fenite was considerably sharper on the eastern edge of the deposit. This implies that the structural setting seen in the Särkijärvi pit (see section 1.2) continues further to the south and the contact between the ore and fenite on the eastern side remains sharp, while on the western side the structural setting is more complicated.

The sub-horizontal reflections seen within the carbonatite-glimmerite ore are most likely caused by diabase dykes or diorite cutting the ore, based on the physical property and borehole information. T. Kauti (Kauti et al. manuscript in preparation) is constructing a detailed waste-rock dyke network 3D model, i.e., diabase dyke model, as a part of the Smart Exploration project. One aspect of the work has been to use production drilling information from the mine to constrain a model of the larger diabase dykes (Figure 38). The diabase dykes have been separated into different populations. As mentioned earlier, the main interest is on the sub-horizontal waste-rock dykes, significant for mine planning and possible to detect with the surface-based reflection seismic measurements. The diabase dyke model is constrained to the Särkijärvi pit but there is no reason to assume that the dyke populations would not continue further south. Figure 38 presents the sub-horizontal dyke population of T. Kauti (Kauti et al. manuscript in preparation) together with the reflection seismic line SM1. By correlating the data, a connection between the sub-horizontal dyke population and a near-surface reflection can be seen. The shape of the reflection resembles a syncline folding structure, which could be related to, or is a

continuation of, an anticline folding shape seen in one of the modelled diabase dykes. Based on the correlation, the reflection is likely caused by a diabase dyke. This interpretation could be expanded to the sub-horizontal reflectivity within the carbonatite-glimmerite ore at ~300–800m depth. As already discussed before (see section 5.1.2), these reflections are possibly also created by sub-horizontal dyke populations.

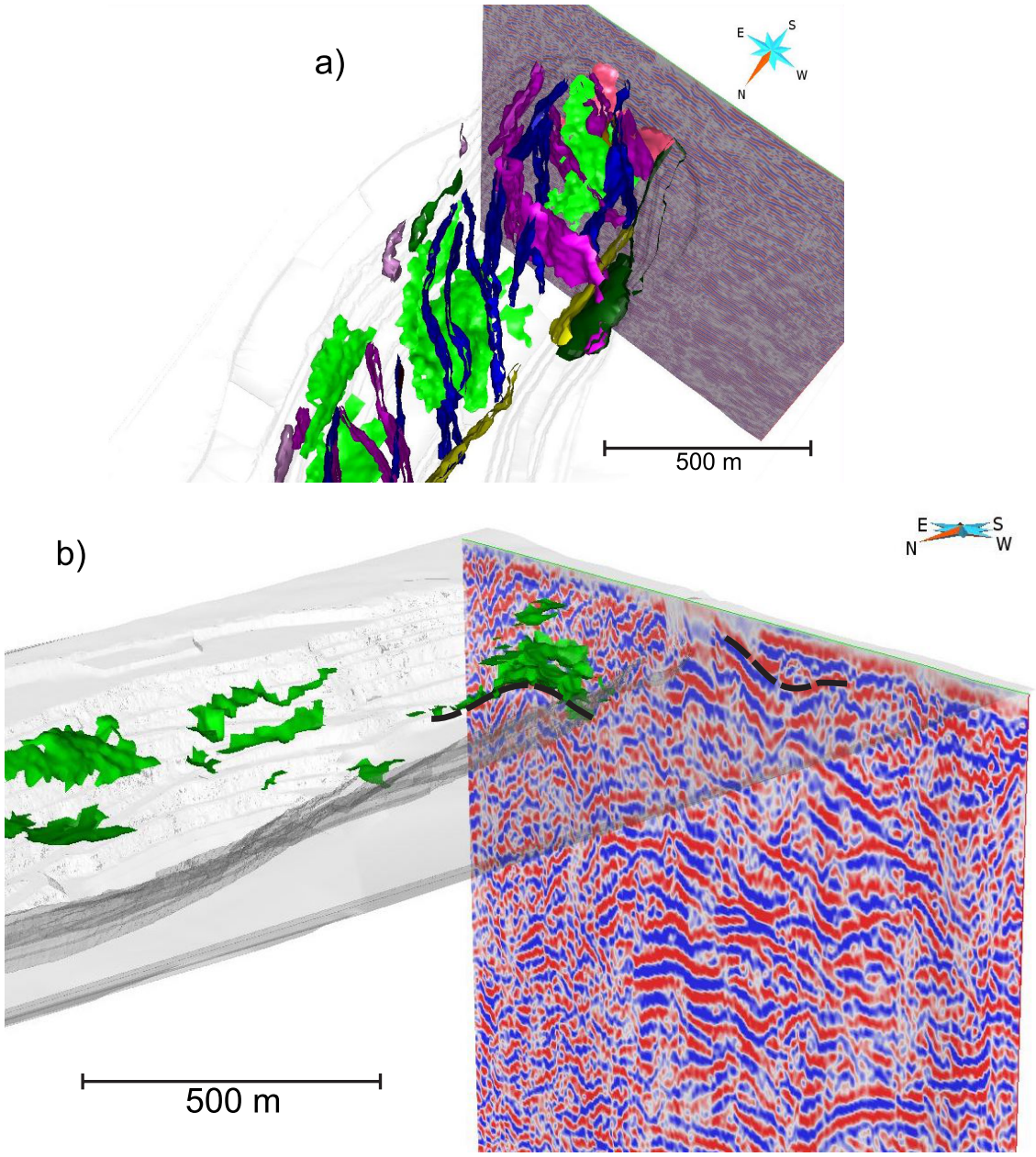

Figure 38. 3D views of the reflection seismic data and the waste-rock dyke, i.e., diabase dyke, network model based on production drilling data (Kauti et al. manuscript in preparation). Figure a) shows all the modelled waste-rock dykes. The different colours present different dyke populations. The sub-horizontal diabase dyke population is presented in green. Figure b) shows the sub-horizontal dyke population with reflection seismic line SM1. The dashed black line outlines the shapes of a modelled diabase dyke, and a diabase dyke interpreted from the reflection seismic data. The shapes resemble an anticline and a syncline of folding structures.

Donczew et al. (2019) were able to locate major shear zones from the eastern edge of the Särkijärvi pit with the in tunnel-seismic data acquired during the Smart Exploration field campaign in Siilinjärvi (see section 1.1). Indications of fault zones on the eastern side of the deposit are also seen on the reflection seismic data from SM1 (Figure 36). To gain a better understanding, a more detailed interpretation should be implemented on the reflection seismic data focusing on the structural setting. The interpretation work will be continued by T. Kauti (Kauti et al. manuscript in preparation). In addition, the tomography models created from the earlier seismic measurements done in the Siilinjärvi deposit (Malehmir et al. 2017b, see section 1.3.2) show areas of reduced seismic velocities, which correlate with areas of know weakness zones in the eastern side of the Särkijärvi pit.

6.2.2. GPR

The resolution and depth extent of GPR data differ significantly compared to the reflection seismic data and should be inspected at a different scale. In GPR data much finer details are seen but the depth extent of the data is only up to 30 m, meaning that the reflections interpreted as diabase dykes would arise from smaller sub-horizontal dykes when compared to the features interpreted as diabase dykes in the seismic data. By interpreting the GPR data with the GigaPan images we could already see that the area of high reflectivity corresponded well with the main carbonatite-glimmerite phase and the sub-horizontal reflections seen within it were interpreted as diabase dykes (Figure 37). Another aspect of T. Kauti's (Kauti et al. manuscript in preparation) work has been to create a detailed waste-rock dyke model from the southern face of the Särkijärvi pit based on field measurements, the GigaPan images and the 3D photogrammetry model (Figure 39). Figure 39 shows a comparison between the high-detail waste-rock dyke model and the GPR line 203 measured in the pit. The comparison shows, that the reflections interpreted as diabase dykes correlate with the modelled dykes and it seems that most of the reflections within the carbonatite-glimmerite ore could be explained by diabase dikes. When comparing the two together it should be noted that the near subsurface depths in the GPR profile are distorted due the antenna separation and the reflections appear to be at deeper depths than in reality (see section 4.2.1). In addition, the velocity used for the time-to-depth conversion affects the depths and the time-to-depth conversion could be recalibrated with the geological constrains (see section 5.2.2).

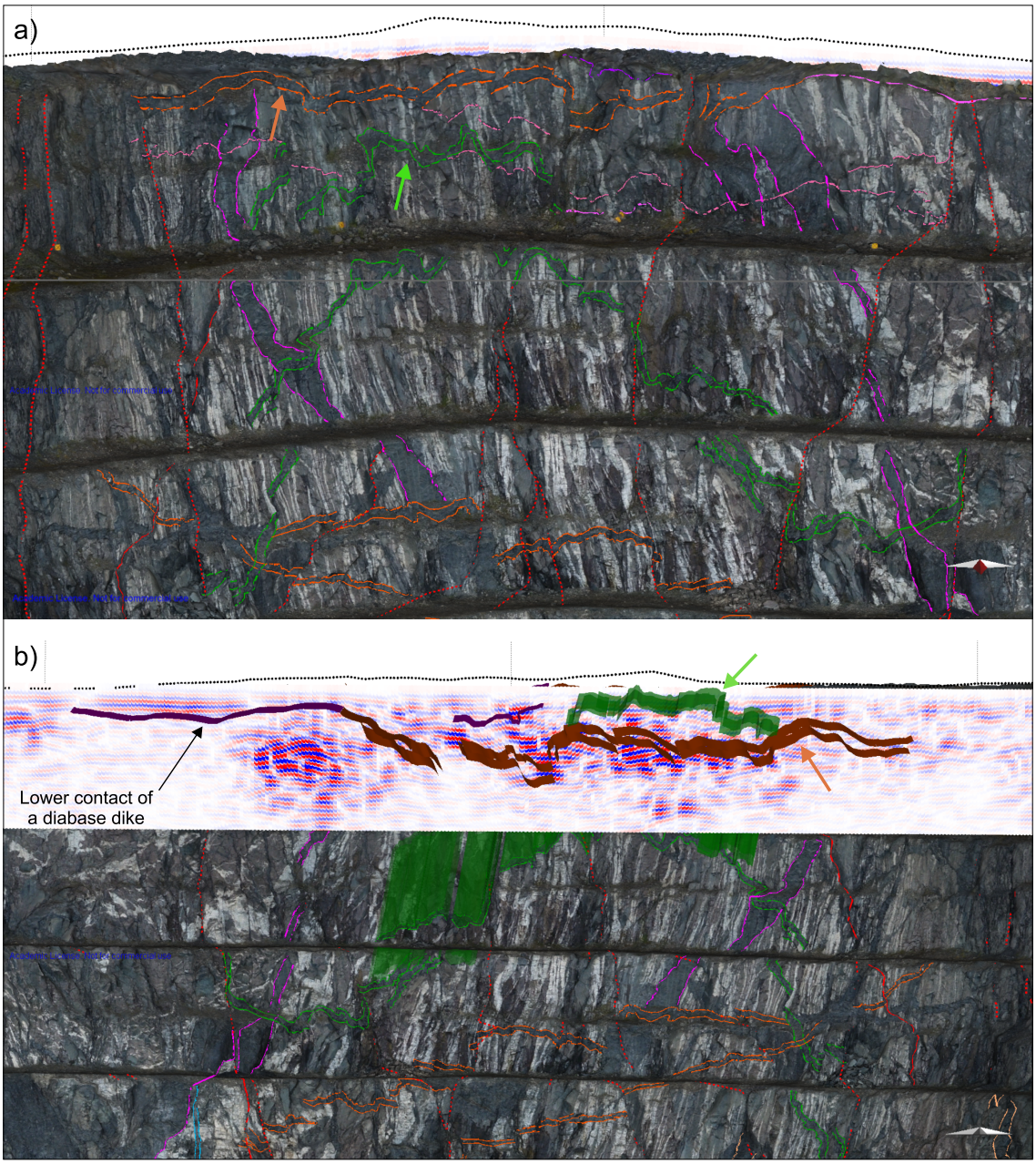

Figure 39. A comparison between the GPR data acquired along the southern edge of the Särkijärvi pit (line 203) and the high-detail waste-rock dyke model created by T. Kauti (Kauti et al. manuscript in preparation). Figure a) shows the 3D photogrammetry model together with the modelled diabase dykes looking towards the south. The pit location corresponds approximately to the distance between 700–900 m in the GPR line 203 (Figure 37). Figure b) shows the 3D photogrammetry model and the diabase dykes together with the GPR data looking towards the north. The different colours of the diabase dykes refer to the positions of the dykes. The orange dyke in the near subsurface, denoted with the orange arrows, is dipping towards the south and the green dyke, denoted with the green arrows, is dipping towards the north. The two dykes are cutting each other somewhere between the pit wall and the GPR line which is why the dykes change order when the viewing angle changes from south to north. In this figure, the GPR data has been plotted to a constant datum, i.e., no elevation variation. The black dashed line shows the true zero position of the GPR line. Figure made by T. Kauti.

The earlier seismic profiles from Malehmir et al. (2017b) (see section 1.3.2.) show also sub-horizontal reflections in the near subsurface of which some might be produced by sub-horizontal dikes (see for example figure 16 (a) in Malehmir et al. 2017b). However,

between the seismic and GPR methods, the GPR method is much easier to implement, and as a routine mine planning method, GPR would be more efficient.

6.2.3. Magnetic

Considering the magnetic susceptibility values and the magnetic total field measurement, a rock mass formed mostly of the tonalite-diorite should appear as a magnetically quiet area. The carbonatite-glimmerite ore seems to be associated with anomalous magnetic values and should be distinguishable, especially from a tonalite-diorite contact. The overall increasing anomaly value trend towards the southern end of the Särkijärvi pit appears to correlate with the area of higher magnetic values seen in the aeromagnetic map (Figures 6, 14 and 35). However, the magnetic lines acquired do not cross the anomaly and the relation cannot be thoroughly inspected.

6.3. General overview of the methods and future recommendations

The reflection seismic, GPR and magnetic data have very different scales, which is why the interpretation and use should be subjected differently for each method. However, despite the different scales, the reflection seismic, GPR and magnetic data do provide a similar overall picture. With high-resolution magnetic 3D measurements, the continuation of the carbonatite-glimmerite deposit at a large scale could possibly be followed. The magnetic 3D measurement could be implemented for example with the high-resolution UAV-based magnetic acquisition system developed within the Smart Exploration project (Malehmir et al. 2019). On a regional scale, airborne magnetic and radiometric surveys have had a significant influence on the discoveries of new alkaline carbonatite deposits and have proven their capability for locating and delignating carbonatites (Simandl and Paradis 2018). There are multiple examples where, with the ground and airborne magnetic surveys, the characteristic circular, ring-shaped and oval structures of carbonatite deposits have been detected. Examples include, the Alnö carbonatite complex in Sweden (Andersson and Malehmir 2018) and multiple carbonatite deposits in Canada presented by Thomas et al. (2016). In Finland, Vartiainen and Paarma (1979) have used magnetic measurements together with other geophysical data, including for example seismic, radiometric and gravity data, to distinguish the Sokli carbonatite complex, northern Finland, from its surroundings and to characterize the complex.

However, it seems that for example in the case of Alnö complex (Andersson and Malehmir 2018) and the Sokli complex (Vartiainen and Paarma 1979) the magnetic susceptibilities are consistently higher than at Siilinjärvi, and the carbonatite complexes have the characteristic circular shapes, unlike the elongated Siilinjärvi complex.

Results of a magnetic 3D survey made in Siilinjärvi could be utilized in the planning of a seismic 3D survey. With a seismic 3D survey, the large-scale structures, like the contact between the fenite and the carbonatite-glimmerite ore and large fault zones could be determined and in particular, the survey could be used to image the large-scale sub-horizontal waste-rock dykes. The information from a seismic 3D survey could be used in the planning of a new open pit. 3D seismic data have been used for mine planning purposes in different geological settings, for example at the Millennium uranium deposit in Canada (Wood et al. 2012) and the Kevitsa Ni-Cu-PGE deposit in Finland (Malehmir et al. 2018). GPR data, having the resolution required to image smaller-scale features and in particular the smaller sub-horizontal waste-rock dykes, could then be utilized in the operating phase of the mine in a more routine manner. The data should be utilized as a part of the detailed geological modeling used for mine planning, improving the reliability of the production predictions.

Considering possible future geophysical measurements and further utilization of the data presented in this study, I would recommend additional petrophysical measurements. With additional measurements, for example, the magnetic susceptibilities related to different rock types could be estimated more reliably, especially for fenite which seemed to create a highly variable magnetic response (Figure 35). I would also recommend including dielectric property measurements, especially as it seems that the GPR measurements could be utilized in a more routine manner in the future.

7. CONCLUSIONS

The lateral and depth continuation of the Siilinjärvi carbonatite-glimmerite deposit and the large-scale sub-horizontal waste-rock dykes were imaged with the active-source reflection seismic data. The sub-horizontal diabase dykes and tonalite-diorite, intruded to

the ore body, create a complex reflectivity pattern distinguishable from the surrounding bedrock. In particular, the contact between the ore and fenite is sharp. In addition, the large weakness zones were outlined based on the reflection seismic data. The GPR data revealed smaller-scale sub-horizontal waste-rock dykes within the shallow subsurface (<30 m depth). Elevated magnetic total field values are related to the carbonatite-glimmerite ore which should appear anomalous especially when in contact with the tonalite-diorite.

The reflection seismic, GPR and magnetic data all showed a similar overall pattern. However, the scales of the three methods are very different and they should all be applied for different purposes within the mineral exploration and mine planning setting at Siilinjärvi. Magnetic measurements could provide information on the larger-scale continuation of the ore deposit, and the results could be utilized in the planning of a focused 3D seismic survey. Reflection seismic data is applicable for imaging the large-scale structures, and this type of data, i.e., seismic 3D data, should be acquired prior to a new open pit, and be used for the planning of the pit. The GPR data, having the best resolution but a low depth penetration, should be used in a more routine manner for detailed mine planning during the operating phase of the mine.

The processing workflow applied to the reflection seismic data can work as a reference flow for testing new methods developed for reflection seismic processing within the Smart Exploration project, concerning in particular static corrections and methods for enhancing the signal-to-noise ratio.

ACKNOWLEDGMENTS

I would like to thank the Smart Exploration project for the possibility to take part in the project and for the funding of this thesis. I am grateful for all the old and new acquaintances I met during the field period in Siilinjärvi, who all gave their best contribution to the survey in Siilinjärvi despite the cold and rainy conditions of the Finnish fall. I would like to thank the people from Yara, especially Aleksi Salo, for making the survey possible. I would like to thank my supervisors Emilia Koivisto and

Pietari Skyttä for their guidance. Thank you, Emilia Koivisto, for all your comments and input given in the field while processing and while writing this thesis. I deeply thank Tuomas Kauti for providing material from his work on the waste-rock dyke network 3D model, making it possible to deepen the inspection of the reflection seismic and GPR data.

I thank my family and friends who have supported me through my years at the University. And last but not least, I would like to thank all my student associates who have made these years memorable.

Smart Exploration has received funding from the European Union's Horizon 2020 research and innovation programme under grant agreement No. 775971.

REFERENCES

Airo, M-L. 2005. Aerogeophysics in Finland 1972–2004: Methods, System Characteristics and Applications. Geological survey of Finland, Special Paper 39. 197 pp.

Al Ani, T. 2013. Mineralogy and petrography of Siilinjärvi carbonatite and glimmerite rocks, eastern Finland. Geological survey of Finland, Archive report. 15 pp.

Andersson, M. and Malehmir, A. (2018). Internal architecture of the Alnö alkaline and carbonatite complex (central Sweden) revealed using 3D models of gravity and magnetic data. Tectonophysics. 740–741, 53–71.

Balestrini, F., Draganoy, D., Malehmir, A., Marsden, P. and Ghose, R. 2019. Improved target illumination at Ludvika mines of Sweden through seismic-interferometric surface-wave suppression. Geophysical prospecting.

Bayanova, T. 2006. Baddeleyite: A promising geochronometer for alkaline and basic magmatism. Petrology. 14, 187–200.

Brodic, B., Malehmir, A., Juhlin, C., Dynesius, L., Bastani, M., & Palm, H. 2015. Multicomponent broadband digital-based seismic landstreamer for near-surface applications. Journal of Applied Geophysics. 123, 227–241.

Bloom, A. L. 1962. Principles of Operation of the Rubidium Vapor Magnetometer. Applied Optics. 1, 61–68.

Buske, S., Bellefleur, G. & Malehmir, A. 2015. Introduction to special issue on "hard rock seismic imaging". Geophysical Prospecting. 63, 751–753.

Davis, J.L. & Annan, A.P. 1989. Ground-penetrating radar for high-resolution mapping of soil and rock stratigraphy. Geophysical Prospecting. 37, 531–551.

Da Col, F., Karimpour, M., Papadopoulou, M., Socco, LV., Koivisto, E., Salo, A., Sito, L., Malehmir, A. & Savolainen, M. 2019. Surface Wave Analysis from Mineral Exploration: a 3D Example from Eastern Finland. Poster: Near Surface - Mining A. in 81st EAGE Conference and Exhibition 2019. European association of geoscientists and engineers, EarthDoc.

Donczew, A., Malehmir, A., Koivisto, E., Savolainen, M. and Brodic, B. 2019. Mine Bench-Tunnel Seismic Data Acquisition for Characterizing Shear Zones in the Siilinjärvi Phosphate Mine, Finland. Conference paper: Near Surface Geoscience Conference & Exhibition 2019 8–12 September 2019, The Hague, Netherlands.

Eaton, D., B. Milkereit, and M. Salisbury, 2003, Hardrock seismic exploration: SEG. 277 pp.

European Commission. 2017a. Communication from the commission to the European parliament, the council, the European economic and social committee and the committee of the regions on the 2017 list of Critical Raw materials for the EU. COM/2017/0490 final. 8 pp.

European Commission. 2017b. Study on the review of the list of Critical Raw Materials. Critical Raw Materials Factsheets. Written by Deloitte Sustainability, British Geological Survey, Bureau de Recherches Géologigues et Minières, Netherlands Organisation for Applied Scientific Research. EU publication. 517 pp.

Fisher, S.C., Stewart, R.R. and Jol, H.M., 1992. Processing ground penetrating radar (GPR) data. CREWES Research Report Volume 4. 11, 1–22.

Francke, J. 2012. A review of selected ground penetrating radar applications to mineral resource evaluations. Journal of Applied Geophysics. 81, 29–37.

Geometrics, inc. 2001. G-858 Magmapper 25309-OM REV. D2, Operation Manual. San Jose, California, USA. 106 pp.

Geometrics, inc. 2015. G-857 Memory-Mag Proton Precession Magnetometer, Operation Manual, San Jose, California, USA. 72 pp.

Geometrics inc., 2018a. G-858 MagMapper Magnetometer. Webpages visited 17.10.2019. https://www.geometrics.com/product/g-858/.

Geometrics inc., 2018b. G-857 Magnetometer. Webpages visited 17.10.2019. https://www.geometrics.com/product/g-857/.

Geotieteiden digiloikka. 2019. Webpages visited 21.10.2019. https://blogs.helsinki.fi/geotieteidendigiloikka/.

GLOBE Claritas. 2019. Seismic Processing Software. Webpages visited 17.10.2019. http://www.globeclaritas.com.

Heinonen, S., Imaña, M., Synder, D., Kukkonen, I. ja Heikkinen, P. 2012. Seismic reflection profiling of the Pyhäsalmi VHMS-deposit: A complementary approach to the deep base metal exploration in Finland. Geophysics 77, WC15–WC23.

Heinonen, S., Malinowski, M., Hlousek, F., Gislason, G., Buske, S., Koivisto, E. and Wojdyla, M. 2019. Cost-effective seismic exploration: 2D reflection imaging at the Kylylahti massive sulfide deposit, Finland. Minerals. 9, 263–278.

Hinze, W. J., Saad, A. H. & Von Frese, R. R. B. 2013. Gravity and Magnetic Exploration: Principles, Practices, and Applications. Cambridge University Press, Cambridge, 512 pp.

Hunt, C.P., Moskowitz, B.M., Banerjee, S.K., 1995. Magnetic properties of rocks and minerals, rock physics and phase relations—a handbook of physical constants, 1995 American Geophysical Union. 189–204.

Hänninen, P. 1991. Maatutkaluotaus maaperägeologisissa tutkimuksissa. Summary: Ground Penetrating radar in Quaternary geological studies. Geological survey of Finland, report of investigation. 33 pp.

Jackisch, R., Madriz, Y., Zimmermann, R., Pirttijärvi, M., Saartenoja, A., Heincke, B., Salmirinne, H., Kujasalo, J-P., Andreani, L. and Gloaguen, R. 2019. Drone-Borne Hyperspectral and Magnetic Data Integration: Otanmäki Fe-Ti-V Deposit in Finland. Remote sensing. 11, 2084.

Keller, G.V. 1989. Electrical properties. Carmichael, R.S. (Ed.) Practical Handbook of Physical Properties of Rocks and Minerals. CRC Press, Boca Raton, FL. In Schön, J. 2011a. Chapter 8 - Electrical properties. Physical properties of rocks: A workbook. Elsevier, Oxford, 273–336.

Kauti, T., Skyttä, P. and Savolainen, M. Manuscript in preparation. Assessment of the structural geometry of the complex dyke network (Siilinjärvi, Finland) utilizing data integration and scalability. Implications for the spatial distribution of the dykes within the subsurface. (Working title).

Koivisto, E., Malehmir, A., Hellqvist, N., Voipio, T. ja Wijns, C. 2015. Building a 3D model of lithological contacts and near-mine structures in the Kevitsa mining and exploration site, Northern Finland: constraints from 2D and 3D reflection seismic data. Geophysical Prospecting. 63, 754–773.

Kukkonen, I., Heikkinen, P., Heinonen, S., Laitinen, J. ja HIRE työryhmä. 2011. Reflection seismics in exploration for mineral deposits: initial results from the HIRE project. Geological Survey of Finland, Special Paper 49, 49–58.

Kukkonen, I., Heinonen, S., Heikkinen, P. ja Sorjonen-Ward, P. 2012. Delineating ophiolite-derived host rocks of massive sulphide Cu-Co-Zn deposits with 2D high-resolution seismic reflection data in Outokumpu, Finland. Geophysics 77, WC213–WC222.

Lindqvist, T., Skyttä, P., Koivisto, E., Häkkinen, T. and Somervuori, P. 2017. Delineating the network of brittle structures with geotechnical, structural and reflection seismic data, Kevitsa open pit, northern Finland. GeoResJ. 13, 159–174.

Luoma, S., Majaniemi, J., Nurminen, T., & Pasanen, A. 2014. GPR survey and field work summary in siilinjärvi mine during July 2014. Geological survey of Finland, Archived report. 36 pp.

MALA GPR Australia. 2009-2017. MALÅ ProEx system – Modular full-range Ground Penetrating Radar (GPR) system for the advanced professional user. Webpages visited 17.10.2019. https://www.malagpr.com.au/mala-professional-explorer.html.

Malehmir, A., Durrheim, R., Bellefleur, G., Urosevic, M., Juhlin, C., John White, D., Milkereit, B. & Campbell, G. 2012. Seismic methods in mineral exploration and mine planning: A general overview of past and present case histories and a look into the future. Geophysics. 77, WC173–WC190.

Malehmir, A., Dynesius, L., Paulusson, A., Johansson, H., Bastani, M., Wedmark, M., and Marsden, P. 2017a. The potential of rotary-wing UAV-based magnetic surveys for mineral exploration: A case study from central Sweden. The Leading Edge. 36, 552–557.

Malehmir, A., Heinonen, S., Dehghannejad, M., Heino, P., Maries, G., Karell, F., Suikkanen, M. & Salo, A. 2017b. Landstreamer seismics and physical property measurements in the Siilinjärvi open-pit apatite (phosphate) mine, central Finland. Geophysics. 82, B29–B48.

Malehmir, A., Maries, G., Bäckström, E., Schön, M., & Marsden, P. 2017c. Developing cost-effective seismic mineral exploration methods using a landstreamer and a drophammer. Scientific reports. 7, 1–7.

Malehmir, A., Tryggvason, A., Wijns, C., Koivisto, E., Lindqvist, T., Skyttä, P. and Montonen, M. 2018. Why 3D seismic data are an asset for exploration and mine planning: Velocity topography of wakness zones in the Kevitsa Ni-Cu-PGE Deposit, Northern Finland. Geophysics. 83, B33–B46.

Malehmir, A., Holmes, P., Gisselø, P., Socco, L.V., Carvalho, J., Marsden, P., Verboon, A.O. and Loska, M. 2019. Smart Exploration: Innovative ways of exploring for the raw material in the EU. 81st EAGE Conference & Exhibition 2019. 3–6 June 2019, London, UK.

Mattsson, H. B., Högdahl, K., Carlsson, M. and Malehmir, A. 2019. The role of mafic dykes in the petrogenesis of the Archean Siilinjärvi carbonatite complex, east-central Finland. LITHOS. 342–343, 468–479.

McKevitt Blathnaid, in preparation. Depth and Lateral Extent of the Southern Continuation of the Siilinjärvi Apatite Ore, Finland, Based on Active Seismic 2D data. (Working title). MSc thesis, University of Helsinki.

Milkereit, B. and Spencer, C. 1989. Noise suppression and coherency enhancement of seismic data; in Statistical application in the Earth Sciences. Edited by Agterberg, F.P. and Bonham-Carter, G.F. Geological survey of Canada. 89–9, 243–248.

Neal, A. 2004. Ground-penetrating radar and its use in sedimentology: principles, problems, and progress. Earth-Science Reviews. 66, 261–330.

O'Brien, H., Heilimo, E., & Heino, P. 2015. The Archean Siilinjärvi carbonatite complex. In: Wolfgang, D. M., Lahtinen, R. and O'Brien, H. (Eds.) Mineral deposits of Finland. Elsevier, 327–343.

Olhoeft, G.R. 1981. Electrical properties of rocks. In: Touloukain, Y.S., Judd, W.R., Roy, R.F (Eds.) Physical Properties of Rocks and Minerals. McGraw-Hill, New York. In Schön, J. 2011a. Chapter 8 - Electrical properties. Physical properties of rocks: A workbook. Elsevier, Oxford, 273–336.

Orica Limited. 2019. Uni tronic™ 600 Detonator. Webpages visited 17.10.2019. http://www.oricaminingservices.com/fi/fi/product/products_and_services/electronic_blasting_systems/uni_tronic_600/uni_tronic_600_detonator/1365.

Papadopoulou, M., Da Col, F., Mi, B., Bäckström, E., Marsden, P., Brodic, B., Malehmir, A. and Socco, V. 2019. Surface-wave analysis for static corrections in mineral exploration: a case study from central Sweden. Geophysical prospecting.

Parshin, A., Morozov, V., Blinov, A., Kosterev, A., & Budyak, A. 2018. Low-altitude geophysical magnetic prospecting based on multirotor UAV as a promising replacement for traditional ground survey. Geo-spatial Information Science. 21, 67–74.

Peltoniemi, M. 1988. Maa- ja Kallioperän geofysikaaliset tutkimusmenetelmät. Otaniemi, pp. 412.

Puustinen, K. 1971, Geology of the Siilinjärvi carbonatite complex, Eastern Finland. Bulletin de la Commission Geológique de Finlande. 294, 43 pp.

Reynolds, J. M. 2011. An introduction to applied and environmental geophysics. 2. edition. Wiley-Blackwell, John Wiley & Sons, Chichester, UK, 696 pp.

Ronen, J. and Claerbout, J. 1985. Surface-consistent residual static estimation by stack-power maximization. Geophysics. 50, 2759–2767.

Rukhlov, A. and Bell, K. 2010. Geochronology of carbonatites from the Canadian and Baltic Shields, and the Canadian Cordillera: Clues to mantle evolution. Mineralogy and Petrology. 98, 11–54.

Salisbury, M., Milkereit, B. and Bleeker, W. 1996. Seismic imaging of sulfide deposits: Part I. Rock properties. Economic Geology. 91, 821–828.

Salisbury, M. ja Snyder, D. 2007. Application of seismic methods to mineral exploration, in Goodfellow, W.D., ed., Mineral Deposits of Canada: A Synthesis of Major Deposit-Types, District Metallogeny, the Evolution of Geological Provinces, and Exploration Methods. Geological Association of Canada, Mineral Deposits Division, Special Publication 5, 971–982.

Sandmeier geophysical research. 2018. Reflexw – GPR and seismic processing software. Webpages visited 17.10.2019. https://www.sandmeier-geo.de/reflexw.html.

Schneider, W. A. 1978. Integral formulation for migration in two dimensions and three dimensions. Geophysics. 43, 49–76.

Schön, J. 2011a. Chapter 8 - Electrical properties. Physical properties of rocks: A workbook. Elsevier, Oxford, 273–336.

Schön, J. 2011b. Chapter 4 - Density. Physical properties of rocks: A workbook. Elsevier, Oxford, 97–105.

Schön, J. 2011c. Chapter 6 - Elastic properties. Physical properties of rocks: A workbook. Elsevier, Oxford, 149–243.

Sercel. 2019. UNITE cable-free seismic aquisition. Webpages visited 17.10.2019. https://www.sercel.com/products/Pages/unite.aspx.

Sheriff, R.E. 1975. Factors affecting Seismic Amplitudes. Geophysical prospecting. 23, 125–138.

Sheriff, R. E. 1995. Exploration seismology. 2. Edition. Cambridge University Press, Cambridge, 628 pp.

Simandl, G. and Paradis, S. 2018. Carbonatites: related ore deposits, resources, footprint, and exploration methods. Applied Earth Science. 127, 123–152.

Smart Exploration. 2019. Webpages visited 25.11.2019. https://smartexploration.eu.

Telford, W. M., Geldart, L. P. and Sheriff, R. E. 1990. Applied geophysics. 2. edition. Cambridge University Press, Cambridge, 770 pp.

Thomas, M.D., Ford, K.L. and Keating, P. 2016. Review paper: Exploration geophysics for intrusion-hosted rare metals. Geophysical prospecting. 64, 1275–1304.

Tichomirowa, M., Whitehouse, M.J., Gerde, A., Götze, J., Schulz, B. and Belyatsky, B.V. 2013. Different zircon recrystallization types in carbonatites caused by magma mixing: Evidence from U–Pb dating, trace element and isotope composition (Hf and O) of zircons from two Precambrian carbonatites from Fennoscandia. Chemical Geology. 353, 173–198.

Vartiainen, H. and Paarma, H. 1979. Geological Characteristics of the Sokli Carbonatite Complex, Finland. Economic Geology. 74, 1296–1306.

Wood, G., O'Dowd, C., Cosma, C. and Enescu, N. 2012. An interpretation of surface and borehole seismic survey for mine planning at the Millennium uranium deposit, northern Saskatchewan, Canada. Geophysics. 77, WC203–WC2012.

Woodward, D.J. 1991. Inversion of seismic refraction data. Geophysics Division, DSIR, Wellington, Eastern Bay of Plenty.

Yilmaz, Ö. 2001. Seismic data analysis: Processing, inversion, and interpretation of seismic data. Volume 1–2. 2. Edition. Society of Exploration Geophysicists, Tulsa, 2065 pp.

Zozulya, D. R., Bayanova, T.B. and Serov,P.N. 2007. Age and isotopic geochemical characteristics of Archean carbonatites and alkaline rocks of the Baltic shield. (Author abstract). Doklady Earth Sciences. 415, 874–879.